UNIVERSITY OF OKLAHOMA

GRADUATE COLLEGE

THEORY AND DESIGN OF PARAMETRICALLY TUNED ELECTRICALLY SMALL RECEIVING ANTENNAS

A DISSERTATION

SUBMITTED TO THE GRADUATE FACULTY

in partial fulfillment of the requirements for the

Degree of

DOCTOR OF PHILOSOPHY

By CLAYTON BLOSSER

Norman, Oklahoma

2025

Downloaded from SHAREOK. Persistent Handle URL: https://hdl.handle.net/11244/341656

THEORY AND DESIGN OF PARAMETRICALLY TUNED ELECTRICALLY SMALL RECEIVING ANTENNAS

A DISSERTATION APPROVED FOR THE
SCHOOL OF ELECTRICAL AND COMPUTER ENGINEERING

BY THE COMMITTEE CONSISTING OF

Dr. Jessica Ruyle, Chair

Dr. K.C. Kerby-Patel

Dr. Kurt Schab

Dr. Hjalti Sigmarsson

Dr. Justin Metcalf

Dr. Caleb Fulton

Dr. Sepideh Stewart

© Copyright by CLAYTON BLOSSER 2025
All Rights Reserved.

Acknowledgments

To my son, who was with me through my doctoral work and all he got was this lousy acknowledgment. Your laugh made every hard day better.

Contents

Acknowledgments **iv**

List of Tables **ix**

List of Figures **x**

1 Introduction **1**

1.1 Backgound 1

1.2 Parametrically Tuned, Electrically Small Receiving Antennas 3

2 Analysis tools **6**

2.1 Full-wave simulation methods 6

2.1.1 Method of moments using antenna toolbox for MATLAB . . 7

2.1.2 Finite element method using High Frequency Structure Simulation 8

2.2 Conversion matrices 9

2.3 SPICE 9

2.3.1 Harmonic Balance 9

2.3.2 Transient 10

2.4 Receiver and Equalizer 10

2.5 Conclusion 12

3 Classic parametric amplifier theory **13**

3.1 Manley-Rowe Relations 14

3.2 Parametric amplification 15

3.2.1 Non-degenerate parametric amplification 16

3.2.2 Non-degenerate parametric amplification circuit analaysis . 17

3.2.3 Amplifier bandwidth 20

3.3 Degenerate mode parametric amplification 22

3.4 Non-Degenerate Parametric Amplifier Examples 24

3.4.1 Design 24

3.4.2 Discussion 27

3.5 Conclusion 29

4 Classic parametrically tuned electrically small receiving antennas **31**

4.1 Modeling and analysis of parametrically tuned receiving antennas . 32

4.1.1 Circuit model 32

4.1.2 Analysis 34

4.2 Antenna design 38

4.3 Non-degenerate parametric amplification design 41

4.3.1 Overview of the design process 41

4.3.2 Non-degenerate design 44

4.4 Degenerate parametric amplification 45

4.4.1 Phase coherent 45

4.4.2 Phase incoherent 46

4.5 Performance comparison 46

4.5.1 Maximizing gain and bandwidth 49

4.5.2 Relation of bandwidth to peak gain 53

4.6 Conclusion 55

5 Single balanced parametrically amplified receivers 57

5.1 Single Balanced Parametric Amplifier Theory 58

5.2 Designing a Single-Balanced, Parametrically Tuned Receiver 61

5.3 Results of the Single-Balanced Receiver 63

5.4 Conclusion 64

6 Parametrically amplified electrically small receive filtenna 65

6.1 Introduction 65

6.2 Parametric Amplifiers Using Broadband Couplers 66

6.2.1 Two band couplers using filter theory 67

6.2.2 Circuit Example 69

6.3 Filtenna Design and Analysis 71

6.3.1 Overview of Symmetric Synthesis Method 72

6.3.2 Calculating design targets 74

6.3.3 Radiator design and tuning 75

6.3.4 Non-radiating resonator design and tuning 75

6.3.5 Inter-resonator tuning 76

6.4 Experimental validation and results 77

6.4.1 Asymmetric Variation 80

6.5 Parametrically Tuned Electrically Small Filtenna 81

6.6 Conclusion 83

7 Stability Analysis 85

7.1 Introduction 85

7.2 Review of Stability Analysis 87

7.3 Complex Frequency Method of Moments 90
7.4 Complex Frequency Representation of the Nonlinear Capacitor . . . 93
7.5 Complex Frequency Conversion Matrix-Method of Moments Stability Analysis 95
7.6 Conclusion 98

8 Conclusion **99**

References **102**

List of Tables

3.1 Component values for classic, singly resonant parametric amplifiers 24

3.2 Performance of singly resonant parametric amplifiers. 26

4.1 This table lists the parameter values for the TVC and load resistance of each case. The phase difference between the TVC and incoming signal ϕ_Δ needed to maximize the power received of the degenerate points of the phase incoherent and phase coherent cases is also listed. 46

5.1 Component values for the actively broadbanded and single-balanced parametric amplifiers. 60

5.2 Performance of the single balanced parametric amplifier against design #1. 61

6.1 Component values of the Butterworth coupling network-based parametric amplifier. 69

6.2 Bandwidth and gain of Kuh's Butterworth coupling network-based parametric amplifier. 71

6.3 The g-coefficients and filtenna design targets for a second-order, equal ripple response with 3 MHz of -10 dB equal-ripple 74

List of Figures

1.1 The radiation efficiency-bandwidth product of several passive, LTI ESAs from literature plotted as a function of the electrical size (x-axis) of the circumscribing sphere around them ka [6]. Some of the designs that came the closest to the bound are marked with the author and a citation number, and further discussed in [6]. The traces represent Chu's limit for a single and a dual mode ESA as a function of ka. 2

1.2 Two stem plots of degenerate mode parametric amplifcation (left) and non-degenerate paraemtric amplification. In the degenerate case, there is a harmonic at a frequency f_{i} that overlaps with the signal frequency f_{s}, which disrupts receiving communication signals. Since that harmonic and the signal no longer overlap in the non-degenerate case, there is no disruption from the harmonic frequency. 4

3.1 Theoretical circuit representing cross-frequency interactions on nonlinear capacitor due to multiple input signals of differing frequency. 15

3.2 This figure shows the reduced, idealized circuit to produce non-degenerate parametric amplification (left) with an illustrative example of its frequency content (right). 17

3.3 Implementation of Figure 3.1 to create a parametric amplifier using a TVC model. 19
3.4 This figure shows the reduced, idealized circuit to produce degenerate parametric amplification (left) with an illustrative example of the frequency content of the phase coherent case (middle) and the phase incoherent case (right). 23
3.5 Transducer gain of #1 versus load resistance and 1/Q of the LTI resonators 26
3.6 Frequency versus gain for designs #1, #2, and #3. 28
3.7 Normalized gain across frequency of designs #3 and #4. 29

4.1 The antenna is modeled as a Thévenin equivalent impedance and the plane wave is modeled as a voltage source. 33
4.2 The impedance plot shows an example of how the circuit model captures the antenna's impedance across frequency. The solid line is the input impedance of the loop described in section 4.2 and the dashed lines are the narrowband approximations of the loop using Equation (4.2). 35
4.3 Dimensions of the LTI concentric loop used for this chapter. When referring to the single loop without the inner loop, the physical dimensions are the same as shown here with the inner loop deleted. . . 40
4.4 Input impedance of the concentric loop antenna (Cloop) and the outer loop by itself (Loop). The input impedance at second series resonances is improved by the presence of the inner loop for the purpose of parametric tuning. 41

4.5 Received power across frequency of the LTI receiving antenna, and the antenna with the non-degenerate (ND) parametric tuning, the phase coherent (PC) degenerate tuning, and the phase incoherent (PI) degenerate tuning. Each design is simulated using CMMoM (solid line), HB (dashed line), and a transient (markers) solver. The discontinuous markers on the plot correspond to the degenerate points of the degenerate designs, and an additional marker is used for the HB and CMMoM simulations at these points since the power received is calculated using the idler and signal harmonics and not just the signal harmonic. 48

4.6 The EVM as a function of bitrate (left) and the step response (right) of the LTI antenna and the three parametrically tuned antennas. The ND receiver configuration outperforms all three, while the LTI outperforms the PC and PI configurations. 50

4.7 The IQ diagrams at a bitrate of 0.12 $\mathrm{Ms/s}$ are shown for the LTI (a), non-degenerate (b), phase coherent (c), and phase incoherent (d) cases. The IQ diagrams for a bitrate of 4.8 $\mathrm{Ms/s}$ is also shown for the LTI (e), and non-degenerate (f) cases. 51

4.8 Maximum gain for a fixed bandwidth (left) is calculated using equations (4.13) and (4.16), the optimizer in (4.5.2), and a CM model using the component values determined by the optimizer. Gain as a function of frequency (right) of the two designs labeled 1 and 2, calculated using CM and equation (4.8). 55

4.9 Effects of loss at the idler frequency on gain and bandwidth for increasing ratios of idler subcircuit loss over signal subcircuit loss. . 56

4.10 Effects of loss at the idler frequency on gain and bandwidth for increasing ratios of idler subcircuit loss over signal subcircuit loss. . 56

5.1 Circuit model of the single-balanced parametric amplifier. 58
5.2 Gain across frequency of the single balanced parametric amplifier against design #1. 61
5.3 Currents at all simulated harmonics with $f_{\mathrm{s}} = 90$ MHz of the single-balanced parametric amplifier. 62
5.4 Dimensions of the loop used for the single balanced parametrically tuned receiver. 63
5.5 The power received across frequency of the single balanced, parametricaly tuned ESA (SB) and that ESA tuned with an LTI capacitor. 64

6.1 Generalized parametric amplifier diagram for broadbanding. 67
6.2 Schematic of the Butterworth coupling network-based parametric amplifier. 69
6.3 Frequency versus gain of the Butterworth coupling network-based parametric amplifier. 71
6.4 73
6.5 The flowchart for developing a second order filtenna. 73
6.6 Geometry of antenna after design stage in subsection 6.3.3 75
6.7 Geometry of first resonator after design stage in subsection 6.3.4. . . 76
6.8 The first external quality factor, associated with the CLL, as a function of Γ-match arm length ℓ_{Γ}. 77

6.9 Figure a) shows the four steps in the TDR tuning stage: step 1) first external quality factor, step 2) first resonator's resonance, step 3) inter-resonator coupling, step 4) antenna's resonance. Figure b) shows the full filtenna with the element spacing and total ka. 78
6.10 Fabricated antenna (left) and measurement setup (right) used for the measured results. 79
6.11 S_{11} normalized to the resonant frequencies f_0 (a) and radiation patterns at the resonant frequencies (b) of the simulated and measured results of the filtenna. 79
6.12 The layout of the asymmetric filtenna with updated dimensions is shown here. Any unlabeled dimensions are unchanged from the symmetric design. 80
6.13 Comparison of the realized gain and scattering parameters for the asymmetric (As.) and symmetric (Sym.) designs. 81
6.14 The power across frequency for the LTI and nLTI filtenna compared to the ND design from chapter 4. 83

7.1 Example non-Foster circuit from [72] where the input impedance will allow the circuit to pass the second stability criterion while failing Rollet's Proviso. 88
7.2 Diagram of the circuit model used to compare to the antenna is shown in 7.2a with the corresponding component values, and the input impedance of the purely real frequency MoM model and the circuit model compared in 7.2b. 92

7.3 Comparison of the complex frequency domain representation of the dipole antenna using sMoM (left) compared to that of the equivalent circuit model of the input impedance (right) 93
7.4 Comparison between the Laplace transform of the time-domain model and the sCM model of the time-varying capacitor. 94
7.5 Two dimensional input impedances of the stable LTI (7.5a) antenna, the potentially unstable non-LTI (7.5b & 7.5c) antenna, and the potentially unstable non-LTI case (7.5d) with $a = 0.1$. 96
7.6 Input impedance at $\alpha = 0$ of a stable (7.6a) LTI antenna and the input impedance of the unstable (7.6b & 7.6b) non-LTI antenna. Figure 97

8.1 Comparison of the non-degenerate (cLoop ND) and single balanced (sLoop SB) antennas to the maximum achievable bandwidths for their radiation efficiencies (cLoop max at 0.58 and sLoop max at 0.43, respectively), the LTI concentric loop (cLoop LTI), the LTI square loop (sLoop LTI), and an optimized version of the ND case (cLoop Opt). The two loops and accompanying bounds are also compared to the projected performance of a planar meandered dipole [65]. 100

Abstract

Electrically small antenna (ESAs) are a fundamental component of size-constrained communication systems. Digital devices also play an important role in modern communication systems, and significant improvements to digital hardware over the past 50 years has resulted in increased performance and size reduction of the digital components. However, ESAs themselves suffer from fundamental physical limitations, often making them the single most restrictive component on modern communications systems' performance and size. Some researchers have turned to using nonlinear and time-varying (non-LTI) devices to circumvent the bandwidth limits on ESAs to improve signal throughput. Most of these efforts have been on transmitting systems, and converting these solutions to receivers is often unfeasible. This work addresses the lack of novel methods for circumventing the bounds on ESA performance by leveraging classic parametric amplification to tune ESAs to resonance while improving their bandwidth. Using multiple simulation methods, three different parametrically tuned antennas are designed and analyzed, with one resulting in a sixfold increase in bandwidth compared to the same antenna without the parametric tuning. Additionally, a model is established for parametrically tuned ESAs, and is used to analyze the optimal performance for such antennas.

Chapter 1

Introduction

1.1 Backgound

Electrically small antennas (ESAs) are important for communication systems with limited platform sizes, but have fundamental limits on their minimum attainable radiation quality factor and radiation efficiency [1], [2], [3], [4], [5] which impacts their ability to transmit and receive communication signals. These limits were explored in [1] and formally defined in [2], where the minimum quality factor (Q factor, or just Q) and maximum antenna gain G to Q ratio were defined using a number of $TE_{n,0}$ or $TM_{n,0}$ far field modes and the size of a circumscribing sphere for an arbitrary antenna. Minimizing Q is critical as it is inversely proportionate to bandwidth, and a larger bandwidth means more information the antenna can either transmit or receive at any given time. Since then, minimum attainable antenna quality factors have been further investigated, including derivation of useful approximations [3], reexamined for accuracy [4], and extension to arbitrary geometries instead of a circumscribing sphere [5].

Due to the widespread use of ESAs there has been much work in maximizing their performance. There has been a litany of novel structures that approach the bound on gain and bandwidth [6]. Figure 1.1 is included to emphasize the amount of

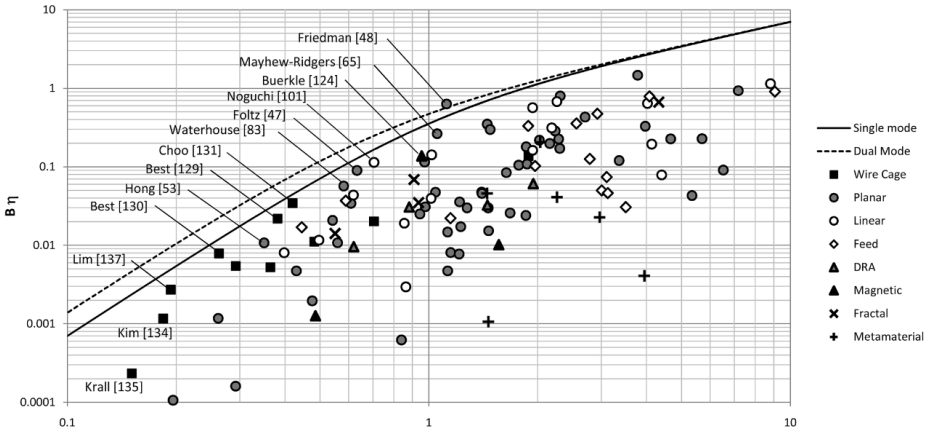


Figure 1.1: The radiation efficiency-bandwidth product of several passive, LTI ESAs from literature plotted as a function of the electrical size (x-axis) of the circumscribing sphere around them ka [6]. Some of the designs that came the closest to the bound are marked with the author and a citation number, and further discussed in [6]. The traces represent Chu's limit for a single and a dual mode ESA as a function of ka.

effort placed in optimizing the performance of passive, LTI ESAs, and comes from the review in [6]. Each marker in Figure 1.1 is the radiation efficiency-bandwidth product of a passive, LTI ESA in literature as a function of the electrical size of the circumscribing sphere about the antenna ka and the traces are the Chu limit for a single and dual mode ESA. There has also been work on optimizing the antenna's Q and gain within a fixed area [7], [8], [9], or utilizing multiple resonant modes [10] to circumvent Chu's limit [2]. Some work focuses on the matching network instead of the antenna alone, like investigations into self-resonant versus tuned ESAs [11] and optimizing wideband matching networks to ESAs [12].

All of the previously mentioned ESAs only focus on maximizing the antenna performance within their physical limits, but are still constrained by limits on quality factor and radiation efficiency. A more recent strategy is to use nonlinear and time-varying (non-LTI) components to circumvent the limits on gain and bandwidth of electrically small antennas. Some methods use fast switching to directly modu-

late the antenna with the signal [13], [14]. Other methods focus on improving the matching network from the antenna to the rest of the system by using fast switching to prevent reflections from the antenna back to the system [15] and active components to create non-Foster matching networks [16]. Another method looks at using time-varying reactances to achieve gain and and bandwidth improvements. Time-varying reactances have been used to achieve parametric frequency conversion with ESAs [17], [18], [19] and degenerate mode and sub-harmonic parametric amplification [20], [21], [22], [23] either on the aperture of the antenna, at the feed, or as part of the matching network.

The major drawback of many of these non-LTI, time-varying systems is that they generally only operate well as transmitters. One example is that modulating the antenna directly with fast switching requires that the switch be driven by the signal itself - this would not be possible on a receiving system. Another example is a switching method like [15] which is specifically designed for transmit architectures as this system is meant to synchronize with pulses coming from a transmitter such that the energy from the pulses cannot be reflected back and continues to be radiated by the antenna instead.

1.2 Parametrically Tuned, Electrically Small Receiving Antennas

Like with fast switching, application of TV reactances for ESAs has also been restricted to transmit system or frequency converting systems [17], [18], [19], [20], [22], [23]. In the case of transmitting systems, most ESAs loaded with a TV reactance implement degenerate mode parametric amplification, whose basic frequency domain representation is illustrated in Figure 1.2a. The issue with degenerate mode

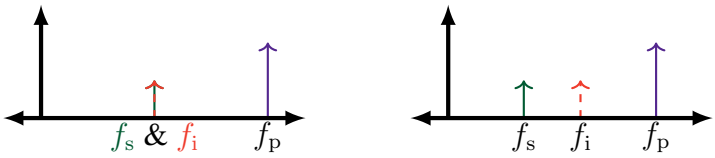


Figure 1.2: Two stem plots of degenerate mode parametric amplifcation (left) and non-degenerate paraemtric amplification. In the degenerate case, there is a harmonic at a frequency f_i that overlaps with the signal frequency f_s, which disrupts receiving communication signals. Since that harmonic and the signal no longer overlap in the non-degenerate case, there is no disruption from the harmonic frequency.

parametric amplification is that, due to the selection of the time-varying reactance's oscillating frequency f_p, the first difference harmonic frequency f_i between the time-varying reactance and the signal is nearly or exactly the same as the signal frequency f_s [24]. This results in the first difference harmonic and signal directly interacting, which greatly interferes with received signals [25].

Non-degenerate parametric amplification, however, mitigates this issue but has not been implemented with ESAs. Non-degenerate parametric amplification is illustrated in Figure 1.2b, which shows how the harmonic and signal now differ significantly in frequency and no longer interact. Since the harmonic and signal frequencies no longer interact in that way, non-degenerate parametric amplification could be used with receivers for communication [25].

In this dissertation, the lack of solutions incorporating TV reactances for circumventing the limitations of ESAs on receive is addressed by leveraging non-degenerate parametric amplification. Specifically, the bandwidth of a receiving ESA is increased beyond its LTI bandwidth by using a TVC to tune it to resonate and simultaneously achieve non-degenerate parametric amplification. The second chapter briefly covers the analysis methods used here. The third chapter covers the

theory behind classic parametric amplification, discusses the gain-bandwidth limitations of circuital parametric amplifiers, and then investigates those limits with some examples. The observations made from this section help illustrate strategies for improving the performance of parametrically tuned ESAs. The fourth chapter covers designing a parametrically tuned ESA loaded with a time-vary capacitance. This chapter includes derivations and analysis of generalized gain and bandwidth equations and a gain-bandwidth relationship for parametrically tuned ESAs, a method for designing and tuning parametrically tuned ESAs using observations from the derived equations, and an example of a parametrically tuned ESA. Chapter five investigates improving the bandwidth of the parametrically tuned ESA by using a single balanced topology for the TVC. This chapter looks at the theoretical enhancements with a classic, circuit implementation, and a single-balanced, parametrically tuned ESA whose bandwidth is an improvement over the previous chapter. The sixth chapter uses a filtenna as the ESA instead of a singly-resonant antenna to further increase the bandwidth, which includes looking at a circuit implementation like the previous chapters and then at a parametrically tuned ESA version. The seventh chapter explores a method of testing the stability of distributed, time-varying structures. Finally, chapter eight concludes the work and discusses future goals.

Chapter 2

Analysis tools

This chapter is an overview of the different analysis tools used to produce all simulated data and any closed-form equations derived in later chapters. The methods include full-wave electromagnetic solvers to calculate the antenna's response, calculations of time-varying systems in MATLAB and commercial, off-the-shelf (COTS) circuit simulators to model the behavior of the antenna and the non-LTI components, and a receiver model including an equalizer to analyze the performance of the parametrically tuned antennas with a realizable signal.

2.1 Full-wave simulation methods

This section discusses the two full-wave, electromagnetic solvers used throughout this work. Unless otherwise stated, all antennas are simulated in free space as two dimensional conductive sheets that are either perfect electric conductor (PEC) or a finite conductivity of 5.95×10^7 Ωm to simulate a copper conductor [26]. The type of conductor used will be stated for each case.

To simulate the LTI antenna with the non-LTI components, voltage source(s) are needed to represent the incoming plane wave at the ports. A single port is used when the non-LTI element is at the feed of the antenna, but two ports are needed

when the non-LTI element is placed elsewhere on the aperture of the antenna. This is done to represent the differences in voltage between two separate locations on the antenna, and to represent the coupling performed by the antenna between the feed and the non-LTI element. For either full-wave solver, the antenna is excited by a plane wave co-polarized with the antenna incoming from whatever angle achieves its maximum effective aperture.

2.1.1 Method of moments using antenna toolbox for MATLAB

The antenna toolbox for MATLAB (AToM) is a method of moments (MoM) solver and is used for most of the antenna experiments [27]. It is easy to include in analysis since it is directly integrated into MATLAB. MoM calculates induced currents along the metallic structure from an applied voltage.

The MoM simulations used a "pixel-grid" mesh where two triangular mesh elements are used to construct each square element. The simulations used Rao-Wilton-Glisson (RWG) basis functions with a integration quadrature order of five.

The MoM impedance model and voltage vector from the plane wave excitation were then compressed using the theory of Shur Complement [28]. The impedance and voltage were compressed down to only the number of ports loaded with either the load impedance of the receiver or a non-LTI element. In most cases this would be two ports, one for the feed network and one for the non-LTI load. When used with a COTS SPICE simulation, the impedance matrix is converted into an S-parameter matrix and the voltages were modeled as voltage sources in series with the non-LTI element and the load.

2.1.2 Finite element method using High Frequency Structure Simulation

High frequency structure simulator (HFSS) is a widely used RF structure solver [29], and is used to design the electrically small filtenna discussed in chapter 6. The results of HFSS simulations can also be exported as touchstone files and loaded with time-varying (TV) elements in another simulation software.

Since the amount of frequency content required for the TV system is unreasonably large for a standard HFSS simulation, the structure is simulated multiple times over portions of the total desired bandwidth. Each simulation could then have an appropriately sized radiation boundary box and solution frequency. Each simulation swept far enough that it would overlap with the adjacent frequency sweeps, and the touchstone data is averaged across the overlap to smooth the transition between each simulation.

The HFSS simulation used interpolating frequency sweeps for the touchstone data, and a single plane wave simulation at the signal frequency to extract the voltages at each port of the structure. The simulations all used the iterative solver with a relative residual of 10^{-6}, a second order basis function, and lambda refinement for the initial mesh of $\lambda \leq 0.1$ relative to the solution frequency of each simulation.

The antenna simulated in HFSS was exported as a two port, Z-parameter network. This is accomplished by simulating the antenna terminated with 50 Ω lumped ports where the feed and capacitor should be and exporting the Z parameters. Another simulation is conducted with both ports left as open circuits and the voltage across them is calculated. These voltages are then used as voltage sources in the SPICE simulations at either port of the Z-parameter network representation of the antenna. This method is similar to the one verified in [22].

2.2 Conversion matrices

Conversion matrices (CM) is a modeling method for TV discrete components that uses phasor representations of the voltage, current, and TV circuit element to represent the element as a impedance matrix where each frequency is a port [28], [30]. These conversion matrices were used in tandem with MoM impedance matrices to create conversion matrices method of moments (CMMoM) models of the antenna loaded with TV circuit components. CM is also used in Chapter 4 to analyze a circuit model representation of a parametrically tuned antenna. Since CMMoM with compressed impedance matrices is very computationally efficient it was used as the initial step in the simulation process, where applicable.

2.3 SPICE

The TV antennas were simulated in CMMoM initially, and then validated using harmonic balance and transient SPICE simulations in Advanced Design Systems (ADS) [31]. The SPICE model for a TV reactance can be found in [32].

2.3.1 Harmonic Balance

Harmonic balance (HB) is a circuit solver that partitions a circuit into its LTI and non-LTI components to calculate non-LTI circuits. Since it is relatively fast it acted as an intermediate validation tool in which tuning the TV antenna occurred. Since the systems being simulated were only TV, the harmonic order of the signal frequency stayed at one, while the harmonic order of the second frequency initially started at six, but if disagreement occurred between the HB and transient SPICE simulations, this order number would be increased to improve the accuracy of the

simulation. To capture all non-negligible harmonics, a maximum mixing order is set to be one integer higher than the harmonic order of the second frequency. Additionally, the "robust" convergence method is used with "max. iterations" set to "robust," and the Krylov simulator matrix solver is used.

2.3.2 Transient

Transient SPICE simulations calculate the currents and voltages at discrete time steps. This method is significantly longer than CM and HB, so it is best used as the last step in the design process. Despite the runtime it captures instability and other phenomenon not immediately captured by the other two simulation methods, making it an important facet of the validation process. All settings used were default, except that the convolution method is set to "strict."

2.4 Receiver and Equalizer

In chapter 4 a receiver model is used to verify the actual signal fidelity of some TV antennas. This is particularly important as the instantaneous bandwidth in the frequency domain of a non-LTI system might not accurately represent the actual effects it has on a signal, as there may be interactions between harmonics or transient phenomenon that degrades the signal quality but is not apparent when analyzing total received power across frequency. A 256 symbol long 16-QAM digital modulation scheme is used, as it would illustrate the effects of the non-LTI system on both amplitude and phase as a function of time.

To measure the error vector magnitude (EVM) of a TV antenna, the step response of the TV antenna is simulated in the transient SPICE simulation at the phase of each symbol of the modulation scheme. The step responses are then imported

into MATLAB, where a pseudo-random symbol sequence (PRBS) is generated and convolved with a train of step responses that matched the appropriate phase of each symbol. This PRBS is then fed through receiver and equalizer model, and the EVM of the signal is measured.

Since the here PSRB uses QAM, the receiver was designed to filter the signal, split the signal into in-phase and quadrature components, and then filter again so the baseband response could be sampled by an equalizer model. The receiver model begins with receiving the unaltered PRBS fed into a bandpass filter using the MATLAB function `bandpass()`. The filter has a center frequency of 120 MHz, a passband bandwidth of 40 MHz, and a transition width of 0.7. This signal is then sent into two mixers oscillating at the center frequency, each 90° out of phase with one another to produce the in-phase and quadrature signals. A 20^{TH} order lowpass butterworth filter is then constructed using the `butter()` function, and each of the signals are filtered using the `filtfilt()` function. The in-phase and quadrature components are then sampled and white noise is added using the `awgn()` function to represent the cumulative internal noise of the receiver components. The white noise was 30 dB below the peak power, resulting in a peak SNR of 30 dB. The equalizer object is then called and the final signal is processed and the EVM is calculated.

The equalizer itself is an adaptive linear equalizer [33]. A least means square algorithm is used for training the equalizer with a step size of 0.001. The equalizer had ten taps and took two samples per symbol, with the first tap used as the reference. Several symbol rates were used, but the energy in the signals of varying symbol rates were normalized as the amount of energy in each signal changes as a function of symbol rate. This energy is normalized to the amount of energy in the 256 symbol PRBS of the slowest symbol rate for each TV antenna simulation to

more fairly compare the EVM of each symbol rate in terms of only inter-symbol interference. External noise is neglected for this experiment, as it should be relatively low compared to the internal noise as these frequencies [34].

2.5 Conclusion

This section covered the general methods of how the designs were simulated. The antenna's are modeled using full-wave simulations, and then the full, TV systems are modeled by importing compressed impedance matrices into circuit simulations that include the TV components. In the circuit models, both frequency and time domain calculations are completed to verify the accuracy of each simulation and ensure stability. In some cases, signal fidelity experiments are also done to understand the signal throughput improvements of the parametrically tuned ESAs. In other sections, CM is used to derive closed form equations instead of outright simulation with an MoM network representation of an antenna. The next chapter reviews classic parametric amplifier theory to lay the groundwork for the parametrically tuned antennas.

Chapter 3

Classic parametric amplifier theory

This chapter is an overview of classic parametric amplifier theory. The purpose of this chapter is to impart an understanding of basic parametric amplifier principles, which are leveraged in later chapters to improve the bandwidth of ESAs. Additionally, some of the observations about maximizing the gain-bandwidth product of a standard parametric amplifier are compared to the circuit analysis of a parametrically tuned ESA in the next chapter.

First, the governing, cross-frequency Manley-Rowe power relations are explained in Section 3.1 with a discussion on the underlying mechanics that produce negative resistance gain using a nonlinear capacitance. Section 3.2 reviews a classic circuit implementation of a non-degenerate, negative resistance parametric amplifier. The review includes previously derived transducer gain and gain-bandwidth equations. Section 3.3 briefly discusses the theory of degenerate mode parametric amplification. Following the review, section 3.4 utilizes the circuit model, gain equation, and gain-bandwidth equations from section 3.2 to analyze four different parametric amplifier configurations to understand how the circuit parameters influence the non-degenerate amplifier's gain and bandwidth.

3.1 Manley-Rowe Relations

While parametric resonance has been around since the 1830s [35], it was first formally introduced into electrical systems with the work of [24]. In [24], a set of cross-frequency, power conservation equations named the Manley-Rowe relations were derived. This section highlights some important points in [24] to setup the explanation of parametric amplification in preceding sections.

The authors of [24] described the interaction of a signal frequency f_{s} and a pumping frequency f_{p} on a nonlinear capacitor, but they also noted that these relations hold for a nonlinear inductor. Figure 3.1 is a circuital representation of these two sources and all possible harmonics that occur. In the circuit, power at each harmonic is isolated to a respective resistance using an ideal bandpass filter that permits only one harmonic and rejects all others completely. Series voltage sources with a resistance in each branch represent the real power that exists at each frequency. For this circuit, power can be generated at, or delivered to, a frequency using the series voltage source and resistor. Designing a parametric circuit usually focuses on only the signal and pumping sources generating power, while all branches have their voltage sources shorted. However, it is important to consider that in practice the higher frequency voltage sources will not be zero in the presence of noise or interferers.

Using this ideal circuit from Figure 3.1 the following relations were derived,

$$\sum_{m=0}^{\infty}\sum_{n=-\infty}^{\infty}\frac{mW_{m,n}}{mf_{\mathrm{s}}+nf_{\mathrm{p}}}=0 \tag{3.1a}$$

$$\sum_{m=-\infty}^{\infty}\sum_{n=0}^{\infty}\frac{nW_{m,n}}{mf_{\mathrm{s}}+nf_{\mathrm{p}}}=0 \tag{3.1b}$$

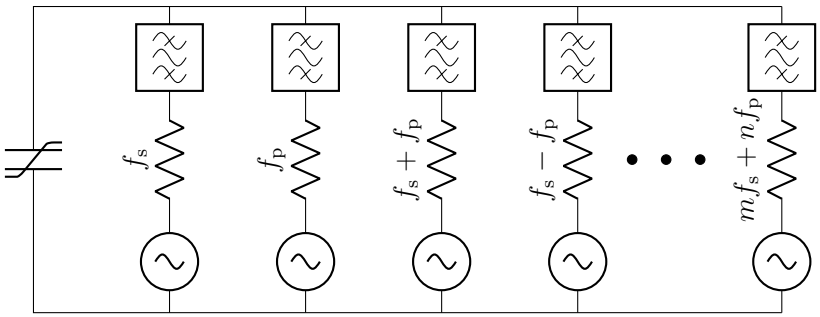


Figure 3.1: Theoretical circuit representing cross-frequency interactions on nonlinear capacitor due to multiple input signals of differing frequency.

where m and n are indices referring to the integer multiple of either the source or pumping frequency, and $W_{m,n}$ is the power at the harmonic frequency $mf_\mathrm{s} + nf_\mathrm{p}$. These power conservation expressions were used in [24] to show the transfer of power for inverting and non-inverting modulators and demodulators. For these examples, it was assumed that no current flows along any of the branches except for the pumping and signal frequency along with either the first sum harmonic $f_\mathrm{s} + f_\mathrm{p}$ or the first difference harmonic $f_\mathrm{s} - f_\mathrm{p}$, often referred to as the idler. The authors also placed the restrictions that the pumping frequency was greater than the signal frequency and the pumping power was much greater than the signal power. Section 3.2.1 and 3.3 demonstrate how this ideal analysis of equations 3.1 can be used to amplify power at the signal frequency.

3.2 Parametric amplification

This section describes how a classic parametric amplifier operates by examining the works of [24], [36], [37], [38]. All equations in this section, unless otherwise stated, come from [36]. The focus of this section is on non-degenerate parametric amplification, where the idler frequency is sufficiently higher than the signal frequency such that the idler frequency falls into the stopband of the signal fre-

quencies' branch and the bandwidth of the signal and idler do not overlap at all. The case where this is not true is referred to as degenerate mode parametric amplification, and is briefly described in section 3.3.

3.2.1 Non-degenerate parametric amplification

Consider the simplified circuit in Figure 3.2a, where the idler is the only harmonic at which current flows through the nonlinear capacitor. Using equation (3.1) for the case where current flows on the nonlinear capacitor at the signal, idler, and pump frequency, it can be shown that the power at the pump is positive while both the power at the idler frequency and signal frequency are negative. This means that instead of the reactance absorbing power from the signal it is instead generating power at the signal and idler frequency. This particular phenomenon is the source of negative resistance parametric amplification.

The version of Manley and Rowe's idealized circuit shown in Figure 3.2 results in a non-degenerate parametric amplifier, and will generate current on the nonlinear capacitor similar to the sketch in Figure 3.2b. As illustrated in Figure 3.2b, the current at the signal with some bandwidth exists at a lower frequency than the idler, which is a conjugated copy of the signal. In the non-degenerate parametric amplifier, only the signal current will flow on the signal branch of the circuit, and only the idler current will flow on its respective branch. Overall, both the circuit model and stem plot in Figure 3.2 demonstrate how the currents at the signal and idler frequencies do not directly interact with one another, and only indirectly interact with cross-frequency coupling through the nonlinear capacitor.

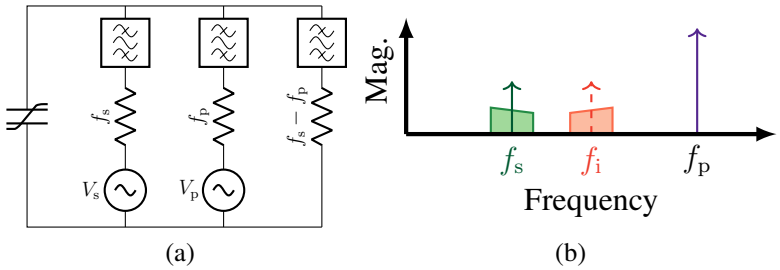


Figure 3.2: This figure shows the reduced, idealized circuit to produce non-degenerate parametric amplification (left) with an illustrative example of its frequency content (right).

3.2.2 Non-degenerate parametric amplification circuit analysis

The equations in (3.1) are useful to describe what is theoretically possible and the fundamental limitations on power transfer across frequency, however, they do not completely describe practical circuit behavior. Instead, it is typical to analyze a parametric amplifier circuit model by representing the cross-frequency power transfer from the pump and idler frequencies down to the signal frequency as a negative resistance. This section introduces a circuit model and uses it to calculate transducer gain from a power source (comprised of a voltage source and generator resistance R_g) to a load resistance R_ℓ. This transducer gain equation is then used to derive peak gain and bandwidth equations, which are subsequently maximized to create a theoretical limit for the gain-bandwidth product.

The first step in parametric amplifier circuit analysis is to assume that pumping power is sufficiently larger than the signal so the system is only weakly nonlinear. This assumption allows the nonlinear capacitor and pumping signal to be represented as a single time-varying capacitance (TVC), such that

$$C(t) = C_0(1 + 2\gamma \sin(w_p t) + 2\gamma_2 \sin(2w_p t) + 2\gamma_3 \sin(3w_p t) + \ldots) \tag{3.2}$$

where C_0 is the static or mean capacitance of the TVC, $\gamma \in [0, 1/2)$ is the modulation factor of the TVC at the pumping frequency ω_p, and the subsequent sinusoidal terms and modulation factors represent possible higher order harmonic frequency components of the TVC. The higher order terms (γ_2, γ_3,... at $2\omega_\mathrm{p}$, $3\omega_\mathrm{p}$,...) are negligible if the nonlinear capacitance's curve as a function of voltage is at least approximately linear in the region of operation. Any simulations in this work only have a non-zero γ for the fundamental TVC pumping tone.

Unlike the nonlinear capacitor model, the TVC model can be analyzed using small signal analysis. With small signal analysis, it can be shown that when the impedance of the TVC with an external circuit is purely real at the passband center frequency f_s and idler center frequency f_i simultaneously, a negative resistance appears at and around the passband's center frequency [36], [37], [38]. This negative resistance is due to the inverse of the impedance at the idler frequency appearing at the signal frequency and the magnitude of the cross frequency impedance of the TVC itself $|Z| = |V_\mathrm{s}/I_\mathrm{i}|$.

A classic implementation of a negative resistance parametric amplifier, including the TVC and external circuitry to cancel out the reactances at the signal and idler frequencies, is shown in Figure 3.3. All currents at the unwanted harmonics (any frequencies other than the signal and idler) are presented an open with the circuit in Figure 3.3 [36]. Since a realizable TVC component would have some series resistance, it is modeled in Figure 3.3 using the resistor R_c. The series resistance of the capacitor is important to model since it captures that currents at the unwanted harmonic frequencies never see a true open.

The circuit utilizes a series resonator at the idler band comprised of an inductance L_i, a capacitance C_i, and some loss R_i, and a resonator at the signal band made of an inductance L_s, a capacitance C_s, and some other loss R_s. These res-

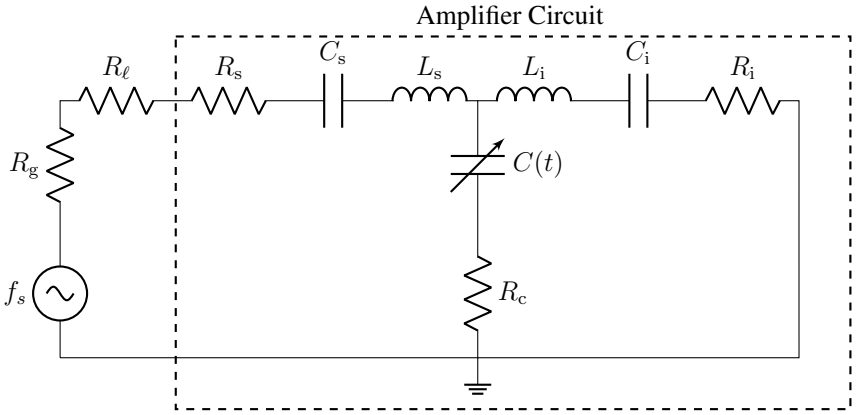


Figure 3.3: Implementation of Figure 3.1 to create a parametric amplifier using a TVC model.

onators act both as filters to isolate the unwanted harmonics from the load and TVC and to cancel out the reactance of the TVC at the passband's resonant frequency f_s and the idler's resonant frequency f_i. The generator at the signal frequency is represented as a series voltage source and a generator impedance R_g and is in series with the load impedance R_ℓ. In the examples in this chapter the loss of the signal band resonator is combined into the load impedance. This is an accurate choice when the signal frequency resonator is a part of the load, but is less accurate when the resonator is a separate component from the load. This is also approximately true whenever $R_\mathrm{s} << R_\ell$.

Analyzing the circuit in FIgure 3.3 using small signal analysis shows the transducer gain G_t with the idler and signal circuits resonating simultaneously is

$$G_\mathrm{t} = \frac{4R_\ell R_\mathrm{g}}{\left[R_\mathrm{s}^\mathrm{net} - R_-\right]^2}. \tag{3.3}$$

The resistance $R_\mathrm{s}^\mathrm{net}$ represents all loss present at the resonant frequency, which is $R_\mathrm{s}^\mathrm{net} = R_\mathrm{g} + R_\ell + R_\mathrm{s} + R_\mathrm{c}$ [36]. The negative resistance R_- due to the idler

impedance coupling into the signal is

$$R_{-} = \frac{\gamma^2}{\omega_1 \omega_2 C' R_2^{\text{net}}} \tag{3.4}$$

where the effective capacitance C' is $C' = C_0(1-\gamma^2)$ and the loss seen at the idler frequency is $R_2^{\text{net}} = R_{\text{c}} + R_{\text{i}}$ [36]. The effective capacitance is due to slight detuning in the mean capacitance and should be used instead of the static capacitance when calculating the component values for the resonators. Equations (3.3) and (3.4) are fundamental in designing a parametric amplifier as they show the max gain achievable at resonance for a design, and the negative resistance term specifically informs on how to tune the TVC for amplification. Furthermore, the condition $R_1^{\text{net}} > R_{-}$ can be used to predict if the amplifier is stable, and it is most likely stable when it the inequality is met.

3.2.3 Amplifier bandwidth

Modeling the transducer gain across frequency requires modeling the frequency dependent impedance instead of assuming the entire circuit is resonant like in equation (3.3). Instead of modeling the entire impedance across frequency, the impedance of the circuit isolated to a narrow bandwidth around the signal and idler frequency is used. The impedance of the circuit about the signal frequency Z'_{s} is the sum of the impedance of the signal tank Z_{s} and the TVC's impedance X_{c}, where the impedance of the circuit about the idler frequency Z'_{i} is the sum of the idler tank Z_{i} and the TVC.

Since these resonances are series, a linear, narrowband approximation is implemented using the quality factor of the total circuit at the signal frequency Q_1 and at

the idler frequency Q_2 such that the impedances can be modeled as

$$Z'_{\mathrm{s}} = Z_{\mathrm{s}}(\omega \approx \omega_{\mathrm{s}}) + Z_c(\omega \approx \omega_{\mathrm{s}}) = R_{\mathrm{s}}^{\mathrm{net}}(1 + j2\delta_{\mathrm{s}}Q_{\mathrm{s}}), \tag{3.5a}$$

$$Z'_{\mathrm{i}} = Z_{\mathrm{i}}(\omega \approx \omega_{\mathrm{i}}) + Z_c^*(\omega \approx \omega_{\mathrm{i}}) = R_{\mathrm{i}}^{\mathrm{net}}(1 - j2\delta_{\mathrm{i}}Q_{\mathrm{i}}). \tag{3.5b}$$

Normalized frequency $\delta_{\mathrm{s/i}}$ is used so the expressions can model an amplifier regardless of any specific operating frequency. The normalized frequency across the bandwidth of the signal δ_{s} is defined as $\delta_{\mathrm{s}} = (\omega - \omega_{\mathrm{s}})/\omega_{\mathrm{s}}$, and the normalized frequency for the idler resonant frequency δ_{i} is $\delta_{\mathrm{i}} = -\omega_{\mathrm{s}}/\omega_{\mathrm{i}} \cdot \delta_{\mathrm{s}}$. Solving for the transducer gain using this approximation results in

$$G_{\mathrm{t}} = \frac{4R_{\mathrm{g}}R_{\ell}}{\left[Z'_{\mathrm{s}} - \frac{R_-}{1-j2\delta_{\mathrm{i}}Q^{\mathrm{C}}{}_{\mathrm{i}}}\right]^2}. \tag{3.6}$$

Equation (3.6) shows that the lower the Q of the resonators the less the gain decays across the frequency. However, increasing the Q does not only increase the bandwidth of the gain, but also influences the maximum gain as well. In [36] there is the relationship

$$G_{\mathrm{t}}\mathrm{b}^2 = \frac{4R_{\mathrm{g}}R_{\ell}/(R_{\mathrm{s}}^{\mathrm{net}})^2}{Q^{\mathrm{C}}{}_1 + \frac{\omega_{\mathrm{s}}}{\omega_{\mathrm{i}}}Q^{\mathrm{C}}{}_{\mathrm{i}}} \tag{3.7}$$

That represents the gain-bandwidth product for a high gain parametric amplifier. According to an example in [36] 20 dB of gain is sufficiently high for equation (3.7) and is the standard for the analysis in this chapter.

To find the absolute theoretical limit for the gain-bandwidth product, equation (3.7) can be maximized. The minimum possible quality factor at the signal and idler frequencies is that of the TVC itself Q^{C}, so by assuming that this quality factor has been achieved and the load and generator resistances are selected to

maximize power transfer, the gain-bandwidth relationship becomes

$$G_{\mathrm{t}}\mathrm{b}^2 = \frac{1}{\left[Q_{\mathrm{s}}^{\mathrm{C}} + \frac{\omega_{\mathrm{s}}/\omega_{\mathrm{i}}}{\gamma^2 Q_{\mathrm{s}}^{\mathrm{C}}}\right]^2}. \tag{3.8}$$

This equation can be further reduced by noting that it is maximized when

$$Q_{\mathrm{s}}^{\mathrm{C}} = \sqrt{\frac{\omega_{\mathrm{s}}}{\omega_{\mathrm{i}}}}\frac{1}{\gamma}. \tag{3.9}$$

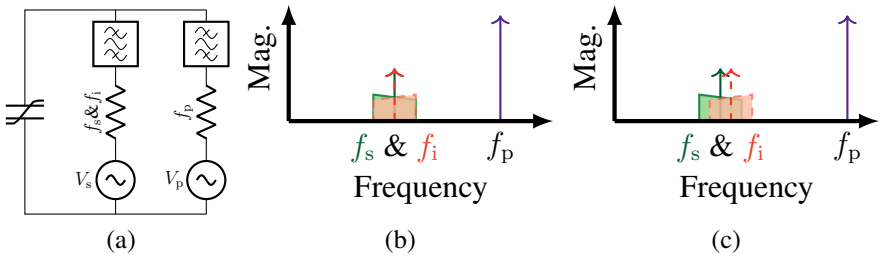
Using these two relationships the the absolute maximum achievable gain-bandwidth product can be found with

$$(G_{\mathrm{t}}^{1/2}\mathrm{b})_{\max} = \frac{\gamma}{2}\sqrt{\frac{\omega_{\mathrm{i}}}{\omega_{\mathrm{s}}}}. \tag{3.10}$$

This gain-bandwidth product assumes the amplifier is operating in a high gain state. When this quality factor is not achieved or when the load and generator do not match the maximum attainable gain-bandwidth product will not be reached.

3.3 Degenerate mode parametric amplification

A parametric circuit similar to the non-degenerate parametric amplifier is the degenerate parametric amplifier, illustrated by the alternative Manley-Rowe circuit model shown in Figure 3.4a. Unlike the non-degenerate case the signal and idler frequencies share a branch because they are now close enough in frequency that they fall within the same passband. The degenerate mode class of parametric amplifiers can be split into two sub-categories: one is phase-coherent such that the pumping frequency is exactly twice the resonance of the signal circuit and the other is phase-incoherent where the pumping frequency is nearly twice the resonant frequency of



(a) (b) (c)

Figure 3.4: This figure shows the reduced, idealized circuit to produce degenerate parametric amplification (left) with an illustrative example of the frequency content of the phase coherent case (middle) and the phase incoherent case (right).

the signal circuit but not exactly equal.

Phase-coherent degenerate amplification is illustrated in Figure 3.4b [36]. However, because the signal and idler frequencies exactly equal the magnitude of the total current at that frequency is a function of the relative phase between the idler and signal. Because of the relative phase relationship between the signal and idler, the total power at that frequency can range anywhere from 6 dB higher than that of the signal power by itself or tens of dB lower than the non-degenerate case [25].

The phase-incoherent case can further improve the bandwidth, but it introduces other complications as well. As shown in Figure 3.4c, the bandwidths between the signal and idler overlap asymmetrically and can result in significant distortion of the signal. Even if the signal bandwidth is reduced so the signal and idler do not overlap, the close proximity of the two can result in a beat frequency that is difficult to filter out. Chapter 4 illustrates the issues with degenerate mode parametric amplification by comparing two degenerate, parametrically tuned antennas to a standard LTI antenna and one non-degenerate, parametrically tuned antenna.

Table 3.1: Component values for classic, singly resonant parametric amplifiers

Des.	$R_\ell(\Omega)$	L_s(nH)	C_s(pF)	L_i(nH)	C_i(pF)	C_0(pF)	γ	Q_i	Q_i
#1	1.45	961	13.03	100.14	0.331	4.01	0.05	164.96	168.32
#2	1.405	724.7	134	75.3	0.453	4.01	0.05	130.38	129.95
#3	6.76	970.5	13.44	100.26	0.331	3.99	0.2	40.22	40.87
#4	6.76	961	13.03	100.14	0.331	4.01	0.05	39.94	40.82

3.4 Non-Degenerate Parametric Amplifier Examples

This section uses both the transducer gain equation (3.6), and SPICE simulations to analyze four variations of a non-degenerate parametric amplifier. All the amplifiers were of the same design as in Figure 3.3 with component values listed in Table 3.1. The purpose of comparing the four designs to one another is to highlight the impact of different design choices on overall performance in relation to the maximum possible bandwidths achievable with each design. Some of these observations will be related to parametrically tuned ESAs in the following chapter.

3.4.1 Design

The design of the parametric amplifiers begins with selecting a modulation factor and static capacitance. The values here were chosen so that the designs in this work could be realized using a varactor from the Skyworks SMV123X varactor diode series [39]. The cutoff frequency for these diodes is 10 GHz, and the corresponding inductance was neglected since the pumping frequency of 1 GHz was low enough that the varactor would still appear as a capacitance and not a resonator. The series resistance R_c could not be neglected like the inductance since parametric amplifiers are sensitive to changes in resistance, and was selected to be 0.5 Ω. The resonant frequency for the signal passband was selected to be 90 MHz, as this is

not a multiple of, and is much lower than, the pumping frequency. Unless specified otherwise, all simulations in this chapter used this loss with the TVC, a modulation factor of 0.05, and the same frequencies for the resonance of the signal band and the pump. These values were left the same wherever possible since they affect the maximum gain-bandwidth product and could skew the comparison if changed between every design.

With these values selected, the component values for the series resonators could be calculated. For these examples, they were tuned so both the idler and signal resonators had nearly identical Q's to limit the impact of differing Q's on amplifier performance. This was done since the resonator with the smallest Q is the limiting factor in bandwidth and gain, and plays a role in some broadbanding techniques [40], [41], [42]. Finally, the ideal load resistance could be calculated. This was accomplished by sweeping values of load resistance as shown in Figure 3.5. Such a plot doubles as a stability analysis, as the only stable load resistances will be those to the right of the peak gain where the resistance at the signal band exceeds the negative resistance. Using Figure 3.5 a load resistance for the first amplifier was selected to be 1.45 Ω, and resulted in approximately 20 dB of gain. While the HB and TR simulations agreed within 0.1 dB, the analytical model's gain curve was shifted 0.115 Ω to the right. Slight error was expected, as the analytical expressions assumed that the amplifier used ideal filters such that all unwanted harmonics are presented a perfect open [36], [43]. For the gain across frequency plots in this section, the analytical calculation used a load resistance shifted up for the R^{net}, R_{g}, R_{ℓ}, and R_{-} terms in equations (3.6) and (3.7) to accommodate this inaccuracy. The error of under 0.5 dB between the analytical results and the simulated results in Figure 3.6 and the agreement in the calculated bandwidth in Table 3.2 indicate this diagnosis of the inaccuracy was correct. The second and third amplifiers in this

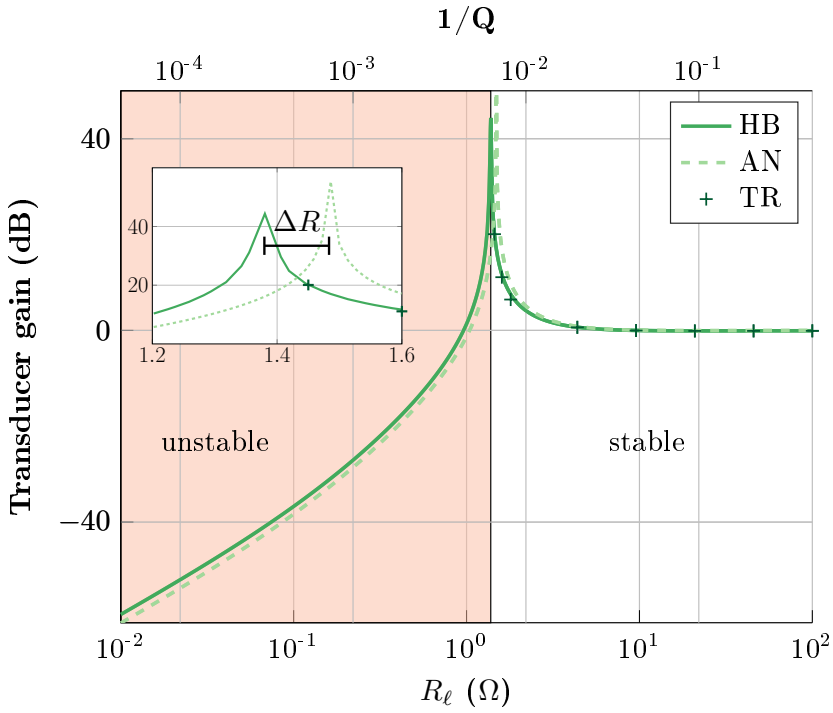


Figure 3.5: Transducer gain of #1 versus load resistance and 1/Q of the LTI resonators

section follow the same design procedure, with the second having a lower Q for both the signal and idler resonators and the third having a higher modulation factor. The fourth was the first design but with a load resistance matching the third design.

Table 3.2: Performance of singly resonant parametric amplifiers.

Design	G_t (dB)	b% (sim.)	b% (calc.)	b% (max)	b% (theor.)
#1	20.10	0.048	0.050	0.064	0.393
#2	19.91	0.063	0.063	0.064	0.393
#3	20.12	0.221	0.221	0.295	1.567
#4	0.15	2.42	2.41	3.01	-

3.4.2 Discussion

The first two examples had identical negative resistance, but their resonators were tuned to have different Q's. The gain across frequency of Design #1 and #2 is shown in Figure 3.6. In Figure 3.6, the HB and TR traces indicate their respective simulation methods, while the analytical (AN) traces represent the gain calculated using equation (3.6). Table 3.2 shows the gain and bandwidths of all the designs, including the simulated bandwidth, the bandwidth calculated using the Q of the resonators and equation (3.7), the maximum bandwidth if the Q of the circuit is only based on the TVC as in equation (3.11), and the theoretical maximum calculated from equation (3.10). The maximum bandwidth was calculated by using the minimum attainable Q, limited by the TVC, for each resonator

$$\mathrm{Q}_{\mathrm{s}}^{\min} = 1/(\omega_{\mathrm{s}} C' R_{\mathrm{s}}) \tag{3.11a}$$

$$\mathrm{Q}_{\mathrm{i}}^{\min} = 1/(\omega_{\mathrm{i}} C' R_{\mathrm{i}}) \tag{3.11b}$$

with equation (3.7). Design #2 approaches the maximum bandwidth with it's lower Q, as its Q is very near the Q of the TVC. The maximum attainable bandwidth of 0.064% for designs #1 and #2 cannot be increased further with the coupling network design in Figure 3.3 for a particular TVC, but according to the theoretical maximum there is still room for improvement.

Design #3 demonstrates the bandwidth improvement of increasing the modulation factor of the parametric amplifier to decrease the TVC's Q without losing gain. This occurred because of the increased negative resistance from the higher modulation factor, and it allowed the amplifier to support 20 dB with a higher load resistance. According to Table 3.2 design #3 seems no closer to approaching the

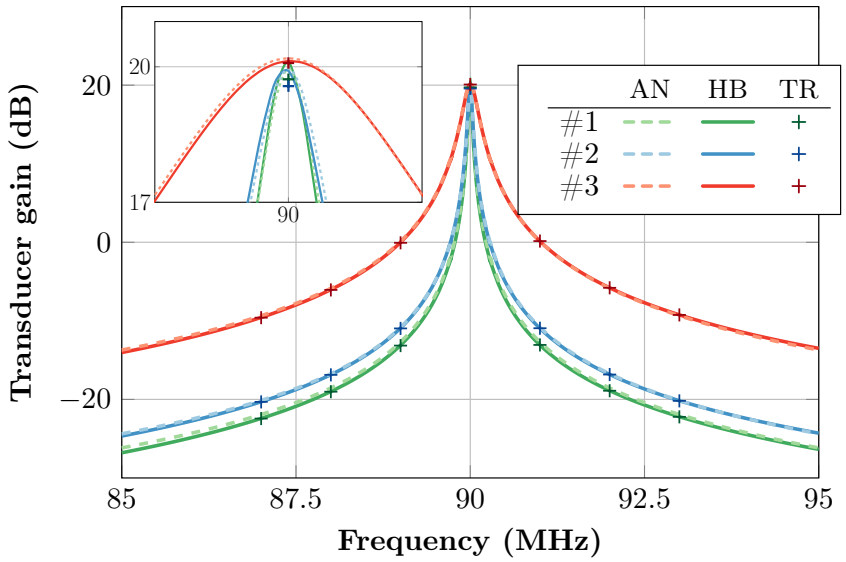


Figure 3.6: Frequency versus gain for designs #1, #2, and #3.

theoretical maximum, as its maximum possible bandwidth was still much lower than the theoretical maximum, meaning that an increase in modulation factor can increase the overall bandwidth but will not use more of the theoretically possible bandwidth.

Designs #3 and #4 are compared together in the normalized plot in Figure 3.7 to illustrate that just loading the amplifier further will improve the bandwidth with a significant sacrifice in gain. The theoretical maximum was derived using the high gain assumption and was not applicable to the design #4 configuration. Figure 3.7 also emphasizes the nonlinear relationship between Q and gain, and suggests that it is best to operate a parametric amplifier with moderate to high gain and seek bandwidth increases other than resistive loading for the best gain-bandwidth product.

Generally speaking, there is significant difference between the maximum achievable bandwidths and the theoretical bandwidths in Table 3.2. The theoretical maximum values in Table 3.2 are calculated using equation (3.10), where the losses are completely neglected, the minimum quality factors were reached, and the ideal

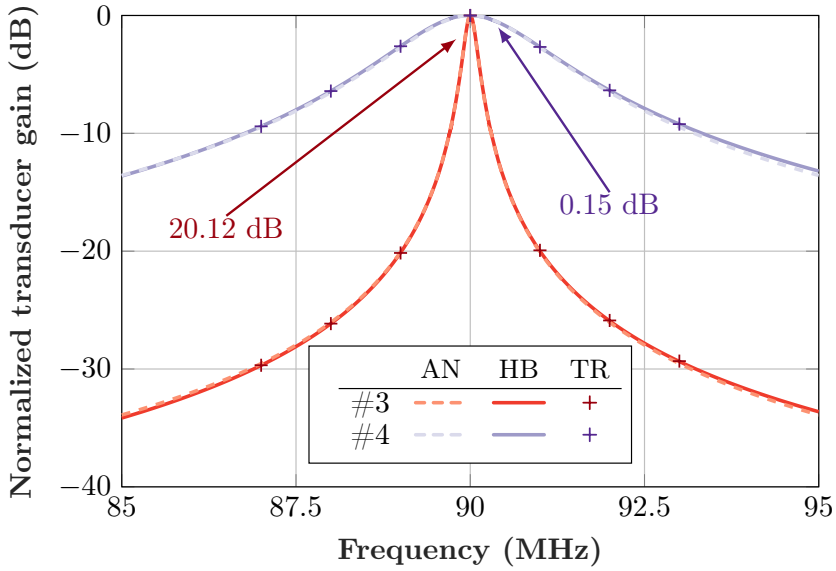


Figure 3.7: Normalized gain across frequency of designs #3 and #4.

load resistance was used. The maximized bandwidth, on the other hand, calculated the maximum achievable bandwidth for the each amplifier using the full expression (3.7) where the quality factors only realized on the reactive energy stored in the TVC. This means that the idler and signal loss are non-negligible. Therefore, without using alternative parametric amplifier configurations or increasing the modulation factor, the primary way of increasing the maximum bandwidth of any of these amplifiers would require a decrease in loss.

3.5 Conclusion

This chapter covered a standard model of circuital parametric amplifiers to understand the effects of different component values on the gain and bandwidth of the amplifier. These effects were also compared to a previously derived gain-bandwidth product to understand the ways in which the performance of a parametric amplifier may reach the theoretical maximum gain and bandwidth. The next chapter extends

the review here to parametrically tuned ESAs by deriving a set of gain and bandwidth equations for the parametrically tuned antenna, demonstrating the feasibility of a parametrically tuned ESA with a realizable example, and analyzing the theoretical maximum gain and bandwidth achievable.

Chapter 4

Classic parametrically tuned electrically small receiving antennas

This section investigates how a TVC can be used to tune an ESA to resonate and also enhance the gain and bandwidth using parametric amplification. The circuit implementation in chapter 3 used two separate resonators for the signal and idler bands, but the parametrically tuned ESA instead uses two resonances of the antenna tuned with the ESA. While an independent resonator can be used for the idler sub-circuit, this work focuses on the case where a higher order, radiating resonance is used.

This chapter first constructs and analyzes a circuit model of a lossless, parametrically tuned antenna, and derives a transducer gain equation from that circuit model. The transducer gain equation is then used to provide some design guidelines for the antenna itself to optimize the gain and bandwidth of the parametric tuning. Using the observations about optimizing the ESA performance, a proof-of-concept example is created using an MoM model of an antenna with CM, HB, and TR simulations. A non-degenerate, phase coherent, and phase incoherent version of the parametrically tuned ESA are simulated and compared, both in instantaneous power received as a function of frequency and in signal fidelity using a time-domain

simulation with a PRBS. After the antenna design and discussion, the circuit model is revisited and the gain and bandwidth are optimized for the circuit model of the parametrically tuned ESA. The optimization is validated and the effects of antenna resistance at the idler frequency and modulation factor on the optimized gain and bandwidth are studied.

4.1 Modeling and analysis of parametrically tuned receiving antennas

4.1.1 Circuit model

The circuit model for the parametrically tuned ESA is similar to the circuit model in chapter 3, but with some key differences. The parametrically tuned ESA is modeled using the circuit in Figure 4.1. There are two resonators $RLC_{\mathrm{s/i}}$ to model the antenna's input impedance around the signal and idler frequencies. However, unlike the circuital parametric amplifier, the parametrically tuned ESA discussed here has the TVC $c(t)$ and its loss R_{c} placed in series with the load resistance R_{L}, which represents the rest of the receiver, and voltage source V_0. This represents how the feed of the antenna sees the TVC even when the antenna is not resonant. There are two ideal filters in series with each RLC branch to decouple the two resonators, and to represent the assumption that currents at all frequencies aside from the signal and idler frequencies are negligible. The voltage source V_0 and the antenna's input resistance at the signal frequency together represent the power received by the antenna, where V_0 is open circuit voltage [44].

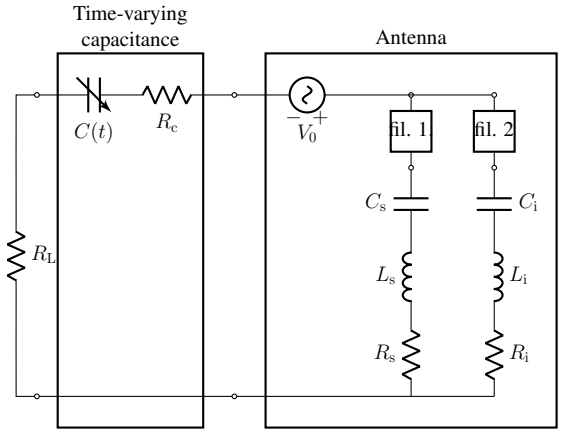


Figure 4.1: The antenna is modeled as a Thévenin equivalent impedance and the plane wave is modeled as a voltage source.

The TVC is modeled similarly to the previous chapter where

$$c(t) = C_0(1 + \gamma \cos(\omega_p t)) \tag{4.1}$$

using the average capacitance C_0 and the modulation factor $\gamma \in [0, 1)$ which represents the swing in capacitance across a single period. Note that there are no higher order harmonics of the pump, which assumes that the nonlinear capacitance used must have an approximately linear C-V curve in the region of operation.

The impedance for each resonator also uses a linear approximation like in the previous chapter, where the impedances are represented by

$$Z_{s/i} = R^{net}_{s/i}(1 \pm j2\delta_{s/i}Q_{s/i}), \tag{4.2}$$

using the loaded quality factors of the total circuit $Q_{s/i}$ and the net resistances $R^{net}_{s/i}$,

$$R^{net}_{s/i} = R_L + R_{s/i} + R_c, \tag{4.3}$$

at each resonance. Frequency is normalized to the deviation from resonance for the signal band $\delta_{\mathrm{s}} = (\omega - \omega_{\mathrm{s}})/\omega_{\mathrm{s}}$ and the idler band $\delta_{\mathrm{i}} = (\omega - \omega_{\mathrm{i}})/\omega_{\mathrm{i}}$. The resistances $R_{\mathrm{s/i}}$ represent the antenna's input resistance at the signal and idler frequencies. Equation (4.2) is important as it allows the resonators to be described regardless of particular frequencies and reactances. This circuit model also assumes that the idler resonance can re-radiate power and is visible to the feed of the antenna, which may not always be true.

An example of using the circuit in Figure 4.1 to model the input impedance of an ESA is shown in Figure 4.2. The solid lines are the real and imaginary parts of the input impedance of the antenna described in section 4.2 tuned with the first resonance at 100 MHz using a 4.5 pF capacitor. The dashed and dotted lines are the impedance approximations using equation (4.2) for the signal and idler resonators. The white areas signify the passbands of each of the ideal filters placed with the resonators, and the gray areas represent the frequencies where the antenna circuit model presents an open circuit.

Since the $f_i = f_s - f_p$ and $f_p > f_s$, the idler frequency f_i is negative, as shown in Figure 4.1 and reflected in the minus sign for $\Im(Z_{\mathrm{i}})$ in equation 4.2. Calculations in this work use the positive frequency $|f_i|$ and account for the negative frequency by taking the complex conjugate of the current and voltage terms at the idler frequency.

4.1.2 Analysis

In this section, the transducer gain at the signal frequency of the parametrically tuned ESA circuit model is calculated using a CM representation [28], [30]. Trans-

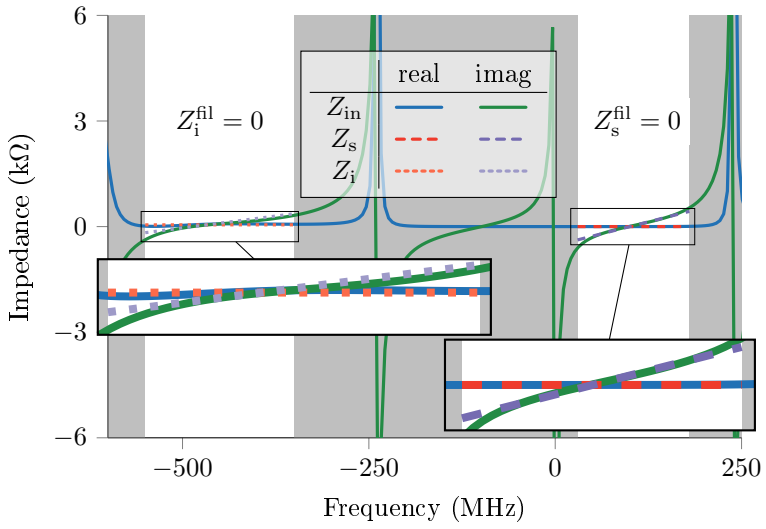


Figure 4.2: The impedance plot shows an example of how the circuit model captures the antenna's impedance across frequency. The solid line is the input impedance of the loop described in section 4.2 and the dashed lines are the narrowband approximations of the loop using Equation (4.2).

ducer gain [45] is defined as

$$G_{\mathrm{t}} = \frac{P_{\mathrm{L}}}{P_{\mathrm{av}}} = \frac{4R_{\mathrm{L}}R_{\mathrm{s}}|I_{\mathrm{s}}|^2}{|V_0|^2}, \tag{4.4}$$

or the ratio of the power dissipated into the load resistance over the power available from the voltage induced by a plane wave on the feed of the antenna. The gain formula is then used to determine an equation for half-power fractional bandwidth at the signal frequency.

To solve for transducer gain, an equation for current must be derived. By using CM [28], [30] to create impedance matrices for the TVC $\hat{\mathbf{Z}}_{\mathrm{C}}$, the load $\hat{\mathbf{Z}}_{\mathrm{L}}$, and the antenna $\hat{\mathbf{Z}}_{\mathrm{a}}$, a system of equations can be formed to solve for the current at the signal frequency. The CM-derived impedance matrix of the TVC in equation (4.1)

is

$$\hat{\mathbf{Z}}_{\mathrm{C}} = \left(\mathrm{j}C_0 \begin{bmatrix} \omega_{\mathrm{s}} & 0 \\ 0 & -\omega_{\mathrm{i}} \end{bmatrix} \begin{bmatrix} 1 & \gamma/2 \\ \gamma/2 & 1 \end{bmatrix} \right)^{-1} = \begin{bmatrix} \frac{1}{\mathrm{j}\omega_{\mathrm{s}} C_1} & \frac{\gamma}{\mathrm{j}2\omega_{\mathrm{i}} C_1} \\ \frac{-\gamma}{\mathrm{j}2\omega_{\mathrm{s}} C_1} & \frac{-1}{\mathrm{j}\omega_{\mathrm{i}} C_1} \end{bmatrix}. \tag{4.5}$$

The TVC is modeled as a virtual two-port device in equation (4.5), with one virtual port at the signal frequency and one at the idler frequency. The diagonal terms of the matrix are the usual LTI definition of impedance $Z_{mn} = V(\omega_m)/I(\omega_n)|_{m=n}$ while the off-diagonal terms are cross-frequency impedance terms $Z_{mn} = V(\omega_m)$ $/I(\omega_n)|_{m\neq n}$.

A by-product of the impedance matrix derivation is the effective static capacitance term $C_1 = C_0(1 - \frac{1}{4}\gamma^2)$, which corresponds to the detuning of the LTI static capacitance at both the signal and idler frequencies from modulating the capacitance. When the diagonal impedance terms of the TVC impedance matrix (Z_{11} and Z_{22}) are put in terms of the effective static capacitance C_1 instead of the initial static capacitance C_0 the diagonal impedance terms mirror the usual definition of impedance for a capacitor $Z = 1/\mathrm{j}\omega C$. Therefore, the effective static capacitance should be used as the capacitance when calculating things like resonant frequency for the circuit model of the parametrically tuned ESA.

The impedance matrices of the load and antenna can be derived using CM as well, and by representing the induced voltage as a vector $\hat{\mathbf{V}}_0 = [V_0,\ 0]^T$ a system of equations can be derived

$$\hat{\mathbf{V}}_0 = \left(\hat{\mathbf{Z}}_{\mathrm{a}} + \hat{\mathbf{Z}}_{\mathrm{C}} + \hat{\mathbf{Z}}_{\mathrm{L}} \right) \hat{\mathbf{I}} = \hat{\mathbf{Z}}^{\mathrm{net}}\, \hat{\mathbf{I}}, \tag{4.6}$$

to find the currents at the signal and idler frequency in the vector form $\hat{\mathbf{I}} = [I_{\mathrm{s}},\ I_{\mathrm{i}}^*]^T$. The matrices $\hat{\mathbf{Z}}_{\mathrm{a}}$ and $\hat{\mathbf{Z}}_{\mathrm{L}}$ refer to the CM impedances for the antenna circuit model and the load resistance, respectively. The current and voltages at the idler frequency

are conjugated since the idler frequency is less than zero. By conjugating the current and voltage, the system of equations can be put in terms of only positive frequencies to simplify calculation. Solving for the current at the signal frequency results in

$$I_{\mathrm{s}} = \frac{V_0}{Z_{1,1}^{\mathrm{net}} - Z_{1,2}^{\mathrm{net}} Z_{2,1}^{\mathrm{net}} / Z_{2,2}^{\mathrm{net}}} = \frac{V_0}{Z_s - \frac{\gamma^2}{4\omega_{\mathrm{s}}\omega_{\mathrm{i}} C_1^2 Z_{\mathrm{i}}}}. \tag{4.7}$$

Using the definition of transducer gain in equation (4.4) and the current from equation (4.7), the transducer gain can be written as

$$G_{\mathrm{t}} = \frac{4R_{\mathrm{L}}R_{\mathrm{s}}|I_{\mathrm{s}}|^2}{|V_0|^2} = \frac{4R_{\mathrm{L}}R_{\mathrm{s}}}{\left[Z_{\mathrm{s}} - \frac{R_-}{1 - j2\delta_{\mathrm{i}}\mathrm{Q_i}}\right]^2}, \tag{4.8}$$

where the negative resistance term R_- is

$$R_- = \frac{\gamma^2/4}{\omega_s\omega_i C_1^2 R_{\mathrm{i}}^{\mathrm{net}}} = \frac{\gamma^2/4}{\omega_s C_1} Q_{\mathrm{i}}^{\mathrm{TVC}}, \tag{4.9}$$

which represents the gain generated by the cross-frequency interaction of power flowing between the idler and signal frequencies. The quality factors $Q_{\mathrm{s/i}}^{\mathrm{TVC}}$ are the loaded quality factors of the TVC at the signal and idler frequency, respectively.

To solve for the half-power fractional bandwidth, an equation for peak transducer gain is needed. Transducer gain is maximized when the impedance at the signal frequency is purely real. Therefore, the peak gain can be found by setting the normalized frequency variables $\delta_{\mathrm{s/i}}$ in equation (4.8) to zero in equation (4.8). Reducing the transducer gain this way results in

$$G_{\mathrm{t}} = \frac{4R_{\mathrm{L}}R_{\mathrm{s}}}{(R_{\mathrm{s}}^{\mathrm{net}})^2 \left[1 - R_-^{\mathrm{N}}\right]^2}. \tag{4.10}$$

where $R_-^{\mathrm{N}} = R_-/R_{\mathrm{s}}^{\mathrm{net}} = \gamma^2 Q_{\mathrm{s}}^{\mathrm{TVC}} Q_{\mathrm{i}}^{\mathrm{TVC}}/4$ is the normalized negative resistance.

The normalized negative resistance can also serve as a stability criterion, where the system is stable if

$$R_{-}^{\mathrm{N}} = \gamma^2 Q_{\mathrm{s}}^{\mathrm{TVC}} Q_{\mathrm{i}}^{\mathrm{TVC}}/4 = R_{-}/R_{\mathrm{s}}^{\mathrm{net}} < 1. \tag{4.11}$$

The half-power fractional bandwidth Δ_{G} of the system can be obtained from the frequency-dependent transducer gain in equation (4.8) by setting it equal to half of the maximum transducer gain in equation (4.10) and solving for $\Delta_{\mathrm{G}} = 2\delta_{\mathrm{s}}$. Writing the half power fractional bandwidth Δ_{G} as a function of the normalized negative resistance, the loaded quality factors of the system at the signal and idler resonances Q_{s} and Q_{i}, and the idler-signal frequency ratio $r_\omega = \omega_{\mathrm{i}}/\omega_{\mathrm{s}}$ results in

$$\Delta_{\mathrm{G}} = \frac{r_\omega(1-a)/Q_{\mathrm{i}}}{\sqrt{(a + r_\omega \frac{Q_{\mathrm{s}}}{Q_{\mathrm{i}}})^2 - (3a^2 - 4a + 1)}}. \tag{4.12}$$

4.2 Antenna design

This section discusses design choices for the ESA that will result in a higher negative resistance term, meaning that more power can be transferred to the incoming signal for a fixed modulation factor. This section then uses those observations to design a loop antenna.

Taking the negative resistance R_{-} and assuming that the signal frequency and static capacitance are held constant, then the two main factors in raising the negative resistance are the modulation factor and the loaded quality factor of the TVC at the idler frequency $Q_{\mathrm{i}}^{\mathrm{TVC}}$. If the modulation factor is also fixed then the only practical way to influence the negative resistance is through the loaded quality factor of the TVC at the idler frequency. Therefore, two design goals for designing an ESA

to be parametrically tuned are two lower the idler resonant frequency and lower the antenna's resistance at the idler to increase the negative resistance for a fixed modulation factor.

As mentioned in chapter 3, it is best to minimize the loaded quality factor of the total system $Q_{\mathrm{s/i}}$ to that of the TVC $Q^{T}TVC_{\mathrm{s/i}}$. Since the TVC is used to tune the ESA to resonance, if the antenna is sufficiently detuned without the TVC then the energy stored in the total system at the signal frequency is inherently equal to that of the TVC. Therefore, by using parametric tuning with an ESA the minimum quality factor at the signal frequency is inherently achieved at the signal frequency.

Designing the ESA A loop was chosen as the radiator [26], [46] since it is easily tuned to resonate using a capacitance and the open space within the antenna can be used to house the parametric circuitry in a later iteration of the design. Since the parametric amplification needs two resonance to operate, the first series resonance is used for the signal, and a higher order series resonance is used for the idler. The loop is a balanced structure and does come with the added obstacle of incorporating a balun for measurement and any applications where the feeding structure of the antenna is unbalanced [26], [47]. However, many unbalanced structures require a ground plane which can add an extra layer of complexity to the design as the ground plane should ideally be very electrically large. Since the preferred electrical size for the ground plane is unachievable while maintaining the electrically small size constraint, a balanced structure is preferred despite the need for a balun.

While the resistance of the first resonance of an ESA is usually small, the higher order series resonances will have significantly higher resistance [48]. As discussed earlier in this section, the lower the resistance of the idler resonance the higher the negative resistance for a fixed modulation factor. Therefore, reducing the input

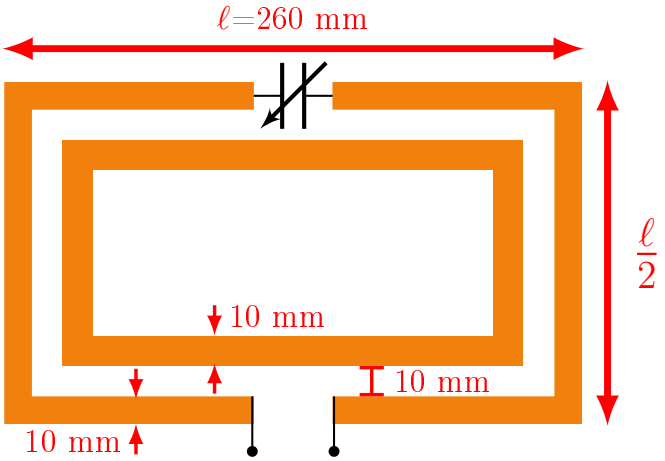
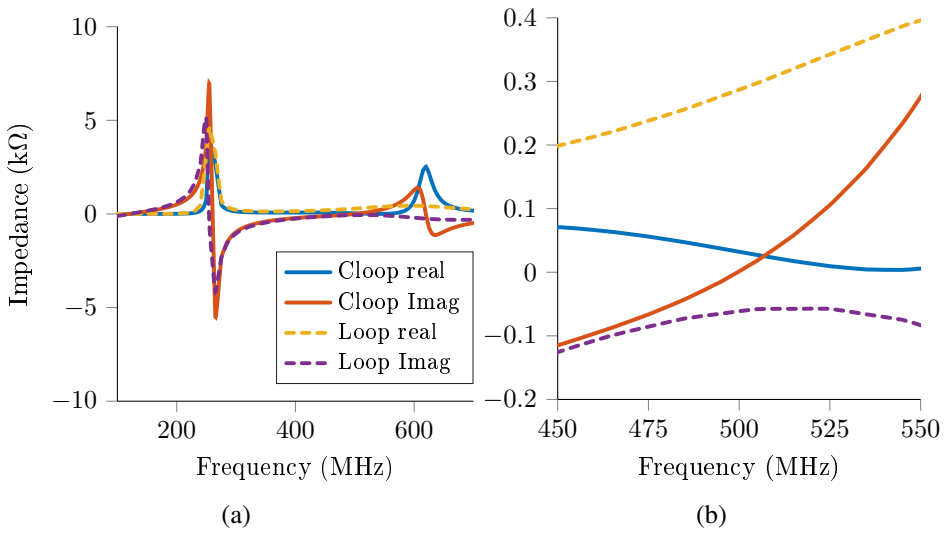


Figure 4.3: Dimensions of the LTI concentric loop used for this chapter. When referring to the single loop without the inner loop, the physical dimensions are the same as shown here with the inner loop deleted.

resistance of the antenna at a higher order resonance will improve the efficiency of the amplification by increasing the negative resistance without increasing the modulation factor.

Lowering the resistance of the higher order mode is achieved here by using a smaller loop within the main loop to create a concentric loop antenna, where the inner loop resonates with the outer loop at one of the outer loop's higher order resonances. Figure 4.3 shows the dimensions of a 2 to 1 concentric loop with a ka of 0.37, and tuned to resonate at 120 MHz with a static capacitance of 2.6 pF. Figure 4.4 compares the input impedance of the outer loop antenna with and without the inner loop. The first resonance is largely unchanged by the inner loop, however the second series resonance and second anti-resonance are changed drastically. With the additional inner loop, the antenna is able to completely resonate at the second series resonance unlike the single loop antenna, and the input resistance about the second series resonance at 500 MHz of the concentric loop is decreased sig-



(a) (b)

Figure 4.4: Input impedance of the concentric loop antenna (Cloop) and the outer loop by itself (Loop). The input impedance at second series resonances is improved by the presence of the inner loop for the purpose of parametric tuning.

nificantly to 31 Ω from the standard loop's input resistance of 287 Ω at the same frequency.

4.3 Non-degenerate parametric amplification design

4.3.1 Overview of the design process

With the antenna designed, the parametric tuning process can begin. First, the choice of whether or not the signal band will be around a series or anti resonance must be made. Here, a series resonance is used since the first resonance of a loop antenna is a series resonance, and based on the previous observations about the negative resistance, the second series resonance should be used to minimize the idler frequency. Regardless of choice, the idler resonance must be the same kind of resonance as the signal resonance. This is necessary to properly negate out currents at unwanted harmonics [36]. Next, the static capacitance that tunes the antenna to

resonate must be found. The LTI tuning capacitance is used as the starting point for the tuning process, and may change depending on the modulation factor. The change in static capacitance based on the modulation factor can be predicted by the effective capacitance, but adjustments will need to be made to fine tune the antenna.

Before continuing, a varactor diode that can achieve this static capacitance must be selected to avoid creating an unrealizable design. For this design, two Skyworks SMV1233 varactors were used in parallel [39]. Using two varactors in parallel instead of a single varactor with a comparable C-V curve allowed the loss introduced by the TVC to be lower than using a single varactor. The varactor's C-V curve determines the maximum allowable modulation factor based on where on the C-V curve the static capacitance falls and the maximum and minimum capacitance values of the varactor. When selecting a varactor, keep in mind that the nonlinear C-V curve can generate higher order pump frequency harmonics not captured by the single tone TVC model depending on the shape of the C-V curve, the static capacitance, and modulation factor being used. One solution to prevent higher order harmonics is restricting the region of the C-V curve used such that the C-V curve is approximately linear. Another option is to model the possible harmonics with an alternative TVC model that assumes that one or more of the pump frequency harmonics or exist [36].

Next, the load resistance needed to achieve a match at the signal frequency resonance must be determined. This resistance represents the rest of the receiver, and in practice would usually be replaced with some kind of matching network that presents this resistance to the antenna and matches to the line impedance of the rest of the system. The pumping frequency must be set as well, such that the difference harmonic falls within the desired resonance. Here, the second series resonance was used, but higher order series resonances could have be selected for this antenna.

For degenerate parametrically tuned ESAs, the signal frequency resonance will be reused as the idler resonance. The pump frequency itself will most likely not fall within a resonance, so in a practical realization the power source for the pump will need some circuitry to maximize the voltage at the pumping frequency across the varactor.

Tuning process The modeling from section 4.5.2 should be used to predict the approximate values for all the component values. However, some tuning will inevitably be needed to precisely achieve the desired performance. To begin the tuning process, create a model (CMMoM, SPICE, etc.) using the previously determined pump frequency, static capacitance, and load resistance with an initial modulation factor below the intended value. The minimum necessary modulation factor can be predicted using equation (4.9) to check if the negative resistance produced by a given modulation factor is sufficiently high to overcome all the loss at the signal frequency.

Run iterations of the simulation while gradually increasing the modulation factor until the desired gain is achieved. It is important to perform this while sweeping across signal frequency as the frequency response of the antenna may shift. If more bandwidth is desired than what the parametrically tuned antenna produces after this step, then gain can be sacrificed to increase the bandwidth by increasing the matched load resistance. The modulation factor will need to be further increased if the gain drops below the target value.

After the gain and bandwidth have been set, use the static capacitance to retune the antenna's frequency response if any detuning occurred. After adjusting the static capacitance slightly adjust the pumping frequency up and down, if either direction increases the gain, then the pumping frequency should be retuned as the

difference harmonic no longer falls into the idler resonance. The static capacitance should be readjusted throughout the pump frequency tuning process to ensure the frequency response stays centered. This process may result in a gain higher than the target, in which case the modulation factor can be reduced to compensate for this. Again, slight adjustment to the static capacitance may be necessary if the frequency response shifts meaningfully. Check that the final modulation factor and static capacitance are still achievable with the selected varactor. If not, another varactor may need to be chosen. This general process can also be used with parametrically tuned antennas that do not fit the circuit model from Section 4.5.2, and can also be used with realizable simulations that include other elements like baluns, couplers, matching networks, and the pump network.

4.3.2 Non-degenerate design

The parametrically tuned receiving antenna can be designed to increase the receiver's sensitivity, but maximum power received can be traded to increase the bandwidth. The target for the parametrically tuned antenna designs here is to achieve the same maximum power received as the antenna would without the parametric tuning, but with a wider bandwidth. While this may not result in the greatest gain-bandwidth product as demonstrated with the examples in chapter 3, that chapter did show it results in the greatest absolute bandwidth. For an operating frequency of 120 MHz the concentric loop can be tuned to resonate with a capacitance of 2.6 pF. The tuned concentric loop has a second series resonance at approximately 500 MHz, and after tuning resulted in a pumping frequency of 621.2 MHz. The total series loss of the two SMV1233 varactors in parallel is $0.75\ \Omega$, which is noticeably lower when compared to a single SMV1234 varactor with a series resistance of

1.2 Ω. The modulation factor was limited to 0.2 to reduce the production of higher order harmonics. With that modulation factor, the parametrically tuned receiving antenna can be matched to a 7.3 Ω load for a bandwidth increase of 3.2 times that over the same antenna with no parametric tuning. The values for this design and the others are shown in Table 4.1.

4.4 Degenerate parametric amplification

Degenerate parametric amplification has been used to circumvent the lower quality factor bound of electrically small antennas on transmit [20], [22], and is used more in current literature for parametric amplification of RF systems than non-degenerate parametric amplification. This section applies both phase coherent and phase incoherent parametric amplification to two different examples to determine if their increased instantaneous bandwidth will increase signal fidelity over the non-degenerate design. The following sections explain the design changes to the non-degenerate, parametrically tuned antenna to create a phase coherent and phase incoherent degenerate antenna.

4.4.1 Phase coherent

The non-degenerate parametric tuned receiver from the previous section was retuned to operate in a phase coherent, degenerate mode with the same modulation factor and a pumping frequency of exactly 240 MHz. Since the idler falls within the signal band the resistance for the idler drops to 0.7 Ω, greatly improving the efficiency of the negative resistance generated by the TVC. The increased negative resistance results in the parametrically tuned antenna being best matched to a 20.4 Ω, however the bandwidth for the phase coherent design is comparable to that

Table 4.1: This table lists the parameter values for the TVC and load resistance of each case. The phase difference between the TVC and incoming signal ϕ_Δ needed to maximize the power received of the degenerate points of the phase incoherent and phase coherent cases is also listed.

Design	C_0 (pF)	$R_c\ \Omega$	γ	f_p (MHz)	ϕ_Δ (deg)	$R_L\ \Omega$
LTI	2.59 x1	-	-	-	-	0.7
ND	1.32 x2	1.5	0.2	621.2	-	7.3
PC	1.31 x2	1.5	0.2	240.0	78	20.4
PI	1.20 x2	1.5	0.2	238.7	164	9

of the non-degenerate design.

4.4.2 Phase incoherent

The phase coherent degenerate case was altered to operate in a phase incoherent mode where the pumping frequency is 238.7 MHz, such that the degenerate point falls slightly below the resonance of the signal passband. This introduces a slight ripple to the passband, where the two maximas correspond to the resonance in the signal band and to the idler frequency. However, since the design focuses on maximum bandwidth these two maximas are obfuscated, but resulted in more bandwidth than the other two cases.

4.5 Performance comparison

The received power across frequency is shown in Figure 4.5. Each design is simulated using CMMoM, HB, and a TR solver. The points of the transient solution that do not follow the CMMoM and HB traces are the points of degeneracy (or the frequency at which the idler equals the signal) at 120 MHz for the phase coherent and 119.35 MHz for the phase incoherent case. For these simulations the relative phase between the TVC and incoming signal are selected to maximize

the power received, resulting in approximately a 6 dB power increase at the point of degeneracy. The 6 dB power increase corresponds to the voltages of the idler and signal harmonics constructively interfering and doubling the total voltage. The CMMoM and HB power received traces are calculated using the power at the first harmonic, which is sufficient for capturing the behavior of the parametrically tuned antenna for all designs at any frequency other than for the degenerate point. The additional markers for the CMMoM and HB simulations include the contribution from the idler harmonic as well as the signal to capture the signal-idler interaction. The difference between the transient simulation and the other two stays below 1 dB for all points. The concentric loop antenna with only an LTI capacitance achieves a 3 dB fractional bandwidth of 0.5%, while the phase coherent degenerate case and the non-degenerate case have a bandwidth of 1.6% and the phase incoherent degenerate case have a bandwidth of 2.7%. Therefore, considering only the instantaneous bandwidth in the frequency domain, it would appear that the phase incoherent degenerate case is the best at increasing the signal throughput of the receiving antenna.

Signal Fidelity To verify the bandwidth enhancements from the parametric tuning, signal fidelity experiments were undertaken on each design. If the signal fidelity experiment is considered instead of the instantaneous bandwidth, then issues arise as shown in Figure 4.6a. Both the phase coherent (PC) and phase incoherent (PI) designs cannot maintain an EVM of less than 30% and are outperformed by the LTI case for all symbol rates. The non-degenerate (ND) design performs similarly to the LTI antenna at lower symbol rates, however, as the symbol rates increases the ND antenna begins to outperform the LTI case. From 1.2 Ms/s to 4.2 Ms/s, the ND maintains an EVM of approximately three times lower than that of the LTI case -

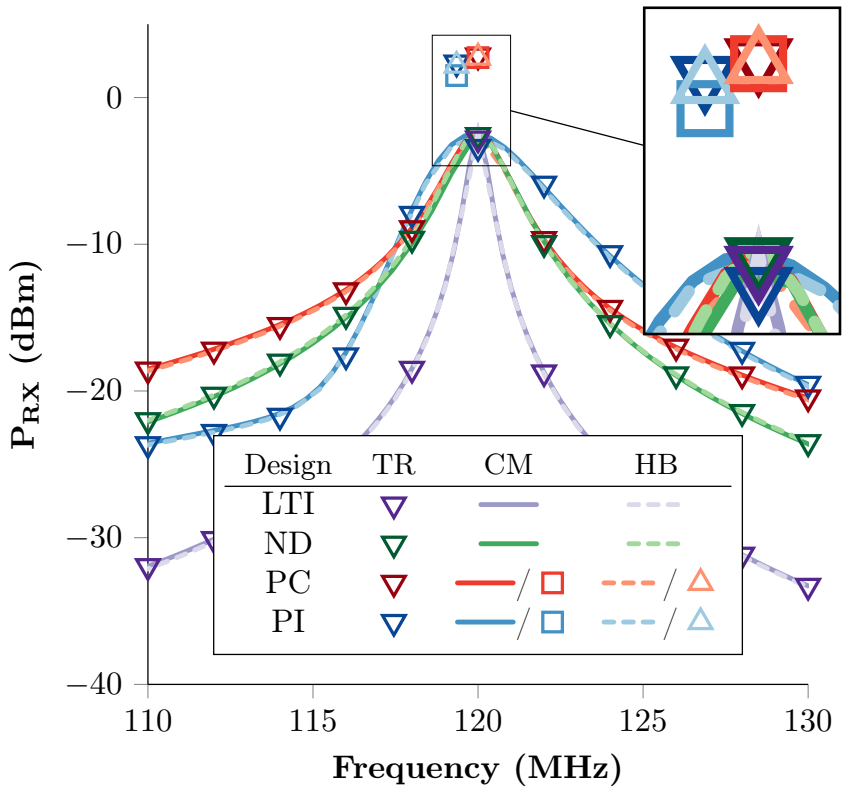


Figure 4.5: Received power across frequency of the LTI receiving antenna, and the antenna with the non-degenerate (ND) parametric tuning, the phase coherent (PC) degenerate tuning, and the phase incoherent (PI) degenerate tuning. Each design is simulated using CMMoM (solid line), HB (dashed line), and a transient (markers) solver. The discontinuous markers on the plot correspond to the degenerate points of the degenerate designs, and an additional marker is used for the HB and CMMoM simulations at these points since the power received is calculated using the idler and signal harmonics and not just the signal harmonic.

mirroring the instantaneous bandwidth improvements.

The EVM results coincide with example step responses shown in Figure 4.6b. In this plot, the received voltages from a single tone input at the center frequency of the signals are plotted normalized to the incoming voltage's magnitude. As expected, the rise time for the ND case is approximately three times shorter than that of the LTI case. The phase dependent magnitude of the PC antenna is illustrated for a few different phases, where each one has a varying magnitude. The PI case maintains the same magnitude, but the beat frequency caused by the idler frequency being so close to the carrier is evident and will create phase dependent distortion in each symbol.

The distortions in the received signals are further illustrated in the IQ diagrams in Figure 4.7. At the lower symbol rates the ND and LTI antennas appear very similar, however, the PC symbols appear "squished" along one dimension due to the phase dependent attenuation. The PI case has no human readable pattern due to the distortion caused by the beat frequency. The IQ diagrams for the ND and LTI antennas are also shown for 4.8 Ms/s, and highlight how the ND case more closely resembles the ideal signal before equalization than the LTI case. In this case, the increase in bandwidth of the ND antenna is less demanding of the equalizer than the LTI antenna, and so manages to receive a signal with less EVM.

4.5.1 Maximizing gain and bandwidth

This section derives optimized gain and bandwidth functions by maximizing equations (4.10) and (4.12), expressed in terms of the modulation factor γ and the loaded quality factor of the TVC at the signal frequency $Q_{\mathrm{s}}^{\mathrm{TVC}}$. This is performed by assuming the values of several parameters that maximize peak gain in equa-

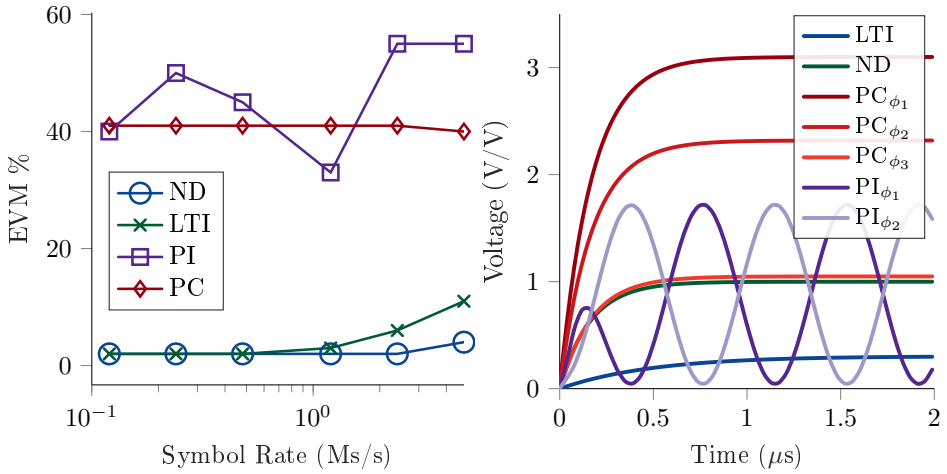


Figure 4.6: The EVM as a function of bitrate (left) and the step response (right) of the LTI antenna and the three parametrically tuned antennas. The ND receiver configuration outperforms all three, while the LTI outperforms the PC and PI configurations.

tion (4.10) and half power fractional bandwidth in equation (4.12). The assumed values can also be used as a guideline for optimizing the performance of a particular parametrically tuned ESA.

Deriving an equation for maximum peak gain starts by determining what parameters should be fixed and which should be variable. The maximum value of equation (4.10) is found by maximizing the negative resistance term in equation (4.9) for a fixed signal frequency and modulation factor and then maximizing the gain equation (4.10) for a fixed negative resistance. The negative resistance term is maximized by assuming the idler resistance is zero and the idler-to-signal frequency ratio $r_\omega = \omega_\mathrm{i}/\omega_\mathrm{s}$ is minimized. The idler-to-signal ratio should be as close to one as possible without causing the idler and signal frequencies to overlap. A signal-to-idler ratio of two is used in calculations here to simplify the equations. As a result, a half-power fractional bandwidth up to 100% will not overlap. In realistic situations the idler frequency antenna resistance will not be zero and the frequency ratio will

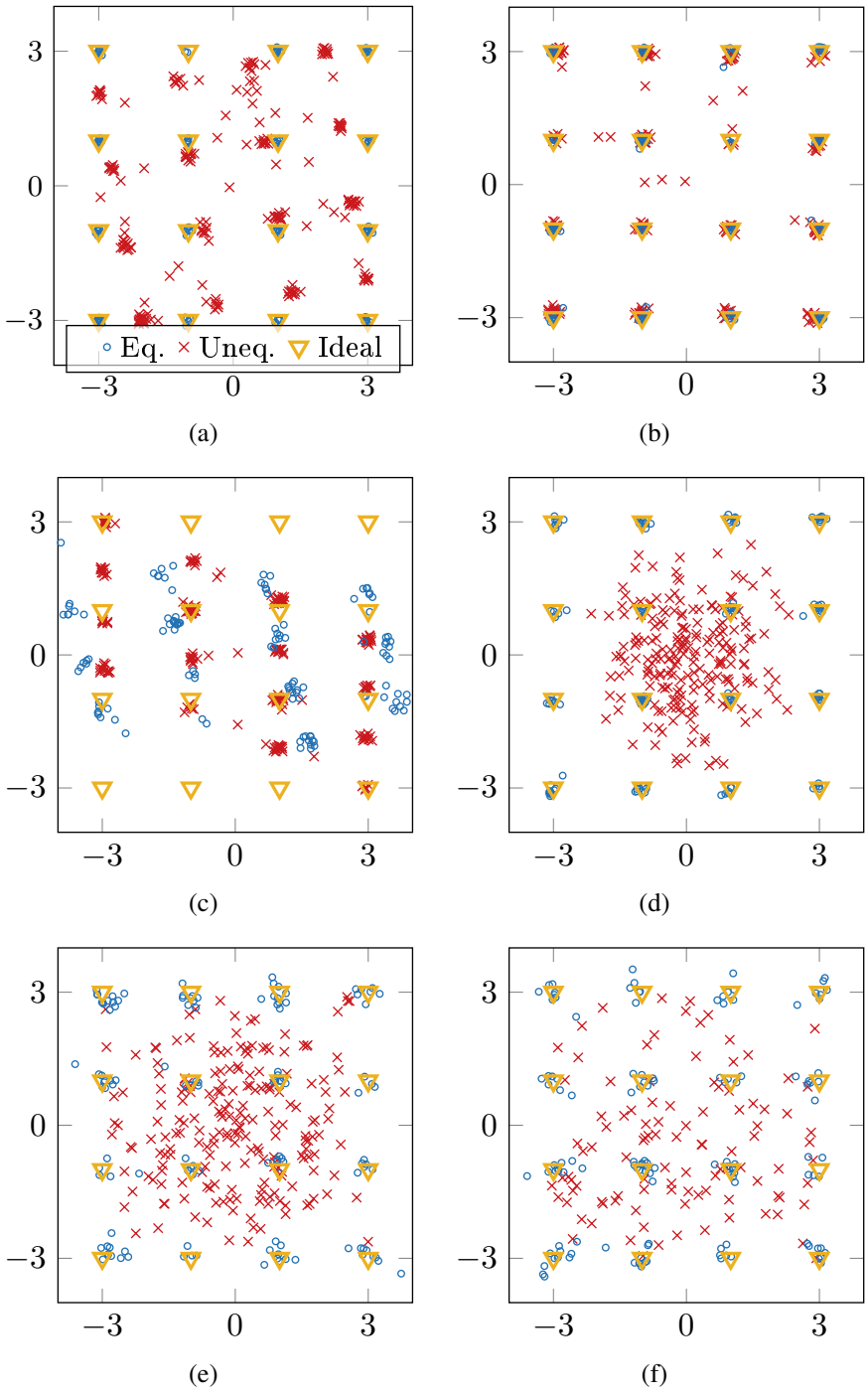


Figure 4.7: The IQ diagrams at a bitrate of 0.12 $\mathrm{Ms/s}$ are shown for the LTI (a), non-degenerate (b), phase coherent (c), and phase incoherent (d) cases. The IQ diagrams for a bitrate of 4.8 $\mathrm{Ms/s}$ is also shown for the LTI (e), and non-degenerate (f) cases.

not be exactly two, so as an antenna moves further away from this ideal the negative resistance will decrease.

If the normalized negative resistance R_{-}^{N} is held constant to ensure stability while allowing the load and antenna resistance at the signal frequency to vary, then setting the load resistance equal to the antenna resistance maximizes gain. Setting the parameters in equation (4.10) to coincide with these assumptions results in

$$G_{\mathrm{t}}^{\max} = \frac{1}{(1 - (\frac{\gamma}{2} Q_{\mathrm{s}}^{\mathrm{TVC}})^2)^2}. \tag{4.13}$$

To maximize bandwidth in relation to the transducer gain in equation (4.13), the total loaded quality factor of the circuit model

$$Q_{\mathrm{L}} = \frac{1}{\omega_{\mathrm{s/i}} R_{\mathrm{s/i}}^{\mathrm{net}} (C_1 || C_{\mathrm{s/i}})} \tag{4.14}$$

must be minimized. The minimum possible loaded quality factor achievable is equal to the loaded quality factor of the TVC, representing a case where the effective static capacitance of the TVC is the dominant capacitance in both the signal and idler resonator subcircuits of the parametrically tuned ESA. Thus,

$$\frac{1}{C_{\mathrm{s/i}}^{\mathrm{net}}} = \frac{1}{C_1} + \frac{1}{C_{\mathrm{s/i}}} \approx \frac{1}{C_1}. \tag{4.15}$$

As previously mentioned, this will often be the case for the signal band if the antenna is sufficiently detuned from the desired resonant frequency without the capacitor. This may not be the case for the idler band, however, and the assumption on quality factor would most likely be met by reducing the quality factor at the idler frequency relative to the TVC.

Using the values from the maximum gain expression in (4.13) and assuming

that the minimum loaded quality factor is achieved in equation (4.15), then equation (4.12) reduces to

$$\Delta_{\mathrm{G}}^{\max} = \frac{2 - \frac{1}{2}(\gamma Q_{\mathrm{s}}^{\mathrm{TVC}})}{Q_{\mathrm{s}}^{\mathrm{TVC}}\sqrt{-1/8(\gamma Q_{\mathrm{s}}^{\mathrm{TVC}})^4 + 2(\gamma Q_{\mathrm{s}}^{\mathrm{TVC}})^2 + 3}}. \tag{4.16}$$

4.5.2 Relation of bandwidth to peak gain

This section uses equations (4.13) and (4.16) to illustrate the limitations on the gain-bandwidth relationship of a parametrically tuned ESA. This analysis is accomplished by determining the maximum possible gain as a function of bandwidth. This section validates the maximum calculated gain for a fixed bandwidth by using a nonlinear optimizer and a CM simulation of the circuit model in Figure 4.1 with no linear approximations of the resonances. Afterwards, this section investigates the effects of loss at the idler frequency and modulation factor on the relationship between gain and bandwidth.

The gain-bandwidth relationship is validated using an interior algorithm for nonlinear optimization [49]. Optimization was performed on Equation (4.10) with the single objective

$$\begin{aligned} \underset{x}{\text{maximize}} \quad & G_{\mathrm{t}}(\boldsymbol{x}) \\ \text{subject to} \quad & \Delta(\boldsymbol{x}) = \Delta_{\mathrm{G}}, \end{aligned}$$

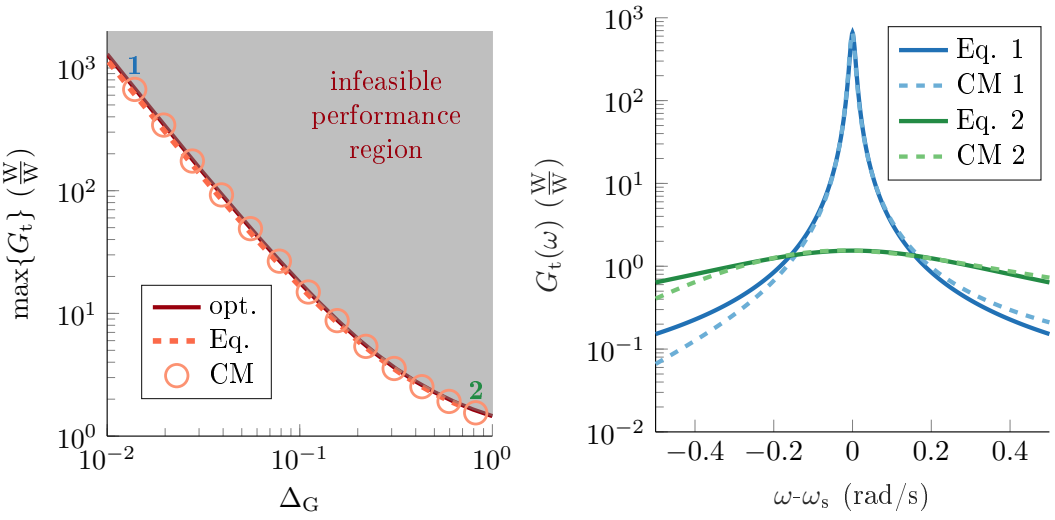
where Equation (4.12) is a nonlinear constraint equal to a desired bandwidth Δ_{G} and $\boldsymbol{x}$ is a vector containing γ, ω_{i}, C_0, R_{s}, R_{i}, and R_L. The modulation factor was restricted to be some number between 0 and 1, the idler was restricted to be a real number such that $\omega_{\mathrm{i}}/\omega_{\mathrm{s}} \geq 2$, and C_0, R_{s}, R_{i}, and R_L must be real, positive numbers.

The results of the derived equations (4.13) and (4.16) are compared to the optimzed values in Figure 4.8a for a modulation factor of one. Figure 4.8a show that

the curve defined by equations (4.13) and (4.16) is only slightly under the optimized gain curve with an average relative difference of 4.6%. The agreement between the equations using the assumptions about various circuit parameters and the optimizer shows that the assumptions can be used as targets in designing a parametrically tuned ESA to maximize the gain for a given bandwidth.

The optimizer was independently verified with a CM model of the circuit in Figure 4.1 that calculates the impedance across frequency using capacitances and inductances instead of the impedance function in equation (4.2). The maximum relative error between the conversion matrix model and the optimizer is 1%, demonstrating that the optimizer arrived at realizable values and that the narrowband impedance function was effective at modeling each resonance. Figure 4.8b compares the gain as a function of frequency of two of the points on either end of the trace in Figure 4.8a, calculated using a CM model of the circuit and using equation (4.8). The agreement of the three methods suggests that using the assumptions made in deriving Equations (4.13) and (4.16) as guidelines for designing a parametrically tuned, receiving ESA can result in performance near the upper limit.

The gain-bandwidth relationship in Figure 4.8a assumes no idler resistance ($R_{\mathrm{i}} = 0$) and that the modulation factor γ is one. The effects of idler resistance are shown in Figure 4.9 with multiple cases of the optimizer with a fixed signal resistance and variable idler resistance. Since the negative resistance is inversely proportionate to the resistance at the idler the overall maximum achievable gain for a fixed bandwidth decreases as the ratio of the idler-to-signal resistance increases. The same trend occurs with decreasing γ, as shown by Figure 4.10. As the modulation factor decreases from one, the maximum gain is decreased since negative resistance is proportional to the modulation factor.



(a) (b)

Figure 4.8: Maximum gain for a fixed bandwidth (left) is calculated using equations (4.13) and (4.16), the optimizer in (4.5.2), and a CM model using the component values determined by the optimizer. Gain as a function of frequency (right) of the two designs labeled 1 and 2, calculated using CM and equation (4.8).

4.6 Conclusion

This section has demonstrated that a TVC can be used with an ESA to improve its bandwidth. In the process, an analysis was undertaken to illustrate the absolute maximum gain achievable for a given bandwidth and from that design guidelines were developed. This analysis included an example of an electrically small concentric loop antenna improving its bandwidth by a factor of three using a TVC that can be realized with a COTS varactor. The next section looks into using a single-balanced topology, instead of a singularly polarized TVC, to understand possible benefits from using the alternative TVC configuration.

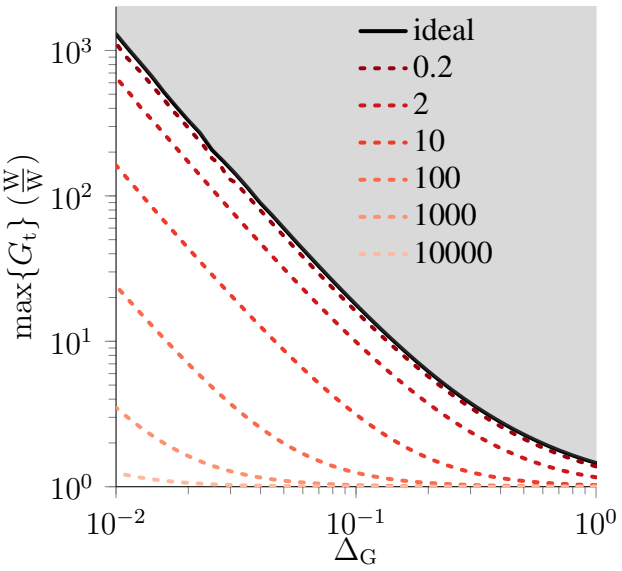


Figure 4.9: Effects of loss at the idler frequency on gain and bandwidth for increasing ratios of idler subcircuit loss over signal subcircuit loss.

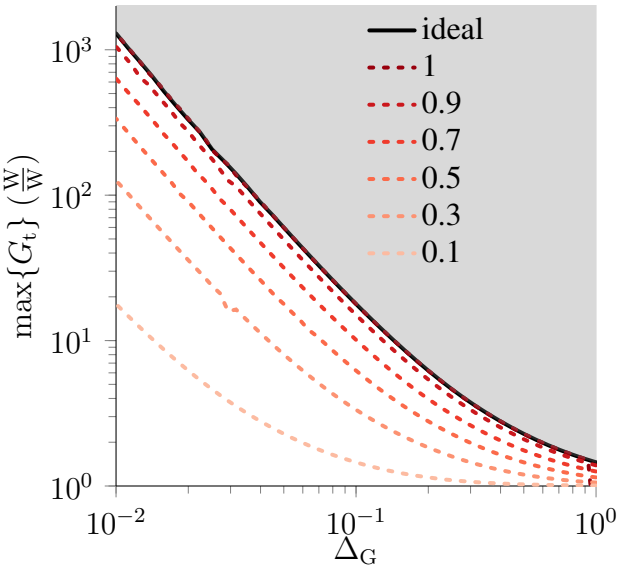


Figure 4.10: Effects of loss at the idler frequency on gain and bandwidth for increasing ratios of idler subcircuit loss over signal subcircuit loss.

Chapter 5

Single balanced parametrically amplified receivers

While the designs in Chapter 4 demonstrated that the parametric tuning could improve the antenna's bandwidth beyond its LTI counterpart, it was also shown in Chapters 3 and 4 that these designs do not approach the theoretical maximum gain-bandwidth limit. One solution is to incorporate a single balanced diode architecture instead of a single diode. Using the single balanced architecture alleviates a few problems: 1) it will decouple the idler current from the rest of the antenna, completely preventing re-radiation and interferers and external noise at the idler frequency being mixed into the signal, 2) the idler resonance is no longer dependent on the antenna, and 3) the loaded quality factor of the whole parametrically tuned antenna is only dependent on the TVC.

This section reviews literature on the single balanced parametric amplifier and then illustrates its performance with a circuit implementation similar to chapter 3. Next, a loop antenna is designed and loaded with a single balanced parametric tuning element. Finally, the instantaneous frequency domain performance is compared to the LTI and ND cases from chapter 4.

5.1 Single Balanced Parametric Amplifier Theory

This section covers some of the theory behind why the single-balanced topology is beneficial for negative resistance parametric amplification. The benefits are then demonstrated with a circuital example that is compared to the circuital parametric amplifier design #1 from chapter 3.

The first mention of balanced parametric amplifiers in literature was in the works of [50] and [51]. The single balanced parametric amplifier, illustrated in Figure 5.1, consists of a signal coupling network leading to two TVCs in anti-parallel. In Figure 5.1 the series RL's with the TVC represents a varactor and its series inductance and resistance. The anti-parallel arrangement causes the current i_{s} to see the two TVCs in parallel with the opposite polarity, while the current i_{d} sees the two TVCs in series with the same polarity.

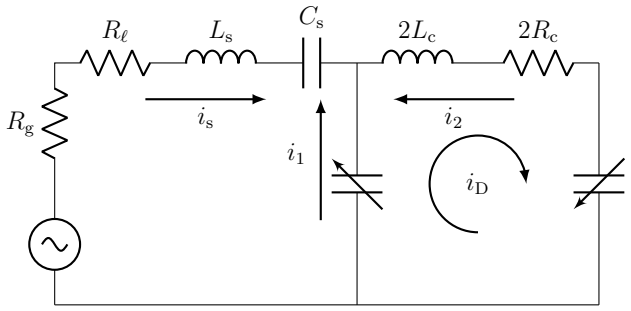


Figure 5.1: Circuit model of the single-balanced parametric amplifier.

Usually, an added idler coupling network would load the amplifier and increase the Q above the minimum set by the TVC. For the single balanced topology, however, the two diodes resonate together in series at the idler frequency, creating a short circuit without an external network. To minimize the Q factor of the idler circuit, the authors in [50] and [51] used the self-resonance of the diode as the idler frequency, so an additional inductor was not needed. The authors of [51] derived

equations for the gain-bandwidth product and noise figure for the anti-parallel diode pair and showed that the single-balanced topology circumvents idler tank Q factor limitation of the the singly-loaded design from Chapter 3 and achieves a higher gain-bandwidth product without increasing the noise.

An additional benefit of the single balanced topology is that it inherently cancels out the current at the idler frequency outside the diode ring. The current cancellation can be best understood through examining the power series representation of the currents [30]. Say the current flowing through the TVC is a function of the voltage across the diodes $f(V_\mathrm{d})$ with a power series of

$$f(V_\mathrm{d}) = aV_\mathrm{d} + bV_\mathrm{d}^2 + cV_\mathrm{d}^3 + dV_\mathrm{d}^4 + ... = i_1 \tag{5.1}$$

then when the current is defined flowing against the TVC and the voltage is flipped relative to its polarity the function is

$$-f(-V_\mathrm{d}) = aV_\mathrm{d} - bV_\mathrm{d}^2 + cV_\mathrm{d}^3 - dV_\mathrm{d}^4 + ... = i_2. \tag{5.2}$$

Using Kirchhoff's Current Law shows that the current looking into the TVCs is

$$i_s = i_1 + i_2 = f(V_\mathrm{d}) - f(-f(V_\mathrm{d})) = 2af(V_\mathrm{d}) + 2cf(V_\mathrm{d})^3 + ... \,. \tag{5.3}$$

Since the second order terms have been canceled by the difference in polarity of the two TVCs, none of the difference harmonic will appear at the output of the amplifier. Taking the current loop i_d into consideration

$$i_\mathrm{d} = i_1 = -i_2 = bV_\mathrm{d} + dV_\mathrm{d}^4 + ... \tag{5.4}$$

shows that the idler harmonic will exist within the TVCs and is function of the applied signal voltage. Therefore, the negative resistance can still be generated despite the cancellation of the idler current exterior to the TVCs. Therefore, these results show that only the odd order terms of the expansion (V, V^3, etc...) appear at the output current i_{s} and only the even order terms (V^2, V^4, etc...) appear at the current within the series TVCs i_{d}.

An example of a circuital single-balanced parametric amplifier in Figure 5.1 was simulated with the components in Table 5.1. Table 5.2, like in chapter 3, shows the gain and bandwidths of all the designs, including the simulated bandwidth, the bandwidth calculated using the Q of the resonators and equation (3.7), the maximum bandwidth if the Q of the circuit is only based on the TVC as in equation (3.11), and the theoretical maximum calculated from equation (3.10). The transducer gain of the single balanced design across frequency is compared to design #1 in Figure 5.2. Table 5.2 and Figure 5.2 show there is almost a tenfold improvement in bandwidth from the classic design #1 for the balanced design. More importantly, the balanced design managed to achieve 86% of the theoretical maximum while design #1 or #2 from Chapter 3 could only get at most 16%. This means the balanced design circumvented the limitation that both designs #1 and #2 were under using the same modulation factor and nearly the same static capacitance.

Table 5.1: Component values for the actively broadbanded and single-balanced parametric amplifiers.

$R_\ell(\Omega)$	L_1(nH)	C_1(pF)	L_2(nH)	C_2(pF)
5	404.64	440	7.705	4

Another benefit of the single-balanced architecture is the harmonic isolation, as demonstrated in Figure 5.3. While the odd-order harmonics are only slightly canceled in the current flowing between the TVCs i_{d}, there are hundreds of dB of

Table 5.2: Performance of the single balanced parametric amplifier against design #1.

Design	G_t (dB)	b% (sim.)	b% (calc.)	b% (max)	b% (theor.)
Balanced	20.35	0.340	-	-	.393
#1	20.10	0.048	0.046	0.064	.393

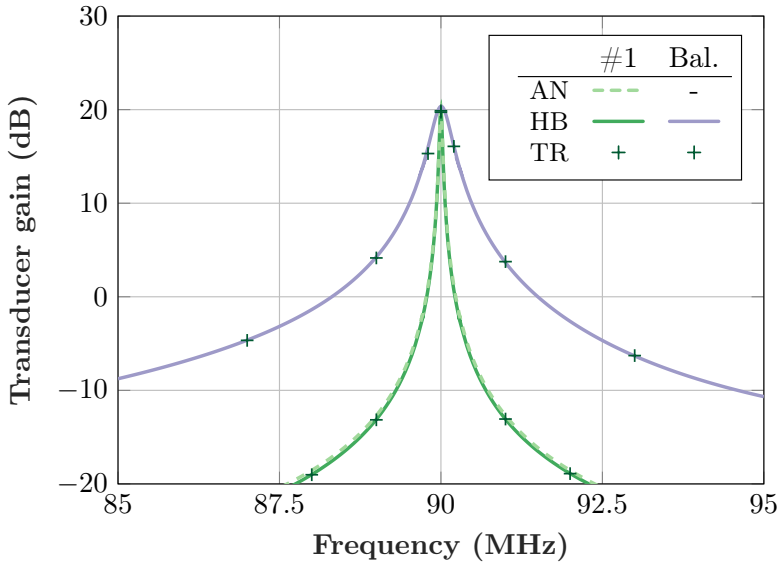


Figure 5.2: Gain across frequency of the single balanced parametric amplifier against design #1.

rejection of the even-order harmonics in the current flowing through the load at the signal frequency i_s.

5.2 Designing a Single-Balanced, Parametrically Tuned Receiver

Designing a parametrically tuned ESA using the single balanced topology is similar to that of the classic parametric tuning from Chapter 4 with some key differences. Designing the ESA is more straight-forward since the idler frequency current is restricted to the diode pair. The self resonant frequency of the varactor being modeled must be considered, since that frequency determines the idler fre-

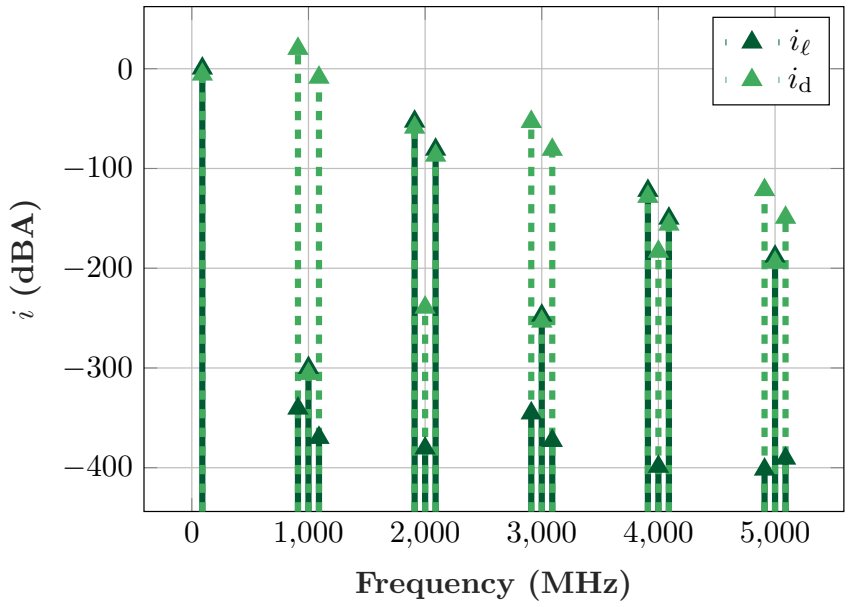


Figure 5.3: Currents at all simulated harmonics with $f_\mathrm{s} = 90$ MHz of the single-balanced parametric amplifier.

quency, and by extension the pump frequency. The idler frequency can be changed using inductive loading within the diode ring, but care should be taken as inductors have non-negligible loss compared to varactors' losses.

Since the idler frequency is not important in design of the ESA, a single square loop was used as the antenna, with dimensions shown in Figure 5.4. While these dimensions resulted in the ka being reduced from 0.37 down to 0.28, the choice of size allowed the single balanced design to be tuned to resonate with a similar static capacitance as the designs in chapter 4. The varactors being modeled were the SMV1233 with a series resistance of 1.2 Ω and inductance of 1.5 nH. An additional 25 nH inductor was placed in series with each varactor to drop the idler frequency down to 975 MHz, so that the maximum frequency required for simulations to converge could also be reduced to accelerate computation time. The single balanced design required a modulation factor of 0.075, less than half of the classic design from chapter 4, and was designed to operate with a 50 Ω load resistance.

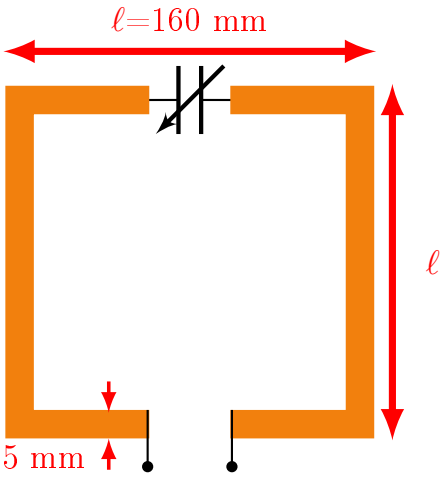


Figure 5.4: Dimensions of the loop used for the single balanced parametrically tuned receiver.

5.3 Results of the Single-Balanced Receiver

The instantaneous bandwidth of the single balanced, parametrically tuned antenna is shown in Figure 5.5. The single balanced version has a bandwidth approximately six times wider than that of the LTI square loop, making it twice as much of a bandwidth improvement as the ND design. There are additional benefits in comparing the ND and single balanced antennas, as the single balanced version: 1) achieves a broader bandwidth with a smaller antenna ka, 2) has a lower modulation factor than the ND case, 3) rejects the idler from the aperture of the antenna, and 4) operates with a 50 Ω load. Since modulation factor is directly proportionate to the pump power needed to operate the TVC, this means the single balanced case should consume less power for amplification. Additionally, this version does not need a matching network as it already matches to 50 Ω load. Lastly, the rejection of the idler on the aperture of the antenna not only prevents noise and interferers being mixed into the signal, but also prevents re-radiation at the idler frequency.

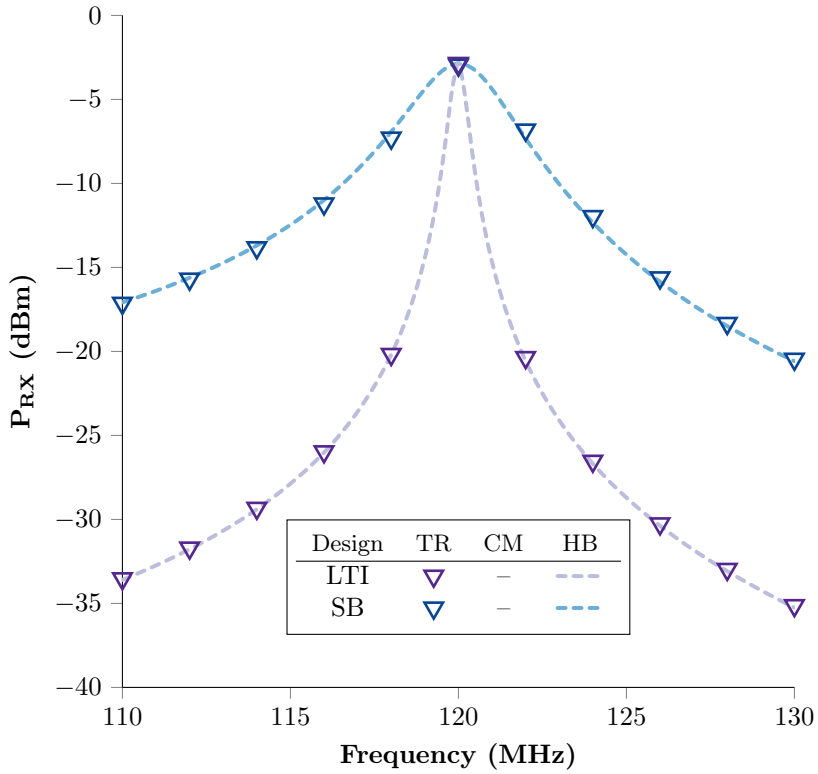


Figure 5.5: The power received across frequency of the single balanced, parametricaly tuned ESA (SB) and that ESA tuned with an LTI capacitor.

5.4 Conclusion

This chapter has demonstrated that using a single balanced configuration for parametric tuning results in several benefits, including isolation of the idler current from the antenna's aperture and a higher increase in bandwidth over the LTI case, despite the TVC having a smaller modulation factor and the antenna having a smaller electrical size. Therefore, a parametrically tuned ESA should employ a single balanced configuration wherever possible. The next chapter investigates another method of increasing the bandwidth of a parametrically tuned ESA, in which the antenna itself is modified instead of alterations being made to the TVC configuration directly.

Chapter 6

Parametrically amplified electrically small receive filtenna

6.1 Introduction

This chapter explores the impact of using a multi-resonant passband for the parametrically tuned ESA instead of a single resonance. The general concept is that since the TVC produces a negative resistance about the point of resonance in the signal frequency passband, introducing multiple resonances can increase the amplification bandwidth [40], [41], [42], [52], [53]. The first section of this chapter reviews how broadband coupling networks have been used in the past to broadband parametric amplifiers using filter theory. The section will cover some of the theory and demonstrate the possible improvements using a circuital example. To use the broadband coupling network approach for ESA design, an electrically small filtering antenna synthesis approach was used. Filtennas, or filtering antennas, are a type of multi-resonant antenna that can leverage filter synthesis to systematically produce a multi-resonant antenna. However, the process of using filter synthesis has not yet been extended to ESAs. Therefore, the second section demonstrates that filter synthesis is usable on ESAs, but that there are unique challenges in applying filter synthesis in the electrically small regime that do not present themselves at electrically larger sizes. The section will go over a symmetric, directly coupled

filtenna design process and validate the process with a fabricated filtenna. The next section shows that by decreasing the external quality factor of the first, non-radiating resonator the inter-resonator coupling can be increased and so too is the bandwidth. The last section loads the ESF with a TVC similar to chapter 4 to increase the bandwidth of the LTI ESF. The results of parametric loading are then discussed.

6.2 Parametric Amplifiers Using Broadband Couplers

Chapter 4 demonstrated the broadbanding abilities of single resonant parametric amplifiers, and much of the work on further increasing the bandwidth of parametric amplifiers focused on alternative coupling networks [40], [41], [42], [52], [53]. The focus was not only to decrease the Q of the coupling networks but to include the effective static capacitance of the TVC into the coupling network. Including the TVC into the coupling network allows the minimum attainable Q to be based on the coupling network and not the TVC by itself. This process centers on dividing the TVC into two parallel components: the static capacitance and the negative resistance. Figure 6.1 represents how these two components can be separated and how they can interact with a coupling network. With the components separated, the static capacitance could be used as the last component in the coupling network and the negative resistance can be treated as a termination in the coupling network design process. Many authors incorporate a circulator into their analysis as well, in addition to performance enhancements, the circulator facilitated the use of the reflection coefficient for analysis. With the reflection coefficient analysis and the two-component model of the TVC, authors were able to leverage coupling network analysis and design into their work and approach the theoretical bandwidth limit of

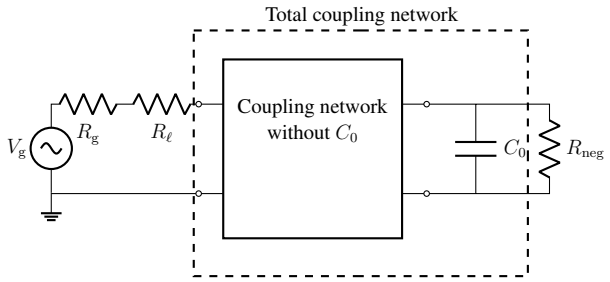


Figure 6.1: Generalized parametric amplifier diagram for broadbanding.

parametric amplifiers [40], [41], [42], [52], [53].

6.2.1 Two band couplers using filter theory

In Matthaei's work [40], they used [38] and [54] to determine the optimum reflection coefficients of a parametric amplifier for a given bandwidth. By first selecting a reflection coefficient for the parametric amplifier that corresponded with the desired gain of the amplifier, a standard, optimized Chebyshev filter design process would be used to find a coupling network that provided the most bandwidth possible for that gain at both the signal and idler bands. This work continued with papers like [55] where realistic diode models for the TVC were incorporated into the design procedure. The main difference was that the diode's parasitic capacitance and series inductance and resistance were included in the coupling design to optimize the amplifier performance. Then Kuh [41] made significant improvements to [40], stating that,

> ...the only available technique for designing wide-band parametric amplifiers and converters was contributed by Matthaei [40]. However, Matthaei did not give the limitation on gain and bandwidth [56, §3]. His design method was more complicated and involved a certain amount of cut and try process.

It is useful to note that while [40] did not create a gain-bandwidth relationship based on the coupling network limitations of [54], the thesis [56, §3] preceded the work done on the gain-bandwidth product in [41].

The authors of [41] used Butterworth theory from [57] and formulated a gain-bandwidth product and a procedure for deriving a coupling network with passbands of identical Q at both the signal and idler frequencies - a requirement for approaching the maximum possible bandwidth for a given gain. The gain-bandwidth product in [41] is

$$\Delta\mathrm{BW} \cdot \ln\left|\frac{1}{\Gamma}\right| \leq \frac{\pi\gamma}{4}\sqrt{\frac{\omega_\mathrm{i}}{\omega_\mathrm{r}}} \tag{6.1}$$

where the gain is captured in the return loss of the coupling network $\mathrm{RL} = \ln|1/\Gamma|$. The important takeaways from equation (6.1) are the modulation factor and difference between the idler and signal frequencies play important roles in increasing the gain-bandwidth product and maximizing these two increase the gain-bandwidth relationship. The bandwidth estimation calculated in [41] complements the analysis of equation (6.1) by showing the network's order effect on the amplifier. The fractional bandwidth estimation is

$$\Delta\mathrm{BW}_\mathrm{est} = \frac{u\gamma}{2}\sqrt{\frac{\omega_i}{\omega_r}} \tag{6.2}$$

where the bandwidth parameter u is

$$u = \frac{\sin\frac{\pi}{2n}}{a-b} \tag{6.3}$$

and a and b are expressions from [41] derived from the minimum value of the reflection coefficient and the order n of the network. The important property of the bandwidth parameter is that as the order n approaches infinity the bandwidth pa-

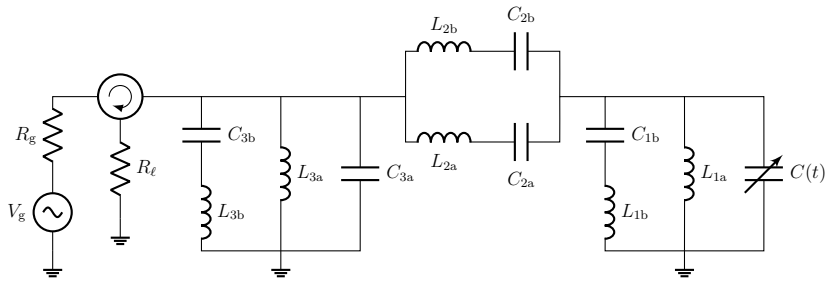


Figure 6.2: Schematic of the Butterworth coupling network-based parametric amplifier.

Table 6.1: Component values of the Butterworth coupling network-based parametric amplifier.

Res.	C_a(pF)	L_a(nH)	C_b(pF)	L_b(nH)	$R_\ell(\Omega)$	C_0(pF)
1	-	3.95	3.85	15.75	5087	4.0024
2	0.01	2.67e4	1.1e-4	2.67e4		
3	2.08	7.58	2.00	30.23		

rameter approaches

$$u \to \frac{\pi}{2\mathrm{RL}} \tag{6.4}$$

and the bandwidth estimation approaches the fundamental limit of equation (6.1). While the limitation on approaching the fundamental bandwidth limit was the Q of the individual resonators for the classic parametric amplifier in Chapter 4, it is the order number of the coupling network here. The broadbanding strategies in this section so far have been realized in literature, like in [58] who used the theories in [40], [41] to fabricate an X-band parametric amplifier with a measured gain of 19 dB of a 20% 3 dB fractional bandwidth.

6.2.2 Circuit Example

To better understand the multiple-resonant coupling network approach for broadbanding parametric amplifiers, the design process in [41] was used to create a 20 dB

amplifier using a 3^{rd} order coupling network as illustrated in Figure 6.2 with the component values in Table 6.1, with each resonator numbered 1 through 3. This example required a lossless TVC and a circulator, unlike the first example set. The design process in [41] would not work otherwise. Note that the last resonator, next to the TVC, is missing a capacitor that the other two resonators have - this is because the filter is designed using the TVC's capacitance instead of a separate capacitor. As mentioned earlier, this allows the Q factor to be based only on the total coupling network's Q factor.

The gain across bandwidth is shown in Figure 6.3. Figure 6.3 shows the calculated gain response

$$G_{\mathrm{t}} \approx \frac{1}{4|\Gamma|^2} \tag{6.5}$$

from [41] in addition to the simulations. The parametric amplifier using a filter-based coupling network is also compared to design #1 from chapter 3. The primary deviation in the analyticay calculation and simulations is the slight ripple in the passband despite the coupling network being maximally flat. The ripple is a consequence of the parametric amplification, and the ripple tolerance can be predicted using formulas in [41]. Table 6.2 shows the calculated bandwidth compared to the maximum theoretical bandwidth calculated using equation (6.1) and a bandwidth estimation using equation (6.2). Even though the design procedure was followed almost exactly, the simulated bandwidth is noticeably smaller than the estimation. This can be accounted for in the difference in the predicted ripple and the ripple in simulation; for a 3^{rd} order, 20 dB parametric amplifier designed this way, approximately 3.5 dB of ripple was expected according to [41] but the simulation had approximately 1 dB. Like with designing any equiripple network, the bandwidth and ripple have been reduced like an undercoupled resonator [45]. The reduction

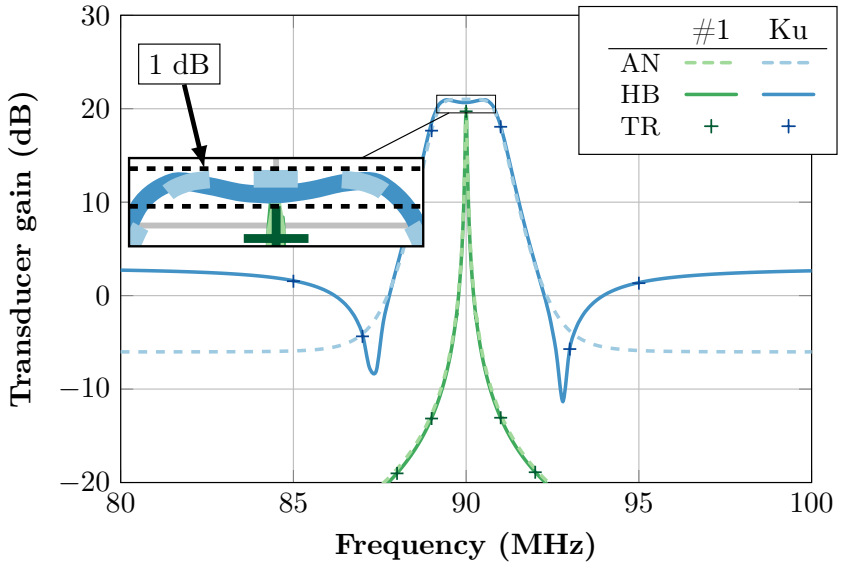


Figure 6.3: Frequency versus gain of the Butterworth coupling network-based parametric amplifier.

Table 6.2: Bandwidth and gain of Kuh's Butterworth coupling network-based parametric amplifier.

Design	Gain (dB)	b% (sim.)	b% (theor.)
Kuh	21	2.281	4.014
#1	20.10	0.048	0.393

from the maximum possible bandwidth and the simulation is due to the order of the filter, as described by the term u's behavior when the order number n approaches infinity. Despite not achieving the best possible bandwidth, the coupling network improved design #1's bandwidth by a factor of 47 using the same modulation factor and frequencies. This example suggests that an antenna should start off with as much bandwidth as possible to maximize the amplifier bandwidth.

6.3 Filtenna Design and Analysis

Now that the theory of filter-based parametric amplifiers has been discussed and the possible bandwidth improvements have been emphasized with an example, this

section will continue on to the parametrically tuned ESF. This section first covers the general design process of a symmetric, directly coupled filter. The synthesis procedure is used to create a second order, Chebyshev filtenna. The filtenna is then adjusted to be slightly asymmetric to further improve the bandwidth of the LTI design. The ESF is then parametrically tuned and its received power across frequnecy is compared to the ND design from chapter 4.

6.3.1 Overview of Symmetric Synthesis Method

The initial filtenna synthesis process utilizes a symmetric, directly-coupled, synchronously tuned topology where coupling between the port and the filtenna occur with only one resonator, inter-resonator coupling occurs in sequential order, and the radiating element is the last resonator illustrated by Figure (6.4a). The synthesis technique uses g-coefficients from the insertion loss method, determined by the desired bandwidth, passband type, and pertinent filter parameters [45], [59]. The coefficients are used with

$$\mathrm{Q}_{\mathrm{ext1}} = \frac{g_0 g_1}{\Delta}, \tag{6.6a}$$

$$\mathrm{Q}_{\mathrm{ext2}} = \frac{g_N g_{N+1}}{\Delta}, \tag{6.6b}$$

$$k_{n,n+1} = \frac{\Delta}{\sqrt{g_n g_{n+1}}} \tag{6.6c}$$

to calculate the first and second external quality factors for each port $\mathrm{Q}_{\mathrm{ext1}}$, $\mathrm{Q}_{\mathrm{ext2}}$ and the inter-resonator coupling coefficients $k_{n,n+1}$ [60].

The values in equation (6.6) act as targets for each step of the design process as outlined in the chart in Figure 6.5. First, the antenna element's lossless radiation quality factor is tuned in simulation to equation (6.6b) using expression in [8], [61], [62]. The target quality factor may unreachable based on fundamental limits [2],

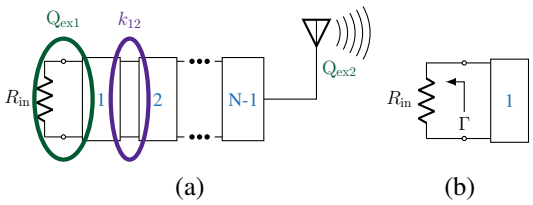


Figure 6.4

[63] or other factors, so a reselection of filter parameters may be necessary.

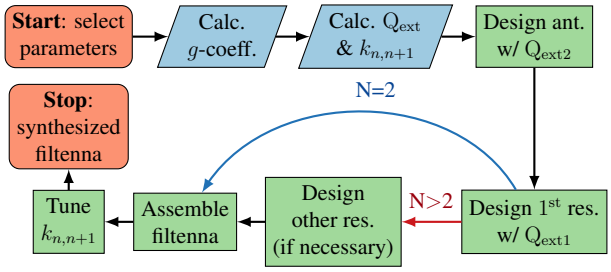


Figure 6.5: The flowchart for developing a second order filtenna.

The next step is to tune the external quality factor of the first resonator using equation (6.6a) as the target. The resonator's radiation should also be sufficiently smaller than the radiating element to preserve the direct-coupled behavior. The external quality factor of the resonator can be calculated from the phase of the reflection coefficient [59] with the lossless resonator loaded with the line impedance using

$$Q_{ex1} = \frac{\omega_0}{\Delta\omega_{\pm 90^o}}, \tag{6.7}$$

shown in Figure (6.4b). If the filtenna's order is 3 or greater this first resonator can be used as the intermediate resonators as well.

The inter-resonator couplings are tuned last by simulating the full filtenna. The target for the resonators' couplings are the inter-resonator coupling coefficients, defined as the sum of the ratios of the electoral energy transfer over electrical energy storage and the magnetic energy transfer over magnetic energy storage [59]. The

time-domain impulse response (TDR) method was used to tune the inter-resonator couplings, since it not only tunes the inter-resonator coupling but also allows for fine tuning of the other filtenna elements as each component of the response is identifiable in the time domain [64]. This process is done in sequential order, tuning the external quality factor and the resonance of the first resonator if needed, then the first inter-resonator coupling, the resonance of the next resonator, the next inter-resonator coupling, and so on ending at adjusting the resonance of the radiating element.

6.3.2 Calculating design targets

The filtenna geometry was chosen to be planar with a $ka < 0.5$, and the inter-resonator coupling was adjusted using the spacing between them. The chosen filter response was a second-order, equal-ripple with at most -10 dB equal-ripple about 120 MHz with 1.7% fractional bandwidth. The g-coefficients were calculated using [45, §8.3], shown in Table 6.3 with their corresponding design targetsas. The -10 dB 3 MHz bandwidth was selected as it resulted in a second external quality factor achievable by a planar antenna with room for the other resonator [8].

Table 6.3: The g-coefficients and filtenna design targets for a second-order, equal ripple response with 3 MHz of -10 dB equal-ripple

g's	g_0	g_1	g_2	g_3
	1	1.3601	0.7066	1.9250
Q & k	$\mathrm{Q}_{\mathrm{etx1}}$	$k_{1,2}$	$\mathrm{Q}_{\mathrm{etx1}}$	
	80	0.0173	80	

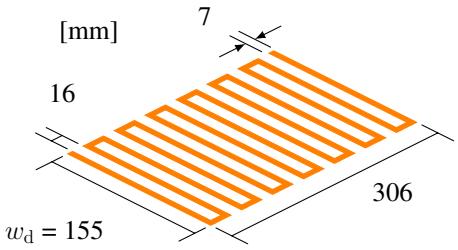


Figure 6.6: Geometry of antenna after design stage in subsection 6.3.3

6.3.3 Radiator design and tuning

A planar meandered dipole was used as the radiating element since it is self-resonant and achieves a relatively low quality factor while maintaining a radiation efficiency above 50% [8], [65]. The radiation quality factor of a meandered dipole is largely a function of ka and the aspect ratio, and $0.3 \leq ka \leq 0.4$ with an aspect ratio of 2 can result in the necessary radiation quality factor of 136 [8]. This choice in ka will also allow room for the other resonator while maintaining a $ka \leq 0.5$. The antenna and other simulations were performed in Ansys' HFSS, in this step as a 2-dimensional sheet of PEC. Following [65] the meandered dipole achieved a radiation quality factor of 79, resonated at 330 MHz, and had a radiation efficiency of 84%. The final meander had a ka of 0.431, with the dimensions and response shown in Figure 6.6.

6.3.4 Non-radiating resonator design and tuning

The first resonator was a capacitively loaded loop (CLL) fed with a Γ-match [66], as illustrated in Figure 6.7a and 6.7b. The CLL itself was designed to be narrow and rectangular so it would not increase the radius of the circumscribing ka sphere of the dipole, and the loop was tuned to resonate using a capacitive gap that can be loaded with an additional capacitor if necessary [67], [59, §13.2]. Instead of using

the Γ-match to transform the antenna's impedance exactly to the line impedance of 50 Ω, the Γ-match was used to intentionally mismatch the two to achieve a particular external quality factor. Figure 6.8 shows the CLL's external quality factor as a function of the Γ-match's arm length ℓ_Γ, demonstrating how the Γ-match can tune the external quality factor of the CLL. The CLL alone had a radiation efficiency of only 0.9% and so did not couple substantially into free space. Its efficiency was calculated using a simulation with finite conductivity. The CLL was tuned to 120 MHz by adjusting its length and the capacitance C_{res}. Next, the Γ-match's arm length was used to tune Q_{ext1} to 80, and the capacitor C_{match} was used to cancel out the inductance of the Γ-match.

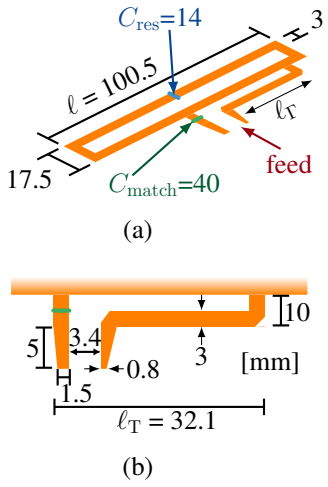


Figure 6.7: Geometry of first resonator after design stage in subsection 6.3.4.

6.3.5 Inter-resonator tuning

The full filtenna was simulated as a 2D copper sheet, as shown in Figure 6.9a. With the filtenna assembled, the TDR tuning could be performed and took four steps as shown in Figure 6.9b. A lossless circuit model was simulated in SPICE as the ideal comparison for tuning. The tuning process was as follows: the first

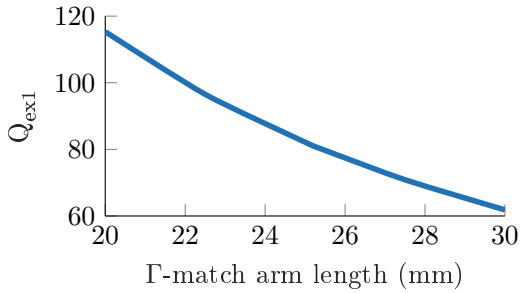


Figure 6.8: The first external quality factor, associated with the CLL, as a function of Γ-match arm length ℓ_Γ.

external quality factor was lowered using the Γ match, then the first resonator's resonant frequency was increased by shortening it, the inter-resonator coupling was too strong and was lowered by spacing the elements more, and finally the resonant frequency of the dipole was too high and was lowered using the aspect ratio.

6.4 Experimental validation and results

The filtenna was realized using Rogers RO5880LZ substrate with 20 mil thickness and half ounce μm copper cladding [68] to facilitate fabrication. Trimmer capacitors (Knowles JR300) were used to compensate for fabrication errors, with one used as the capacitor C_{res} and another used in parallel with a 15 pF (Murata GRM1885C1H) capacitor on the Γ-match. The filtenna in Section 6.3 was designed without a substrate to expedite the process, and including it in the realized design slightly changed the resonant frequency of the filtenna. After retuning the filtenna to include a substrate the final dimensions were the same as the design without the substrate except for the dipole width w_{D}, which changed to 154.2 mm, and the Γ-match and feed ℓ_{T}, whose new length was 36.6 mm.

Reflection coefficient and calibrated realized gain data measured in an anechoic chamber are compared against simulations of the same model and the conjugate-

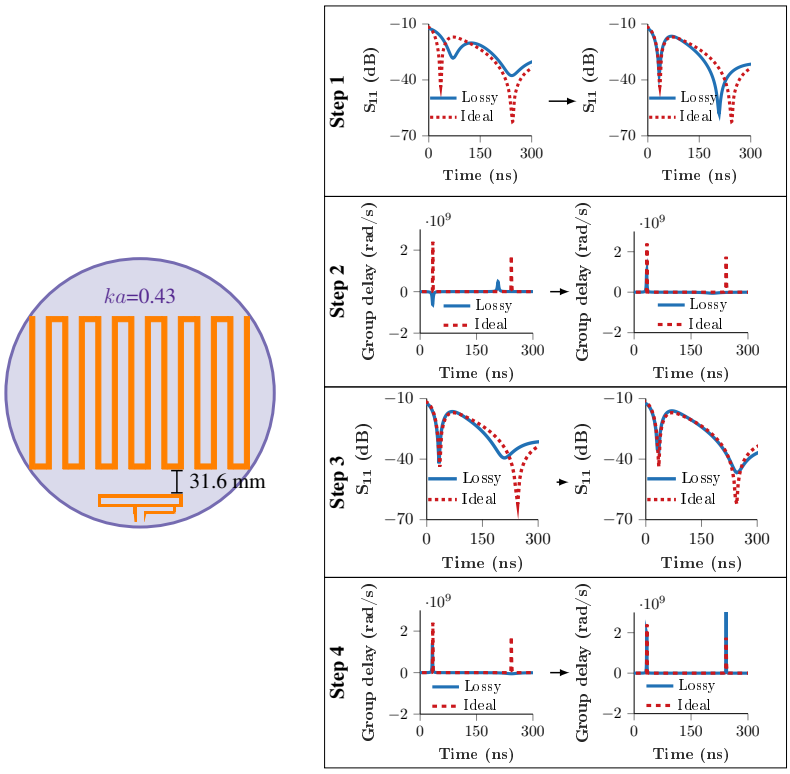
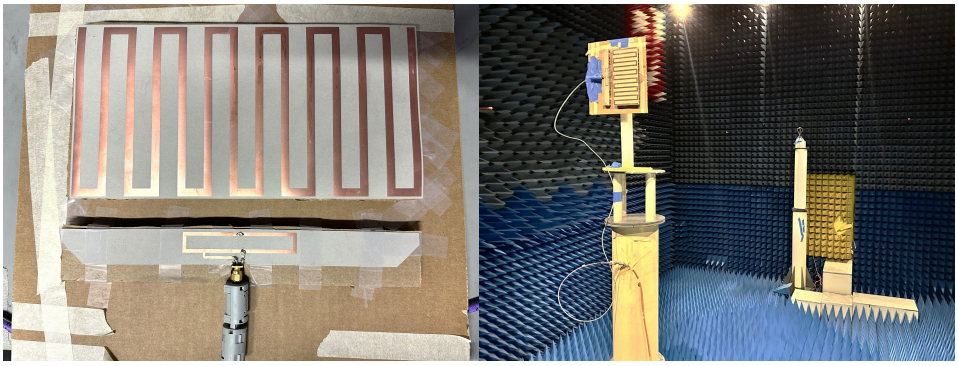


Figure 6.9: Figure a) shows the four steps in the TDR tuning stage: step 1) first external quality factor, step 2) first resonator's resonance, step 3) inter-resonator coupling, step 4) antenna's resonance. Figure b) shows the full filtenna with the element spacing and total ka.

matched dipole from Section 6.3.3 as a function of frequency normalized to their respective resonant frequencies f_r in Figure 6.11a. Simulated and measured E-plane and H-plane realized gain patterns at the center frequency are plotted in Figure 6.11b. The measured results achieve the initial bandwidth goals but the center frequency was shifted down by 2.4 MHz compared to the simulation, resulting in a 2% error. This shift in resonant frequency resulted from differences in the substrate footprint between the simulated and fabricated filtenna, and the filtenna conductor was simulated as a two-dimensional sheet.

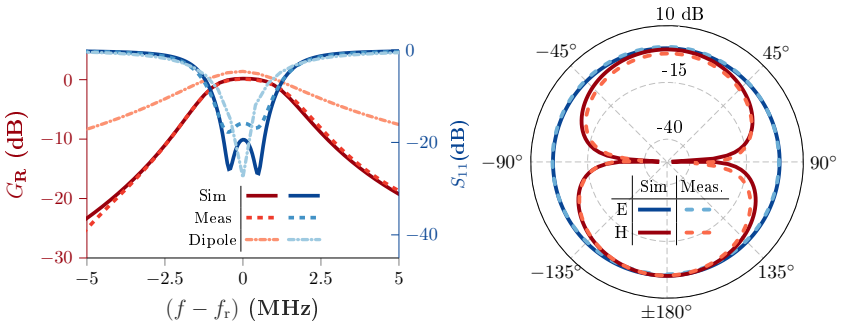
Comparing the reflection coefficients of the filtenna to the conjugate-matched

dipole from Section 6.3.3 shows that the filtenna successfully produced the desired response and increased the -10 dB realized gain bandwidth by 70%. However, the -3 dB realized gain bandwidth decreased to 2.2%, compared to the conjugate-matched dipole's 3%. The peak realized gain also decreased from the dipole's 1.4 dB down to the ESF's 0.2 dB. While the increase in -10 dB bandwidth of S_{11} came at the expense of a reduction in realized gain magnitude and bandwidth, these results demonstrate that this synthesis technique can be used in place of large, multi-variable parametric sweeps to design ESFs.



(a) (b)

Figure 6.10: Fabricated antenna (left) and measurement setup (right) used for the measured results.



(a) (b)

Figure 6.11: S_{11} normalized to the resonant frequencies f_0 (a) and radiation patterns at the resonant frequencies (b) of the simulated and measured results of the filtenna.

6.4.1 Asymmetric Variation

The reduction in the realized gain bandwidth can be compensated by increasing the coupling between the resonators. This is because the more tightly coupled the resonators are, the more bandwidth the filtenna will have [45], [59] As the coupling increases the filtenna will no longer be matched to 50 Ω, to alleviate that the first external quality factor is reduced to 60. The asymmetric filtenna was also loaded with a capacitor opposite the side closest to the CLL as shown in Figure 6.12, which does slightly reduce the efficiency of the dipole. However, this capacitor is necessary as it will be the location of the TVC in the following section. Additionally, the ka of the total filtenna decreased, which will impact the total performance. The full filtenna with dimensions is also shown in Figure 6.12.

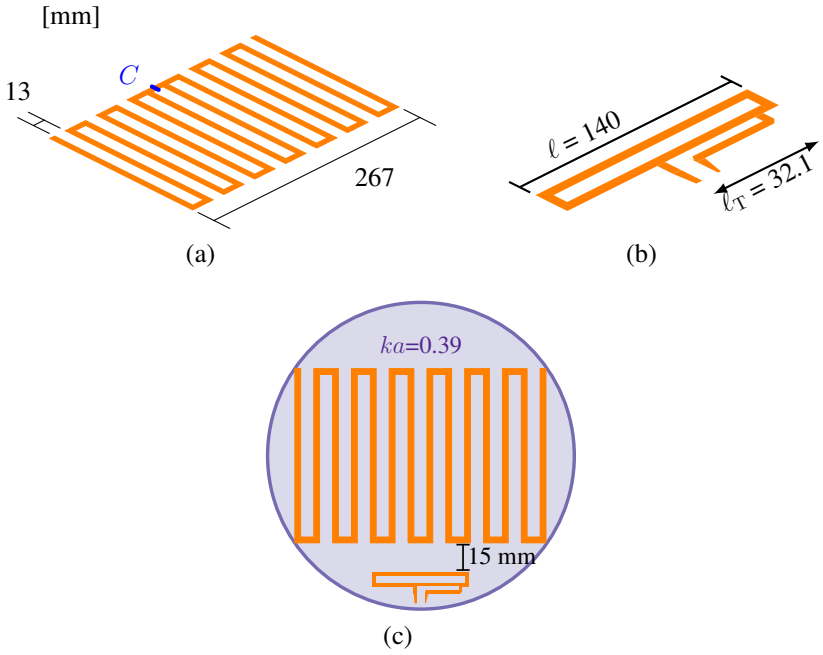


Figure 6.12: The layout of the asymmetric filtenna with updated dimensions is shown here. Any unlabeled dimensions are unchanged from the symmetric design.

Taking the process from section 6.3.5 results in the asymmetric filtenna shown in Figure 6.13. Compared to the symmetric design, it seems this design losses a

negligible amount of peak realized gain to sightly increase the bandwidth of the realized gain. Compared to the -3 dB of the symmetric filtenna of 2.2% bandwidth, the asymmetric is able to almost achieve the same bandwidth of the dipole at 2.9%. However, with a peak realized gain of 0.1 dB the asymmetric filtenna still loses slightly over 1 dB of gain compared to the meandered dipole.

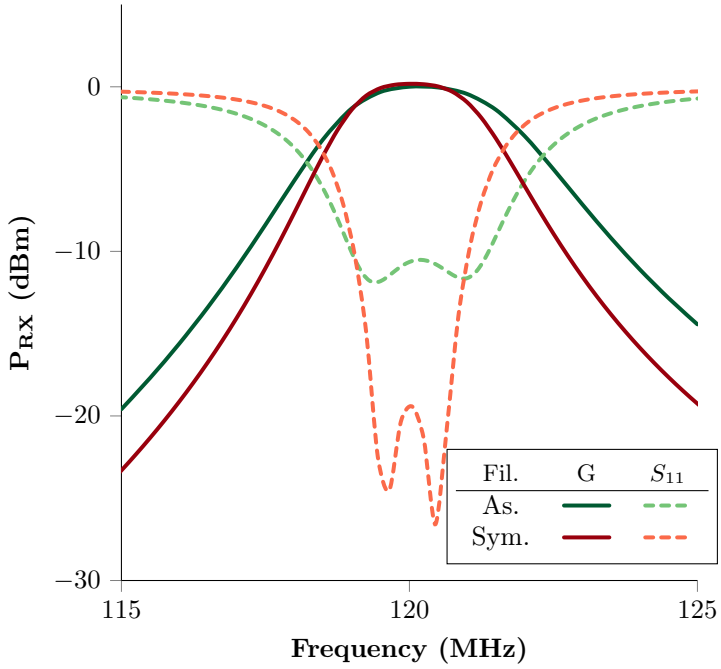


Figure 6.13: Comparison of the realized gain and scattering parameters for the asymmetric (As.) and symmetric (Sym.) designs.

6.5 Parametrically Tuned Electrically Small Filtenna

The asymmetric filtenna was loaded using the same proceduce discussed in Chapter 4. The design process resulted in the filtenna having a load resistance of 106 Ω, a pumping frequency of 1128 MHz, a modulation factor of 0.1, and a static capacitance of 4.6 pF. The filtenna was simulated in SPICE assuming a constant voltage across the bandwidth, and while this assumption is not as accurate as with

the singly-resonant designs, it is suitable for a proof-of-concept simulation. Discrepancies in bandwidths in this section compared to the previous section are due to the constant voltage assumption.

The power received as a function of frequency for the parametrically tuned filtenna, LTI filtenna, and ND case from chapter 4 are shown in Figure 6.14. Since the peak power for the filtenna and concentric loop designs were both matched to their LTI counterparts, the difference in peak power will be neglected from discussion. The -3 dB fractional bandwidth of the parametrically tuned filtenna is 2.2%, which is larger than the LTI bandwidth of 1.8% and the ND bandwidth of 1.5%. While the bandwidht of the parametrically tuned filtenna is greater than the ND design, the nLTI filtenna is only broader by a factor of 1.2 compared to the LTI version, where the ND case's bandwidth was 3 times broader than its LTI version. This is in part due to the decrease in modulation factor from 0.2 down to 0.16, however, this choice was made to maintain stability with the nLTI filtenna.

Another consideration is that the results if the circuital analysis in Figure 6.3 suggests that the bandwidth improvement of a second order coupling network compared to a singly resonant parametric amplifier should be much greater than the improvements in Figure 6.14. The circuital examples focused on generating 20 dB of peak gain instead of purely maximizing the bandwidth like with the parametrically tuned antennas, therefore, the using a multi-resonant antenna may be better suited to parametrically tuned ESAs where a considerable amount of gain is desired instead of trying to maximize the bandwidth while maintaining a gain of 0 dB like this work.

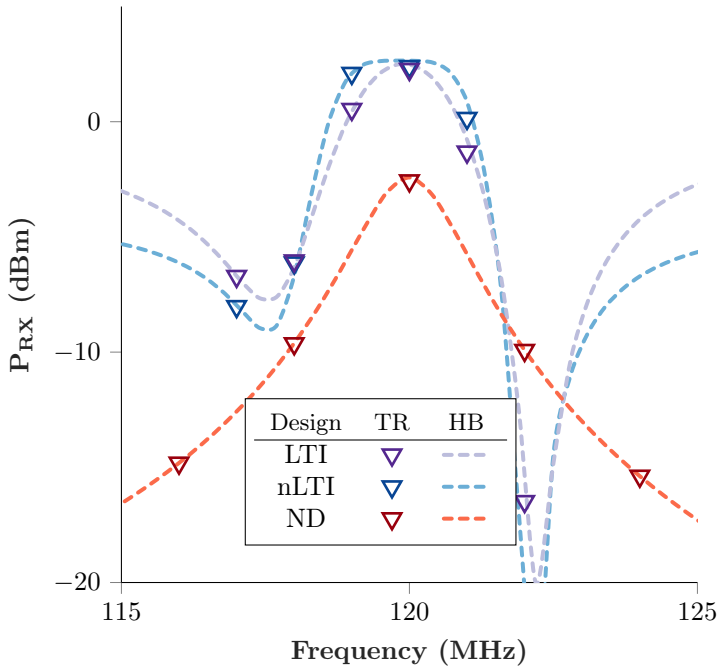


Figure 6.14: The power across frequency for the LTI and nLTI filtenna compared to the ND design from chapter 4.

6.6 Conclusion

This section demonstrated that a filtenna can be used in tandem with parametric tuning, and the result will improve the bandwidth of the ESF. However, there are some noticeable hurdles, primarily that a more rigorous design procedure for synthesizing a parametrically tuned ESF needs to be developed like has been done for circuital implementations of parametric amplifiers [40], [41]. It also appears that the multi-resonant, parametrically tuned ESA achieves more significant improvements over the singly resonant, parametrically tuned ESA when an increased peak received power over the LTI power received is desired.

The following chapter will take a detour into developing a novel method of determining the stability of a distributed structure loaded with a TVC. This is an important endeavour since the stability criteria from chapter 4 make assumptions

on the device. The method developed in the next chapter makes no assumptions about the antenna or the mode of operation for the TVC, making it particularly useful for testing stability for new methods of incorporating a TVC with an ESA beyond standard parametric amplification.

Chapter 7

Stability Analysis

7.1 Introduction

Stability is a crucial phenomenon to characterize when designing any active device, and without a robust analysis the device can fail. Stability analysis has been well established for standard amplifiers in the RF regime since the mid-twentieth century, and numerous ways to efficiently handle such an analysis have been developed in that time [45], [69], [70], [71]. It is common to assume that there are only poles in the left half of the complex frequency plane in the analysis of 2-port amplifiers operated in a linear region [45], [71]. Moreover, some stability analyses have been shown to fail for more exotic amplifying and non-LTI devices such as negative impedance circuits [72]. Such devices are particularly prone to instabilities in ways that solid-state amplifiers are not, and are stable under a narrow range of operating conditions. With the recent surge in the use of parametric amplification with nonlinear capacitors in antenna design, robust stability criteria are pivotal in transitioning this new category of antenna designs to practical application.

The concern with the stability of circuits utilizing nonlinear capacitor stems from issues that arise with non-Foster networks. Non-Foster networks generally utilize transistors to create negative impedances. At the harmonics generated by

nonlinear capacitors the capacitance can similarly appear negative. Non-Foster devices have been shown to fool standard stability tests and loop-gain tests by hiding s-domain poles, where $s = \alpha + \mathrm{j}\omega$ [72]. Thus parametric amplifiers must be dealt with carefully as they also exhibit non-Foster behavior and could pass stability tests in error. Another significant concern is the exclusion of one of two criteria used in stability analysis, known as Rollet's Proviso, which is often guaranteed to be true for simple, two-port amplifiers [45], [70], [71]. However, due to the prevalence of this automatic assumption Rollet's Proviso is not always included in stability analysis. Since standard parametric amplifier design usually does not analyze the s-domain response, Rollet's Proviso is neglected here as well [36], [37]. As antenna research continues to incorporate non-LTI devices the absence of stability analysis of non-LTI, distributed structures must be addressed while not masking any poles or excluding Rollet's Proviso.

Currently, stability analysis is often conducted through broad and computationally inefficient methods like load-pull analysis for LTI systems or parameter sweeps for non-LTI systems [73], [74]. There is also no general, standardized stability analysis method for antennas loaded on-aperture with non-LTI devices, like the antenna in [22]. Efficient analysis of an antenna with on-aperture loading of a non-LTI component requires a novel procedure that carefully follows the requirements for system stability for distributed systems.

The formulation of the stability analysis shown in this chapter begins with a review of device stability section 7.2. Next, a procedure for analyzing antennas in the s-domain using MoM is shown in Section 7.3, and then weakly nonlinear devices using CM is demonstrated in Section 7.4. In Section 7.5, the complex-frequency response of an on-aperture loaded antenna is modeled by loading its s-domain MoM representation with a complex frequency CM representing its weakly

nonlinear loads.

7.2 Review of Stability Analysis

An outline of negative resistance parametric amplifiers has been presented, so a review of stability analysis can be undertaken. The notion of stability had been around well before Rollet's work in [69], it standardized stability analysis for electrical networks. In his paper, Rollet laid out two criteria that must be met for a two-port electrical system to be stable, and while these criteria have been verified using different methods and have been extended to N-port networks the underlying requirements remain unchanged [70], [71], [75]. Rollet's analysis and subsequent permutations compose standard RF stability analysis. Firstly, Rollet's Proviso must be ensured, which states that a network's poles must lie only in the left half of the complex frequency plane under ideal terminations. This would translate practically to the impedance having no poles in the right half plane when ports are terminated in open circuits, or that the admittance meets the same criteria with the ports terminated in short circuits. In a multi-port system, this can be extended to saying that the determinant of the matrix of network parameters is non-zero [75]. Once Rollet's Proviso has been verified the second stability requirement can be analyzed, which requires that the real part of the impedance or admittance at a port be non-negative when the other is terminated with a perfect match. This second condition was referred to as the invariant stability factor (ISF) by Rollet and is of the form

$$k = \frac{2Re(\rho_{11})Re(\rho_{22}) - Re(\rho_{12}\rho_{21})}{|\rho_{12}\rho_{21}|}, \tag{7.1}$$

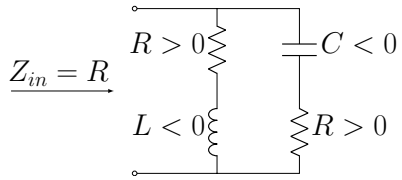


Figure 7.1: Example non-Foster circuit from [72] where the input impedance will allow the circuit to pass the second stability criterion while failing Rollet's Proviso.

where ρ_{xy} refers to the network parameter being analyzed, e.g. impedance or admittance parameters. Rollet stated that for unconditional stability k must be greater than or equal to 1 and that ρ_{11} and ρ_{22} must be greater than or equal to 0. The ISF has undergone different permutations, such as the $K - \Delta_s$ test or the μ test, but all verify the same constraint [71].

The issue of neglecting Rollet's Proviso, while not immediately problematic, extends to some standard parametric amplifier designs like the stability analysis outlined in [36] and [37]. When operated in a standard, negative resistance configuration, the stability of the device is verified through the analysis of the resistance at the terminal. If the resistance at the port is permitted to become less than zero, the device becomes unstable and begins to oscillate. Standard parametric amplifier topology makes analyzing the resistance at the feed a sufficient stability criterion as Rollet's Proviso is correctly presumed and ISF has been verified, but this may not hold for alternative circuits or an antenna loaded on-aperture.

The second common error in stability analysis occurs when a pole is invisible to the port, which [72] demonstrated with a simple, unconditionally unstable non-Fosters circuit that could pass both Rollet's Proviso, ISF, and a loop gain stability test. The circuit is shown in Figure 7.1, and the components are set by the relationship $L = R^2C$ where R is arbitrary. When the components are set in this way, the input impedance of the circuit appears to be a constant resistance across all

complex frequencies. The instability can be detected by not compressing the non-Fosters component into the network and examining the voltage or current along the non-Foster devices.

The non-Foster behavior of a nonlinear capacitor is best illustrated by examining the lower harmonic of an ideal, time-varying capacitor of the form,

$$C(t) = C_0 \cdot (1 + \gamma \cdot \sin(2\pi f_{\mathrm{p}})), \tag{7.2}$$

where C_0 is the mean capacitance, γ is the modulation factor of the time-variance, and f_{p} is the pumping frequency at which the capacitor oscillates. The apparent capacitance moved from the excitation frequency to the lower harmonic is $\frac{-\mathrm{j}\gamma C_0}{2}$, where the negative sign shows that the apparent capacitance at the lower harmonic is non-Foster. This means that, under certain circumstances, a nonlinear capacitor that has been pumped to become time-varying could hide poles relative to a port.

Some efforts have been made to analyze the stability of parametric amplifiers, both independent of the antenna and in a co-designed system [20], [74]. In [20] stability is analyzed by deriving an expression for the input impedance of the amplifier while connected to the antenna for the one-dimensional frequency domain and then extended to complex frequencies using analytic continuation. This approach only examines port impedance which was identified as a potential issue in [72]. The authors of [20] rely on the classic assumption that the negative resistance is the only source of instability and use their expression for input impedance in a constrained window of frequencies to validate their stability analysis. While this model works well for their particular application, it was explicitly derived for the case in [20] and is not applicable to other co-designed antenna-parametric amplifier systems.

The stability analysis in [74] used a closed loop transfer function to determine

the locations of the poles and zeros. By determining the transfer function from inside the circuit, the problem of pole cloaking identified in [72] is avoided. Since this method requires a harmonic balance simulation, any permutations of the circuit require an entirely new simulation. The methods in [74] and [20] directly inspect the complex frequency domain for their specific design and have no clear way to be generalized for distributed electromagnetic structures.

The method formulated in this paper avoids masking poles by compressing only the LTI portion of the model (the s-domain MoM impedance matrix) into an N-port network while leaving all nonlinear components exposed. The method can incorporate an arbitrary passive, distributed electromagnetic structure using a modified MoM matrix, and is computationally efficient as the matrix can be compressed and reused for multiple permutations of loads and nonlinear capacitors [28]. It has been demonstrated that the nonlinear capacitor can be reasonably assumed to be weakly nonlinear, or time-varying, so a simple harmonic decomposition in the complex frequency domain is sufficient to model the element [30].

7.3 Complex Frequency Method of Moments

To capture the complex frequency behavior of an antenna, an s-domain full-wave solver is developed in this section. MoM is a widely used analysis method for distributed electromagnetic structures like antennas [76]. At its core, MoM decomposes the voltage and current on a structure into finite subdivisions and relates the interaction between each section through impedances. MoM generates an N-port impedance matrix where each port represents a single basis function of the whole system. Nonlinear components can be represented as external loads to the ports of the MoM structure, which divides the problem into LTI and nonlinear sub-

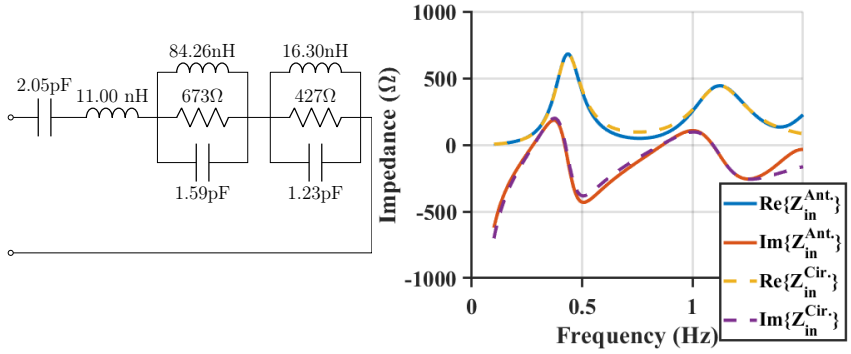
problems. This division allows the system to be evaluated using Rollet's Proviso and ISF safely because the non-Foster component is not inside the compressed network representation like in Figure 7.1.

MoM is typically evaluated in the one-dimensional frequency domain, so some alterations are necessary in order to find the complex frequency MoM (sMoM) matrix. A simple thin-wire dipole will be used to demonstrate a complex frequency MoM representation, but the sMoM method is generalizable to arbitrary geometries. MoM uses the closed-form Electric or Magnetic field integral equations to formulate a constitutive relationship [76]. The thin wire MoM method uses the free space, point-source Green's function,

$$G_0(\boldsymbol{r}, \boldsymbol{r}') = \frac{e^{-jk_0|\boldsymbol{r}-\boldsymbol{r}'|}}{4\pi|\boldsymbol{r}-\boldsymbol{r}'|} \tag{7.3}$$

to solve the integral equations. The free space wavenumber in Eq. (7.3) is usually defined as $k_0 = \frac{2\pi}{\lambda} = \frac{\omega}{\mathrm{c}}$, but will instead be replaced with $k_0 = \frac{\alpha+\mathrm{j}\omega}{c}$ to model complex frequencies. With the use of complex frequency, the Green's function is now analyzing a wave with some arbitrary frequency and decay or growth. This process can be repeated for the governing electric field integral equation and auxiliary equations to model the MoM system in complex frequency.

A wire dipole 50 cm in length with a 1 cm wire radius was simulated using sMoM and its input impedance was compared to that of a circuit model mimicking the antenna's input impedance, shown in Figure 7.2a. Since the circuit model has a closed-form s-domain expression it was used for verification of sMoM. The circuit model was derived using the standard MoM input impedance using only real frequencies. The circuit values were found by tuning the tanks to the anti-resonances and the series LC to the first resonance of the MoM simulation of the same antenna,



(a) (b)

Figure 7.2: Diagram of the circuit model used to compare to the antenna is shown in 7.2a with the corresponding component values, and the input impedance of the purely real frequency MoM model and the circuit model compared in 7.2b.

and then a commercial circuit solver was used to tune the values. Figure 7.2b shows the circuit model input impedance compared to the real frequency MoM simulation versus real frequency. The best agreement is at and below the first anti-resonance, and the traces diverge as the circuit model's level of detail becomes insufficient to capture higher-frequency features.

To measure the success of the sMoM model the Euclidean norm of the location of each local maximum or minimum of $|Z_{in}(s)|$ in complex frequency was compared between the two methods. Figure 7.3 shows two contour plots of the complex input impedance, in dBΩ, with the percent error of the Euclidean norms of each maximum or minimum location. As expected, there is excellent agreement between the two methods on the locations of the first maximum-minimum pair and some agreement for the second pair, while the third pair is not modeled at all by the circuit. Overall, the sMoM model is successfully capturing the presence of poles and zeros and is therefore sufficient for stability analysis.

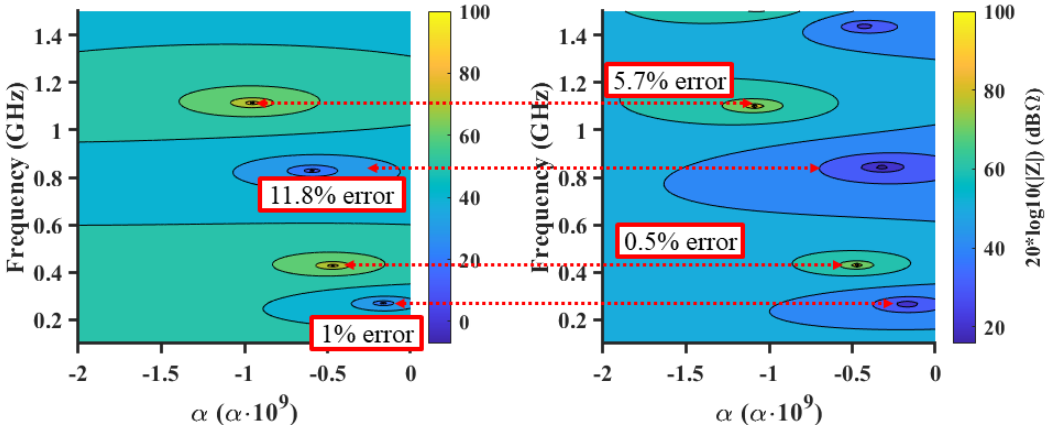


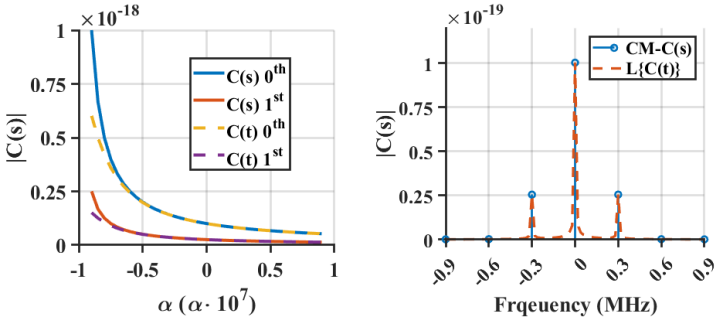
Figure 7.3: Comparison of the complex frequency domain representation of the dipole antenna using sMoM (left) compared to that of the equivalent circuit model of the input impedance (right)

7.4 Complex Frequency Representation of the Nonlinear Capacitor

A complex frequency domain model of the nonlinear component is needed for integration with the sMoM antenna model shown in Section 7.3. The CM linear time varying capacitor model of [14] will be used to model the periodically pumped nonlinear capacitor. For the CM model to be valid the capacitor is assumed to be weakly nonlinear, such that the pumping power is much greater than the excitation and only the first-order harmonics are present. The time domain capacitor model in Eq. (7.2) cannot be used in a complex frequency model, as it will incur a pole on the $\mathbb{R} = 0$ axis. Therefore, the slightly modified version,

$$C(t) = C_0 \cdot (1 + \gamma \cdot \sin(2\pi f_\mathrm{p})) \cdot e^{-at} \cdot \mathrm{u}(t), \tag{7.4}$$

was used, where a is the decay factor of the sinusoid, and with the restrictions that $a > 0$, $0 < \gamma < 1$, and $C_0 > 0$. The decaying exponential in Eq. 7.4 is used to place



(a) Capacitance magnitude at harmonics

(b) Capacitance magnitude at $\alpha = 0$

Figure 7.4: Comparison between the Laplace transform of the time-domain model and the sCM model of the time-varying capacitor.

the pole at $s = a + \mathrm{j}2\pi f_\mathrm{p}$. This time domain model is represented by its constituent harmonic components, which are functions of α, resulting in,

$$C = \begin{bmatrix} C_s(\alpha + \mathrm{j}2\pi f_\mathrm{ex}) & C_s(\alpha + \mathrm{j}2\pi(f_\mathrm{ex} - f_\mathrm{p}) & 0 \\ C_s(\alpha + \mathrm{j}2\pi(f_\mathrm{ex} + f_\mathrm{p}) & C_s(\alpha + \mathrm{j}2\pi f_\mathrm{ex}) & C_s(\alpha + \mathrm{j}2\pi(f_\mathrm{ex} - f_\mathrm{p}) \\ 0 & C_s(\alpha + \mathrm{j}2\pi(f_\mathrm{ex} + f_\mathrm{p}) & C_s(\alpha + \mathrm{j}2\pi(f_\mathrm{ex}) \end{bmatrix}, \tag{7.5}$$

where,

$$C_s(s) = \frac{C_0}{s + a} + \frac{\gamma C_0 2\pi f_\mathrm{p}}{(s + a)^2 + (2\pi f_\mathrm{p})^2}. \tag{7.6}$$

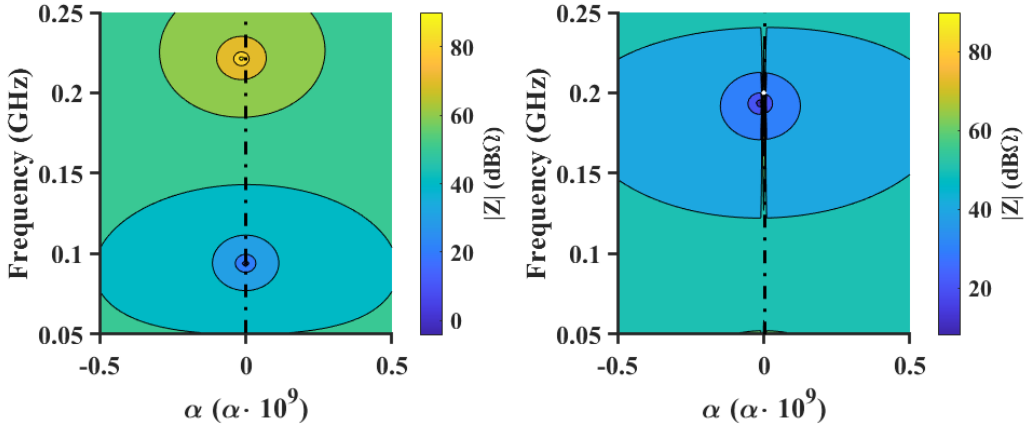
In order to verify that the complex frequency CM (sCM) is constructed correctly, the time domain capacitance was calculated and then transformed into the complex frequency domain. The model used $\gamma = 0.5$, $C_0 = 1$ pF, and $a = 10^7$, where the a value was chosen to reduce computation time in the time domain. Figure 7.4 shows that the magnitude of the capacitance calculated by the complex frequency and time-domain models agrees except in the neighborhood of the pole at $\alpha = 10^{-7}$. This can be attributed to the proximity to the pole, as the Laplace transform becomes progressively more difficult to numerically calculate the closer to

the pole it is performed. Based on this comparison, we conclude that the s-domain representation can correctly model weakly nonlinear devices.

7.5 Complex Frequency Conversion Matrix-Method of Moments Stability Analysis

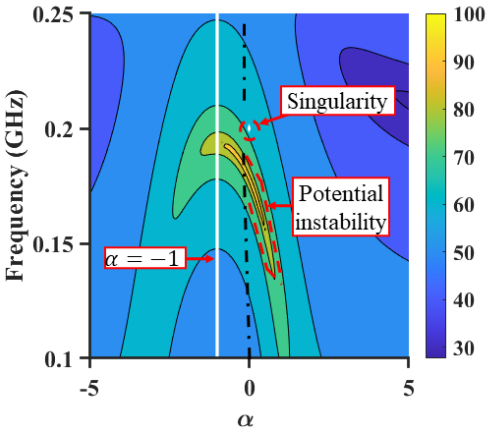
A preliminary test was carried out to demonstrate how to use sCMMoM to verify stability of an on-aperture loaded antenna. For this initial test, the presence of poles was verified by inspection, and were determined by looking for maxima in the complex frequency domain. To test the method, a loop antenna 21 cm in diameter was simulated with a wire radius of 1 cm and was tuned to resonate at approximately 100 MHz using a single static capacitor of 4.7 pF. Figure 7.6a shows the LTI input impedance of the loop antenna versus complex frequency. For the LTI case, there is one pole in the left-half side of the s-domain creating the anti-resonance as indicated by the maxima around 0.2125 GHz. The capacitor was then pumped at a frequency of 200 MHz with a modulation factor of $\gamma = 0.2$ and $a = 1$. While a large a was useful for the time-domain calculations to run efficiently, the requirement $a << f_{\mathrm{p}}$ for the full sCMMoM method is necessary. This is equivalent to modeling near steady-state conditions for the time-varying capacitor which is the operating condition of the system. The dampened sine of the capacitor could result in a pole being shifted from the right side to the left side of the s-domain in error, but if $a << f_{\mathrm{p}}$ then any possible shift is negligible. When inspecting poles very near the y-axis allowing $a \to 0^{+}$ will help ensure that there is no effect from a on pole placement.

The magnitude of the input impedance of the complex frequency domain calculations, here defined as $Z_{in} = \frac{V_{ex}}{I_{ex}}$ where V_{ex} and I_{ex} are the voltage and current at

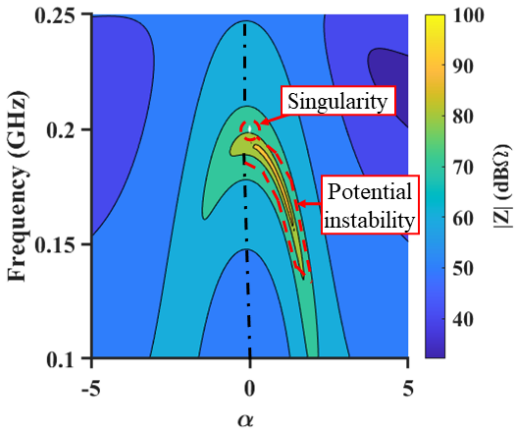


(a) Z_{in} of the LTI antenna

(b) Z_{in} of the non-LTI antenna



(c) Zoomed in Z_{in} of the non-LTI antenna



(d) Zoomed in Z_{in} of the non-LTI antenna, $a = 0.1$

Figure 7.5: Two dimensional input impedances of the stable LTI (7.5a) antenna, the potentially unstable non-LTI (7.5b & 7.5c) antenna, and the potentially unstable non-LTI case (7.5d) with $a = 0.1$.

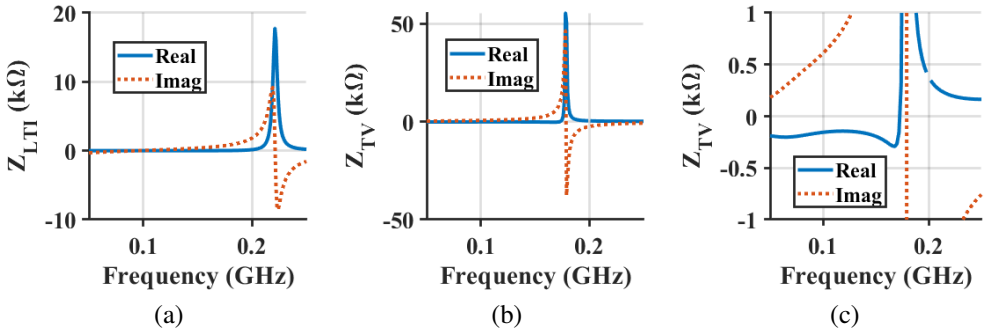


Figure 7.6: Input impedance at $\alpha = 0$ of a stable (7.6a) LTI antenna and the input impedance of the unstable (7.6b & 7.6b) non-LTI antenna. Figure

the excitation, is presented in Figure 7.5. By inspection of Figures 7.5c and 7.5d, there do exist poles within the frequency range of interest in the right half plane of the complex frequency domain. There is a white diamond indicating that the method resulted in a singular matrix for that particular value of s, so at a frequency of $f_{\text{ex}} = f_{\text{p}} = 200$ MHz the loaded antenna appears unconditionally unstable [75]. However, this is not entirely true. There is technically oscillation occurring at this frequency, but this is due to the pumping source directly delivering power to the signal and not because the system is truly unstable. There is also another potentially unstable region just below 200 MHz where maxima in the right-hand plane indicate possible poles. The antenna is recalculated for a capacitor with a decay of $a = 0.1$ to see the impact of the choice of $a = 1$. Figure 7.5d shows that $a = 1$ did shift the response over slightly, and that the maximal region is entirely in the right-hand plane as $a \to 0^+$. sCMMoM has successfully verified that the loaded antenna should not be operated around the region where $f_{\text{ex}} \approx f_{\text{p}}$, but that there could be stability elsewhere provided that the device passes the ISF test.

To verify ISF there can be no negative resistance seen at the port of the antenna, and Figure 7.6 shows that the input resistance of the non-LTI-loaded antenna does

become negative for some frequencies. This is expected as there was no load resistance to offset the negative resistance of the amplifier, thus resulting in instability. To alleviate the instability, a load resistance must be used to overcome the negative resistance in the desired operating region. With the current configuration, the antenna requires approximately 200 Ω to overcome the negative input resistance since the input impedance is approximately -200Ω. The sCMMoM method was able to verify the conditional stability of the non-LTI antenna in a region of degenerate-mode negative resistance amplification [36].

7.6 Conclusion

This chapter reviewed literature on the stability of non-LTI devices in an effort to highlight the importance of rigorously validating their stability. This chapter then established a method of using MoM to create a complex frequency domain representation of an RF structure using CM to load it with a TV element. This sCMMoM method is particularly powerful for large investigations into novel structures and applications of TV elements with RF structures, as doing this large of a sweep for stability verification in the transient domain would be much more computationally expensive. The next step of leveraging sCMMoM for stability analysis is to use a more generalized pole detection method to determine the existence of poles in the right hand plane of the complex frequency domain instead of calculating a wide sweep of possible values and visually inspection the results for each iteration.

Chapter 8

Conclusion

This dissertation has demonstrated that parametric tuning can be used on receiving ESAs to increase their signal throughput beyond their LTI capabilities. Consider Figure 8.1, where the maximum bandwidth achievable for an antenna within a fixed ka sphere using the radiation efficiency of the 2 to 1 concentric loop (cLoop max) and the square loop (loop max) are compared to the actual bandwidths of the LTI and TV versions of the 2 to 1 and square loops. The LTI versions of each antenna, denoted by the circle markers, are considerably lower than the fundamental maximum bandwidth. This is largely due to the planar loop not filling much of the circumscribing ka sphere, since filling the volume of a ka sphere is directly proportionate to approaching the fundamental limit [2]. The bandwidth of a planar, meandered dipole with a radiation efficiency of 64% is also plotted in Figure 8.1. This trace is based on the meandered dipole design from [65], as this type of ESA approaches the fundamental minimum Q for an electrically small, planar antenna [5]. Due to its' performance and straight-forward design, the meandered dipole is widely used as the standard, state-of-the-art ESA in numerous applications.

The bandwidth versus ka of the singly loaded, TV version of the concentric loop is shown in Figure 8.1 with the red x marker. The optimization from chap-

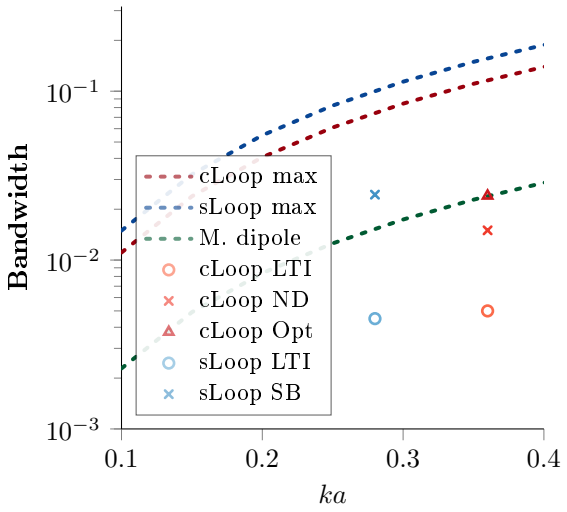


Figure 8.1: Comparison of the non-degenerate (cLoop ND) and single balanced (sLoop SB) antennas to the maximum achievable bandwidths for their radiation efficiencies (cLoop max at 0.58 and sLoop max at 0.43, respectively), the LTI concentric loop (cLoop LTI), the LTI square loop (sLoop LTI), and an optimized version of the ND case (cLoop Opt). The two loops and accompanying bounds are also compared to the projected performance of a planar meandered dipole [65].

ter 4 was used on the concentric loop as well to see if the bandwidth could be further improved for a fixed modulation factor, and is also plotted on Figure 8.1 as the red, triangular marker. The TV concentric loop did perform much better than the LTI case, and the optimized version has a comparable bandwidth to the meandered dipole. A loop antenna can be used to reduce the overall size of a receiver since components can be placed inside of the loop without significantly impacting performance. Therefore, the optimized concentric loop can reduce the overall size of the receive system without sacrificing bandwidth relative to the state-of-the-art ESA.

The bandwidth versus ka of the single balanced square loop is is also shown in Figure 8.1 with the blue x marker. Since it is only a single loop where the concentric loop has the second, inner loop, it has more surface area for components than the concentric loop for its electrical size. The single balanced design also has a wider

bandwidth than even the optimized concentric loop despite the reduction in size. Comparing the single balanced square loop to the meandered dipole, it exceeds the dipole's bandwidth by nearly 50%. Therefore, the single balanced, square loop can both reduce the overall receiver footprint while also improving the bandwidth relative to the state-of-the-art ESA.

Future work will initially focus on realized prototypes of the designs laid out here. While the TVCs were designed to be realizable with COTS varactors, there is still the task of designing the pumping network and varactor to produce the TVC. Investigating different antenna designs to attempt to circumvent the Chu limit is also a an important avenue to investigate. Another task is to improve the single balanced ESA design process by creating a circuit model analysis like in chapter 4, as single balanced parametric amplifiers do not have a full circuit model analysis and design equations to date. The circuit model can be used to optimize the single balanced design to further improve the bandwidth of particular designs like with the singly loaded case. Also, the parametrically tuned ESF needs a formal design process where a filter synthesis technique directly incorporates the negative resistance and effective static capacitance in the design equations like in circuital parametric amplifiers that use filter as the coupling network. The parametrically tuned ESF can also benefit from using a more filter topology where all the elements are radiators so it can more closely achieve the Chu limit before parametric tuning.

References

[1] H. Wheeler, "Fundamental Limitations of Small Antennas," *Proceedings of the IRE*, vol. 35, no. 12, pp. 1479–1484, Dec. 1947, ISSN: 2162-6634. DOI: 10.1109/JRPROC.1947.226199

[2] L. J. Chu, "Physical Limitations of Omni-Directional Antennas," *Journal of Applied Physics*, vol. 19, p. 14, 1948.

[3] R. F. Harrington, "Effect of antenna size on gain, bandwidth, and efficiency," *Journal of Research of the National Bureau of Standards, Section D: Radio Propagation*, vol. 64D, no. 1, p. 1, Jan. 1960, ISSN: 1060-1783. DOI: 10.6028/jres.064D.003 Accessed: Apr. 8, 2024. [Online]. Available: https://nvlpubs.nist.gov/nistpubs/jres/64D/jresv64Dn1p1_A1b.pdf

[4] J. S. McLean, "A re-examination of the fundamental limits on the radiation Q of electrically small antennas," *IEEE Transactions on Antennas and Propagation*, vol. 44, no. 5, pp. 672–, May 1996, ISSN: 1558-2221. DOI: 10.1109/8.496253

[5] M. Gustafsson, C. Sohl, and G. Kristensson, "Physical limitations on antennas of arbitrary shape," *Proceedings of the Royal Society A: Mathematical, Physical and Engineering Sciences*, vol. 463, no. 2086, pp. 2589–2607, Jul. 18, 2007. DOI: 10.1098/rspa.2007.1893 Accessed: Apr. 8, 2024. [Online]. Available: https://royalsocietypublishing.org/doi/full/10.1098/rspa.2007.1893

[6] D. F. Sievenpiper et al., "Experimental Validation of Performance Limits and Design Guidelines for Small Antennas," *IEEE Transactions on Antennas and Propagation*, vol. 60, no. 1, pp. 8–19, 2012, ISSN: 1558-2221. DOI: 10.1109/TAP.2011.2167938

[7] M. Capek, M. Gustafsson, and K. Schab, "Minimization of Antenna Quality Factor," *IEEE Transactions on Antennas and Propagation*, vol. 65, no. 8, pp. 4115–4123, Aug. 2017, ISSN: 0018-926X, 1558-2221. DOI: 10.1109/

TAP.2017.2717478 Accessed: Mar. 1, 2024. [Online]. Available: https://ieeexplore.ieee.org/document/7953652/

[8] M. Capek et al., "Optimal Planar Electric Dipole Antennas: Searching for antennas reaching the fundamental bounds on selected metrics," *IEEE Antennas and Propagation Magazine*, vol. 61, no. 4, pp. 19–29, Aug. 2019, ISSN: 1558-4143. DOI: 10.1109/MAP.2019.2920088 Accessed: Aug. 15, 2024. [Online]. Available: https://ieeexplore.ieee.org/document/8751149/?arnumber=8751149

[9] M. Gustafsson, M. Capek, and K. Schab, "Tradeoff Between Antenna Efficiency and Q-Factor," *IEEE Transactions on Antennas and Propagation*, vol. 67, no. 4, pp. 2482–2493, Apr. 2019, ISSN: 1558-2221. DOI: 10.1109/TAP.2019.2891448 Accessed: Sep. 4, 2024. [Online]. Available: https://ieeexplore.ieee.org/document/8605342/?arnumber=8605342

[10] J. J. Adams and J. T. Bernhard, "A Modal Approach to Tuning and Bandwidth Enhancement of an Electrically Small Antenna," *IEEE Transactions on Antennas and Propagation*, vol. 59, no. 4, pp. 1085–1092, Apr. 2011, ISSN: 1558-2221. DOI: 10.1109/TAP.2011.2109683

[11] L. Jelinek, K. Schab, and M. Capek, "Radiation Efficiency Cost of Resonance Tuning," *IEEE Transactions on Antennas and Propagation*, vol. 66, no. 12, pp. 6716–6723, Dec. 2018, ISSN: 1558-2221. DOI: 10.1109/TAP.2018.2870492 Accessed: Jul. 21, 2024. [Online]. Available: https://ieeexplore.ieee.org/document/8466803/?arnumber=8466803

[12] H. Wheeler, "The wide-band matching area for a small antenna," *IEEE Transactions on Antennas and Propagation*, vol. 31, no. 2, pp. 364–367, Mar. 1983, ISSN: 0096-1973. DOI: 10.1109/TAP.1983.1143030 Accessed: May 18, 2024. [Online]. Available: http://ieeexplore.ieee.org/document/1143030/

[13] K. Schab, D. Huang, and J. J. Adams, "An Energy-Synchronous Direct Antenna Modulation Method for Phase Shift Keying," *IEEE Open Journal of Antennas and Propagation*, vol. 1, pp. 41–46, 2020, ISSN: 2637-6431. DOI: 10.1109/OJAP.2020.2972842

[14] K. Schab, D. Huang, and J. J. Adams, "Pulse Characteristics of a Direct Antenna Modulation Transmitter," *IEEE Access*, vol. 7, pp. 30 213–30 219, 2019, ISSN: 2169-3536. DOI: 10.1109/ACCESS.2019.2902365 Accessed: Jan. 20, 2023. [Online]. Available: https://ieeexplore.ieee.org/document/8654637/

[15] A. Shlivinski and Y. Hadad, "Beyond the Bode-Fano Bound," *Physical Review Letters*, vol. 121, no. 20, 2018, ISSN: 0031-9007, 1079-7114.

[16] S. E. Sussman-Fort and R. M. Rudish, "Non-Foster Impedance Matching of Electrically-Small Antennas," *IEEE Transactions on Antennas and Propagation*, vol. 57, no. 8, pp. 2230–2241, Aug. 2009, ISSN: 1558-2221. DOI: 10.1109/TAP.2009.2024494

[17] P. Loghmannia and M. Manteghi, "Broadband Parametric Impedance Matching for Small Antennas Using the Bode-Fano Limit: Improving on Chu's limit for loaded small antennas," *IEEE Antennas and Propagation Magazine*, vol. 64, no. 5, pp. 55–68, Oct. 2022, ISSN: 1558-4143. DOI: 10.1109/MAP.2021.3089997

[18] M. Hedayati, L. K. Yeung, M. Panahi, X. Zou, and Y. E. Wang, "Parametric Downconverter for Mixer-First Receiver Front Ends," *IEEE Transactions on Microwave Theory and Techniques*, vol. 69, no. 5, pp. 2712–2721, May 2021, ISSN: 1557-9670. DOI: 10.1109/TMTT.2021.3058214

[19] L. K. Yeung, M. Hedayati, M. Panahi, A. Aalipour, and Y. E. Wang, "Parametric Matching of Electrically Small Antennas for Broadband and Low Noise Reception," in *2024 IEEE International Symposium on Antennas and Propagation and INC/USNC-URSI Radio Science Meeting (AP-S/INC-USNC-URSI)*, Jul. 2024, pp. 793–794. DOI: 10.1109/AP-S/INC-USNC-URSI52054.2024.10686739 Accessed: Jul. 2, 2025. [Online]. Available: https://ieeexplore.ieee.org/document/10686739/

[20] A. Mekawy, H. Li, Y. Radi, and A. Alù, "Parametric Enhancement of Radiation from Electrically Small Antennas," *Physical Review Applied*, vol. 15, no. 5, p. 054 063, May 27, 2021, ISSN: 2331-7019.

[21] H. Li, A. Mekawy, and A. Alù, "Beyond Chu's Limit with Floquet Impedance Matching," *Physical Review Letters*, vol. 123, no. 16, p. 164 102, Oct. 16, 2019, ISSN: 0031-9007, 1079-7114. DOI: 10.1103/PhysRevLett.123.164102 Accessed: Sep. 4, 2023. [Online]. Available: https://link.aps.org/doi/10.1103/PhysRevLett.123.164102

[22] P. Loghmannia and M. Manteghi, "An Active Cavity-Backed Slot Antenna Based on a Parametric Amplifier," *IEEE Transactions on Antennas and Propagation*, vol. 67, no. 10, pp. 6325–6333, Oct. 2019, ISSN: 1558-2221. DOI: 10.1109/TAP.2019.2920236

[23] Z. Fritts, A. Babaee, S. M. Young, and A. Grbic, "Space-Time Modulation of a Multimode Electrically Small Antenna for Increased Matching and Efficiency Bandwidths," *IEEE Transactions on Antennas and Propagation*, pp. 1–1, 2024, ISSN: 1558-2221. DOI: 10.1109/TAP.2024.3508081

[24] J. M. Manley and H. E. Rowe, "Some General Properties of Nonlinear Elements: Part I. General Energy Relations," *Proceedings of the IRE*, vol. 44, no. 7, pp. 904–913, Jul. 1956, ISSN: 2162-6634. DOI: 10.1109/JRPROC.1956.275145

[25] C. Blosser, A. Bauer, J. E. Ruyle, K. C. Kerby-Patel, and K. Schab. "Signal Fidelity in Degenerate and Nondegenerate Mode Parametric Amplifier Antennas." arXiv: 2403.11067 [cs, eess], Accessed: Apr. 6, 2024. [Online]. Available: http://arxiv.org/abs/2403.11067 pre-published.

[26] C. Balanis, *Antenna Theory*, 2nd ed. New York: John Wiley & Sons, Inc., 1997, ISBN: 0-471-59268-4.

[27] *Antenna Toolbox for MATLAB (AToM)*, Czech Technical University in Prague, Department of Electromagnetic Field, 2025. [Online]. Available: http://www.antennatoolbox.com/

[28] S. F. Bass, A. M. Palmer, K. R. Schab, K. C. Kerby-Patel, and J. E. Ruyle, "Conversion Matrix Method of Moments for Time-Varying Electromagnetic Analysis," *IEEE Transactions on Antennas and Propagation*, vol. 70, no. 8, pp. 6763–6774, Aug. 2022, ISSN: 0018-926X, 1558-2221. DOI: 10.1109/TAP.2022.3164938 Accessed: Jan. 5, 2023. [Online]. Available: https://ieeexplore.ieee.org/document/9755023/

[29] *High Frequency Simulation Software (HFSS)*, version 2021R2, Ansys, 2021.

[30] S. A. Maas, *Nonlinear Microwave and RF Circuits*, 2nd ed. Boston, MA: Artech House, 2003, ISBN: 978-1-58053-611-0.

[31] *Pathwave advanced design system*, Keysight. [Online]. Available: https://www.%20keysight.com/us/en/products/software/pathwave-design-software/%20pathwave-advanced-design-system.html.

[32] G. Fisher and J. Connelly, "Modeling Time-Dependent Elements for SPICE Transient Analyses," *IEEE Transactions on Computer-Aided Design of Integrated Circuits and Systems*, vol. 5, no. 3, pp. 429–432, Jul. 1986, ISSN:

0278-0070. DOI: 10.1109/TCAD.1986.1270212 Accessed: Mar. 13, 2024. [Online]. Available: http://ieeexplore.ieee.org/document/1270212/

[33] J. Proakis and M. Salehi, *Digital Communications*, fifth. McGraw-Hill, 2008.

[34] "Recommendation ITU-R P.372-17 (08/2024) - Radio noise,"

[35] M. Faraday, "On a peculiar class of Acoustical and on certain Forms assumed by groups of particles upon vibrating elastic Surfaces," *Corr. Mom. Acad. Science of Paris*, pp. 299–340, 1831.

[36] L. Blackwell and K. Kotzebue, *Semiconductor-Diode Parametric Amplifiers*. Englewood Cliffs, NJ: Prentice-Hall Inc., 1961.

[37] H. Heffner and G. Wade, "Gain, Band Width, and Noise Characteristics of the Variable-Parameter Amplifier," *Journal of Applied Physics*, vol. 29, no. 9, pp. 1321–1331, Sep. 1958, ISSN: 0021-8979, 1089-7550. DOI: 10.1063/1.1723436 Accessed: Nov. 15, 2022. [Online]. Available: http://aip.scitation.org/doi/10.1063/1.1723436

[38] H. Rowe, "Some General Properties of Nonlinear Elements. II. Small Signal Theory," *Proceedings of the IRE*, vol. 46, no. 5, pp. 850–860, May 1958, ISSN: 0096-8390. DOI: 10.1109/JRPROC.1958.286938 Accessed: Nov. 15, 2022. [Online]. Available: http://ieeexplore.ieee.org/document/4065408/

[39] "SMV123x Series: Hyperabrupt Junction Tuning Varactors," Skyworks Solutions, In, 2020. Accessed: Apr. 7, 2024. [Online]. Available: https://www.skyworksinc . com/ - /media / SkyWorks / Documents / Products / 101 - 200 / SMV123x_Series_200058AA.pdf

[40] G. Matthaei, "A Study of the Optimum Design of Wide-Band Parametric Amplifiers and Up-Converters," *IRE Transactions on Microwave Theory and Techniques*, vol. 9, no. 1, pp. 23–38, Jan. 1961, ISSN: 2331-088X. DOI: 10.1109/TMTT.1961.1125259

[41] E. Kuh and M. Fukada, "Optimum Synthesis of Wide-Band Parametric Amplifiers and Converters," *IRE Transactions on Circuit Theory*, vol. 8, no. 4, pp. 410–415, 1961, ISSN: 0096-2007. DOI: 10.1109/TCT.1961.1086824 Accessed: Mar. 8, 2024. [Online]. Available: http://ieeexplore.ieee.org/document/1086824/

[42] J. DeJager, "Maximum Bandwidth Performance of Non- degenerate Parametric Amplifier with Single-Tuned Idler Circuit," *IEEE Transactions on Microwave Theory and Techniques*, vol. 12, no. 4, pp. 459–467, Jul. 1964, ISSN: 0018-9480. DOI: 10.1109/TMTT.1964.1125847 Accessed: Mar. 8, 2024. [Online]. Available: http://ieeexplore.ieee.org/document/1125847/

[43] P. Loghmannia, "Time-Variant Components to Improve Bandwidth and Noise Performance of Antennas."

[44] S. R. Best and B. C. Kaanta, "A Tutorial on the Receiving and Scattering Properties of Antennas," *IEEE Antennas and Propagation Magazine*, vol. 51, no. 5, pp. 26–37, Oct. 2009, ISSN: 1558-4143. DOI: 10.1109/MAP.2009.5432036 Accessed: Jul. 8, 2025. [Online]. Available: https://ieeexplore.ieee.org/document/5432036/

[45] D. Pozar, *Microwave Engineering*. John Wiley & Sons, Inc., 2011.

[46] C. Harrison and R. King, "Folded dipoles and loops," *IRE Transactions on Antennas and Propagation*, vol. 9, no. 2, pp. 171–187, Mar. 1961, ISSN: 1558-3643. DOI: 10.1109/TAP.1961.1144962

[47] J. Sevick, *Transmission Line Transformers*, 4th ed. U.S.A.: Scitech Publishing, Inc., 2006, ISBN: 1-884932-18-5.

[48] J. E. Storer, "Impedance of thin-wire loop antennas," *Transactions of the American Institute of Electrical Engineers, Part I: Communication and Electronics*, vol. 75, no. 5, pp. 606–619, Nov. 1956, ISSN: 2379-674X. DOI: 10.1109/TCE.1956.6372437 Accessed: Jun. 10, 2025. [Online]. Available: https://ieeexplore.ieee.org/document/6372437/

[49] R. Waltz, J. Morales, J. Nocedal, and D. Orban, "An interior algorithm for nonlinear optimization that combines line search and trust region steps," *Mathematical Programming*, vol. 107, no. 3, pp. 391–408, Jul. 2006, ISSN: 0025-5610, 1436-4646. DOI: 10.1007/s10107-004-0560-5 Accessed: Jul. 2, 2025. [Online]. Available: https://link.springer.com/10.1007/s10107-004-0560-5

[50] J. Pearson and K. Lunt, "A broadband balanced idler circuit for parametric amplifiers," *Radio and Electronic Engineer*, vol. 27, no. 5, p. 331, 1964, ISSN: 00337722. DOI: 10.1049/ree.1964.0062 Accessed: Feb. 20, 2023. [Online]. Available: https://digital-library.theiet.org/content/journals/10.1049/ree.1964.0062

[51] S. Hayasi and T. Kurokawa, "A Balanced-Type Parametric Amplifier," *IRE Transactions on Microwave Theory and Techniques*, vol. 10, no. 3, pp. 185–190, May 1962, ISSN: 2331-088X. DOI: 10.1109/TMTT.1962.1125489

[52] W. Ku, "A Broad-Banding Theory for Varactor Parametric Amplifiers-Part I," *IEEE Transactions on Circuit Theory*, vol. 11, no. 1, pp. 50–58, Mar. 1964, ISSN: 2374-9555. DOI: 10.1109/TCT.1964.1082234

[53] W. Ku, "A Broad-Banding Theory for Varactor Parametric Amplifiers-Part II," *IEEE Transactions on Circuit Theory*, vol. 11, no. 1, pp. 59–66, 1964, ISSN: 0018-9324. DOI: 10.1109/TCT.1964.1082235 Accessed: Nov. 9, 2022. [Online]. Available: http://ieeexplore.ieee.org/document/1082235/

[54] H. W. Bode, "Network Analysis and Feedback Amplifier Design,"

[55] W. Getsinger and G. Matthaei, "Some Aspects of the Design of Wide-Band Up-Converters and Nondegenerate Parametric Amplifiers," *IEEE Transactions on Microwave Theory and Techniques*, vol. 12, no. 1, pp. 77–87, Jan. 1964, ISSN: 0018-9480. DOI: 10.1109/TMTT.1964.1125755 Accessed: Mar. 9, 2024. [Online]. Available: http://ieeexplore.ieee.org/document/1125755/

[56] R. Aron, "Bandwidth Limitations and Syntehsis Procedures for Negative Resistance and Variable Reactance Amplifiers," California Institute of Technology, Pasadena, California, 1960. Accessed: Mar. 11, 2024. [Online]. Available: https://thesis.library.caltech.edu/1071/1/Aron_rm_1961.pdf

[57] L. Weinberg and P. Slepian, "Takahasi's Results on Tchebycheff and Butterworth Ladder Networks," *IRE Transactions on Circuit Theory*, vol. 7, no. 2, pp. 88–101, 1960, ISSN: 0096-2007. DOI: 10.1109/TCT.1960.1086643 Accessed: Mar. 19, 2024. [Online]. Available: http://ieeexplore.ieee.org/document/1086643/

[58] C. Barnes, W. Bertram, and M. Cowan, "A low-noise, wideband, L-band parametric amplifier," in *1964 IEEE International Solid-State Circuits Conference. Digest of Technical Papers*, Philadelphia, PA, USA: IEEE, 1964, pp. 24–25. DOI: 10.1109/ISSCC.1964.1157506 Accessed: Mar. 12, 2024. [Online]. Available: https://ieeexplore.ieee.org/document/1157506/

[59] J.-s. Hong and M. J. Lancaster, *Microstrip Filters for RF/Microwave Applications*. JOHN WILEY & SONS, INC., 2001, ISBN: 0-471-22161-9.

[60] M. Dishal, "Alignment and Adjustment of Synchronously Tuned Multiple-Resonant-Circuit Filters," *Proceedings of the IRE*, vol. 39, no. 11, pp. 1448–1455, Nov. 1951, ISSN: 0096-8390. DOI: 10.1109/JRPROC.1951.273611 Accessed: May 17, 2024. [Online]. Available: http://ieeexplore.ieee.org/document/4050569/

[61] A. Yaghjian and S. Best, "Impedance, bandwidth, and Q of antennas," *IEEE Transactions on Antennas and Propagation*, vol. 53, no. 4, pp. 1298–1324, Apr. 2005, ISSN: 1558-2221. DOI: 10.1109/TAP.2005.844443

[62] A. Bauer, "External quality factor of antennas and their use in filtenna design," May 13, 2022. Accessed: May 28, 2024. [Online]. Available: https://shareok.org/handle/11244/335688

[63] R. Harrington, "On the gain and beamwidth of directional antennas," *IRE Transactions on Antennas and Propagation*, vol. 6, no. 3, pp. 219–225, Jul. 1958, ISSN: 1558-3643. DOI: 10.1109/TAP.1958.1144605 Accessed: Jul. 21, 2024. [Online]. Available: https://ieeexplore.ieee.org/document/1144605/?arnumber=1144605

[64] J. Dunsmore, "Advanced Filter Tuning using Time Domain Transforms," in *1999 29th European Microwave Conference*, vol. 2, Oct. 1999, pp. 72–75. DOI: 10.1109/EUMA.1999.338412 Accessed: Aug. 13, 2024. [Online]. Available: https://ieeexplore.ieee.org/document/4139441/?arnumber=4139441

[65] S. R. Best, "Electrically Small Resonant Planar Antennas: Optimizing the quality factor and bandwidth," *IEEE Antennas and Propagation Magazine*, vol. 57, no. 3, pp. 38–47, Jun. 2015, ISSN: 1045-9243, 1558-4143. DOI: 10.1109/MAP.2015.2437271 Accessed: Apr. 4, 2024. [Online]. Available: https://ieeexplore.ieee.org/document/7163524/

[66] D. J. Healey, "An Examination of the Gamma Match," *QST*, pp. 11–15, 57, Apr. 1969. Accessed: Jun. 4, 2024. [Online]. Available: http://bcpink.com/KB3IFH/files/Download/Gamma%20Match%20article.pdf

[67] M.-C. Tang, Y. Chen, and R. W. Ziolkowski, "Experimentally Validated, Planar, Wideband, Electrically Small, Monopole Filtennas Based on Capacitively Loaded Loop Resonators," *IEEE Transactions on Antennas and Propagation*, vol. 64, no. 8, pp. 3353–3360, Aug. 2016, ISSN: 0018-926X, 1558-2221. DOI: 10.1109/TAP.2016.2576499 Accessed: May 18, 2024. [Online]. Available: http://ieeexplore.ieee.org/document/7484724/

[68] "RT/duroid 5880LZ laminates," Rogers Corp., 2025. [Online]. Available: https://www.rogerscorp.com/advanced-electronics-solutions/rt-duroid-laminates/rt-duroid-5880lz-laminates

[69] J. Rollett, "Stability and Power-Gain Invariants of Linear Twoports," *IRE Transactions on Circuit Theory*, vol. 9, no. 1, pp. 29–32, Mar. 1962, ISSN: 2331-3854. DOI: 10.1109/TCT.1962.1086854

[70] A. Platzker and W. Struble, "Rigorous determination of the stability of linear n-node circuits from network determinants and the appropriate role of the stability factor K of their reduced two-ports," in *Third International Workshop on Integrated Nonlinear Microwave and Millimeterwave Circuits*, Oct. 1994, pp. 93–107. DOI: 10.1109/INMMC.1994.512515

[71] R. Jackson, "Rollett Proviso in the Stability of Linear Microwave Circuits—A Tutorial," *IEEE Transactions on Microwave Theory and Techniques*, vol. 54, no. 3, pp. 993–1000, Mar. 2006, ISSN: 1557-9670. DOI: 10.1109/TMTT.2006.869719

[72] S. D. Stearns, "Incorrect stability criteria for non-foster circuits," in *Proceedings of the 2012 IEEE International Symposium on Antennas and Propagation*, Jul. 2012, pp. 1–2. DOI: 10.1109/APS.2012.6348832

[73] S. C. Cripps, *Advanced Techniques in RF Power Amplifier Design*. Artech House, 2002, 342 pp., ISBN: 978-1-58053-564-9.

[74] B. Gray, F. Ramirez, B. Melville, A. Suarez, and J. S. Kenney, "A Broadband Double-Balanced Phase-Coherent Degenerate Parametric Amplifier," *IEEE Microwave and Wireless Components Letters*, vol. 21, no. 11, pp. 607–609, Nov. 2011, ISSN: 1558-1764. DOI: 10.1109/LMWC.2011.2167137

[75] W. H. Ku, "Stability of linear active nonreciprocal N-ports," *Journal of the Franklin Institute*, vol. 276, no. 3, pp. 207–224, Sep. 1, 1963, ISSN: 0016-0032. DOI: 10.1016/0016-0032(63)90383-1 Accessed: Mar. 17, 2023. [Online]. Available: https://www.sciencedirect.com/science/article/pii/0016003263903831

[76] J.-M. Jin, *Theory and Computation of Electromagnetic Fields*. Wiley-IEEE Press, 2010, ISBN: 978-0-470-87425-7. [Online]. Available: https://ieeexplore.ieee.org/book/5628376